THESIS

THE EFFECTS OF LAND SURFACE-ATMOSPHERE INTERACTIONS WITHIN TWO CONVECTIVE STORM REGIMES

Submitted by

Benjamin D. Ascher

Department of Atmospheric Science

In partial fulfillment of the requirements

For the Degree of Master of Science

Colorado State University

Fort Collins, Colorado

Spring 2024

Master's Committee:

Advisor: Susan C. van den Heever

Russ Schumacher
Daniel McGrath

ABSTRACT

THE EFFECTS OF LAND SURFACE-ATMOSPHERE INTERACTIONS WITHIN TWO CONVECTIVE STORM REGIMES

Convective storms, which are driven in part by atmospheric thermodynamic instability, come in a range of shapes and sizes and bring a variety of impacts both at the surface and throughout the atmosphere. Often these storms initiate as a result of lifting within the Planetary Boundary Layer (PBL), the behavior of which is strongly affected by the characteristics of the land surface below them. To examine the effects of land surface properties on convective storm behavior and impacts, I have conducted two high-resolution mesoscale modeling studies. The first study examined the impact of Lake Huron on convective lake-effect snow over Lake Erie, while the second analyzed the effects of heterogeneous vegetation cover on deep convection in an idealized coastal environment. Our findings in the first study revealed that Lake Huron initiates lake-effect snow bands which persist over land between Lake Huron and Lake Erie and then reintensify after moving over Lake Erie. The persistent band "kickstarts" convection over Lake Erie and increases snowfall over and downwind of Lake Erie compared to when Lake Huron is not present. I also found that areas of snow-free land can act as a "brown lake" and initiate lake effect-like convection on their own. An area of snow-free land upwind of Lake Erie fulfilled a similar role to Lake Huron in enhancing convection and snowfall downwind of Lake Erie. Such findings may have important implications for improved short-term forecasting of the location and intensity of heavy snowfall. The results in our second study indicated that heterogeneous land surfaces enhance convective storm activity over certain vegetation types and suppress it over others. In particular, I found an increase in precipitation over forests surrounded by pasture lands and suburban regions, while the precipitation over the pasture and suburban regions is suppressed. I also discovered that circulations induced by these heterogeneous land surfaces appear to be more important to the location and timing of

convection initiation than a sea breeze which forms in the simulations. Finally, I concluded that cold pools produced by convective storms reinforce the land surface-induced circulations, thereby allowing these circulations to collide in the center of the forested region, where they initiate intense convection which subsequently produces heavy rainfall.

ACKNOWLEDGEMENTS

I would like to thank Dr. Susan C. van den Heever, Dr. Peter J. Marinescu, and Stephen M. Saleeby for their tireless efforts in helping me design and run model simulations, analyze the simulation output, and synthesize the results into the chapters present here. I would also like to thank Dr. Leah Grant, Dr. Ian Baker, Dr. Hassan Dashtian, and John Boris at the National Weather Service Forecast Office in Gaylord, MI, for their help with data products and process analysis.

I would like to thank my friends at the Department of Atmospheric Science. My years here at CSU have been the best of my life, entirely because of the incredible community of students. I'm beyond sad to leave after what feels in retrospect like such a short time here.

Finally, I want to thank my family. Mom, Dad, Josh, and of course Leo, you've all supported me in different ways for so many years. I can't even think how much you've all had to do over the years to get me to this point.

This work was funded by the NSF ESCAPE Grant AGS-2019947. I would like to acknowledge high-performance computing support from Cheyenne (doi:10.5065/D6RX99HX) provided by NCAR's Computational and Information Systems Laboratory, sponsored by the National Science Foundation.

TABLE OF CONTENTS

LIST OF TABLES

LIST OF FIGURES

Chapter 1

Introduction

Convective storms occur around the world in a variety of morphologies. These range from small puffy cumulus clouds which appear overhead on an otherwise tranquil sunny day to ferocious tropical cyclones which grow to the top of the troposphere and bring devastating rainfall, winds, and storm surges to coastal communities. Despite their massive difference in scale and impacts, both of these atmospheric phenomena, as well as many others, are driven to some extent by the same fundamental principle of atmospheric instability. In this thesis, I will examine two vastly different convective phenomena, lake-effect snow and coastal deep convection, and analyze the role of land surface properties in the initiation, evolution, and impacts of these storm systems. The first phenomenon, lake-effect snow, occurs during the cool season as cold air blows over warm lakes. This results in strong sensible heating at the lake surface and subsequent destabilization of the atmosphere, which results in shallow convection. This shallow convection can produce heavy snowfall, which often occurs in long bands parallel to the mean wind direction. The size, shape, depth, and snowfall rates of these convective bands are sensitive to Planetary Boundary Layer (PBL) characteristics such as temperature, humidity, and wind.

Over the Great Lakes of the United States and Canada, lake-effect snow often occurs under westerly or northwesterly winds which advect cold air southward from the Canadian Arctic in late fall and early winter. Because the Great Lakes lie in a general northwest-southeast line from Lake Superior to Lake Ontario, this means that the same air mass may pass over more than one lake. As it does so, the thermodynamic properties of this air mass become modified by each lake in succession, potentially triggering lake-effect convection over each lake it passes over. How this convection alters the convective environment and dynamics over the downwind lakes is still unclear, despite numerous modeling and observational studies demonstrating that convection can often "connect" between upstream and downstream lakes in what is referred to as a "lake-to-lake" (L2L) connection.

To examine the role that upstream lakes and their induced convection play in altering the convective environment and behavior of convection over downwind lakes, I used the Regional Atmospheric Modeling System (RAMS) to simulate a lake-effect snow event which produced snow downwind of Lake Erie from 1-7 January 2010. To assess the impact of Lake Huron, an upstream lake, on the development and impacts of lake-effect convection over Lake Erie, a downwind lake, I conducted two simulations, one control simulation and one in which Lake Huron was replaced with a mixed forest. The results of the first study comprising this thesis are to be submitted to Monthly Weather Review [1].

The second phenomenon, coastal deep convection, occurs when the convective environment is favorable and a source of lifting for convection initiation is present. A common source of lifting in the coastal environment is the sea breeze, a circulation which develops between the warmer land and cooler ocean during the daytime. In response to the developing baroclinic circulations, the cooler, higher-pressure air over the ocean pushes inland, causing convergence and lifting at the boundary between the ocean-influenced air and the land-influenced air.

While the role of sea breezes has long been understood in convection initiation, it is not the only circulation which arises from contrasts in land surface properties. Numerous observational and modeling studies have highlighted that differential heating between areas of differing soil moisture and vegetation cover can induce circulations at the boundaries of these different land surface properties. Like the sea breeze, these land surface-induced circulations can provide a source of lifting which initiates convective storms. These circulations can also suppress convection, however. Previous studies have indicated that these land surface-induced circulations favor the development of convection and precipitation over relatively drier and hotter land surfaces while suppressing it over cooler and wetter land surfaces.

Despite knowledge of these two important mesoscale circulations (the sea breeze and land surface-induced circulations), and the role of each in convection initiation and evolution, the inter-

[1] Ascher, B.D., S.M. Saleeby, P.J. Marinescu, and S.C. van den Heever, 2024: Lake Huron Enhances Snowfall Downwind of Lake Erie: A Modeling Study of the 2010 New Year's Lake-Effect Snow Event. To be submitted to Mon. Wea. Rev.

action of the two has not been studied in detail. However, many coastal locations have heterogeneous adjacent land surfaces. For instance, the area around Houston, TX, in which the Experiment of Sea Breeze Convection, Aerosols, Precipitation, and Environment (ESCAPE) field campaign was conducted in 2022 to study the influence of the environment and mesoscale circulations on sea breeze convection, contains many different land surfaces close to the coast (Kollias et al., 2023). The interaction of circulations which arise on the boundaries of these land surfaces and the sea breeze circulation may affect the development of convective storms and rainfall differently than a uniform land surface adjacent to the coast would.

In addition, the role of cold pools in affecting these land surface-induced circulations is unclear. Cold pools, which arise from evaporation of precipitation and subsequent sinking of the cooler, dense air, can create their own wind circulations in the lower boundary layer. The interaction of these cold pool circulations with the land surface-induced circulations, and the combined impacts of these two circulations on future convective storm development, has received little attention.

To analyze the interaction between the sea breeze, land surface-induced circulations, and cold pools in a situation like that of Houston, I conducted idealized RAMS simulations in a coastal setting. Three of these simulations used uniform land surface types, while three used a striped pattern of land surface thereby representing land surface heterogeneity. The results of the second study are to be submitted to the Journal of the Atmospheric Sciences [2].

Together, these two studies examining the interactions of the land surface and convection will advance fundamental knowledge of the role of land surface processes in affecting convection initiation and development. They may also lead to improvements in our future ability to predict the occurrence and impacts of convective storms.

[2]Ascher, B.D., S.M. Saleeby, P.J. Marinescu, and S.C. van den Heever, 2024: Forest Breezes Enhance Convection over Heterogeneous Land Surfaces. To be submitted to J. Atmos. Sci.

Chapter 2

The New Year's 2010 Lake-Effect Snow Event

2.1 Introduction

For the heavily-populated Midwest and Northeast regions of the United States, lake-effect snow, which occurs when very cold air from the Canadian Arctic surges south over the unfrozen Great Lakes, can unleash havoc for local communities, infrastructure, and transportation (Niziol, 1987; Rose, 2000). Although estimating the exact population affected each year by lake-effect snow events is difficult, the presence of large urban areas such as Cleveland, OH, Erie, PA, Syracuse, NY, and Buffalo, NY within prominent lake-effect snow belts ensures significant population exposure to these hazards (Niziol, 1987; Kunkel et al., 2002). As was tragically seen in the 23-26 December 2022 winter storm in Buffalo, NY, these events can cause loss of life even in communities accustomed to intense winter weather (Kilgannon et al., 2022).

The Great Lakes comprise large lakes (Lakes Superior, Huron, Michigan, Erie and Ontario, listed from largest to smallest) in the northern United States and southern Canada (Figure 2.1). Because of their immense sizes, they can remain unfrozen throughout much of the winter season, thus creating large sensible heat fluxes which allow convective instability and favorable conditions for lake effect snow as cold Arctic air passes over the warm lakes.

Lake-effect snow events are sensitive to the size and shape of the lake over which they occur, as well as the direction of the wind over the lake (Gowan et al., 2021; Kristovich and Steve, 1995). Over long, oval-shaped lakes such as Lake Erie, Lake Ontario, and Lake Michigan, considerably different types of convection ("convection" in this chapter will refer to shallow lake-effect convection, unless otherwise specified) are observed when the near-surface wind is parallel to the long axis of the lake compared to when it is perpendicular to the long axis of the lake.

When winds are parallel to the long axis of the lake, Long-Lake Axis Parallel (LLAP) bands form. These convective bands are narrow (20-50 km across), have strong secondary circulations

with updrafts of $5\ \mathrm{m\ s^{-1}}$, and can produce heavy localized snowfall (Niziol et al., 1995; Bergmaier and Geerts, 2020; Bergmaier et al., 2017). While these events are most commonly seen over Lake Ontario (Figure 2.1), they also occur although less frequently over Lake Erie and Lake Michigan (Kristovich and Steve, 1995; Laird et al., 2017). There is usually one dominant LLAP band, with weaker auxiliary convective bands around it (Steenburgh and Campbell, 2017). The narrowness of LLAP bands means that only a few miles can separate areas of very heavy snowfall from areas of little to no snowfall. The deadly and destructive blizzard which occurred in Buffalo between 23-26 December 2022 was a catastrophic example of a strong LLAP band which formed under southwesterly flow over Lake Erie (Kilgannon et al., 2022).

Conversely, when winds are perpendicular to the long axis of the lake, wind-parallel bands (WPB) form (Laird et al., 2003). These bands are narrower (widths 5-20 km) and weaker than LLAP bands (Niziol et al., 1995). Unlike LLAP band cases, where a single strong band (hereafter, "band" or "bands" will refer to convective bands of the type found in WPB or LLAP lake-effect convection) dominates, WPB cases have many small bands present over the lake (Laird et al., 2003; Yang and Geerts, 2006). These bands individually have lower snowfall rates than LLAP bands; however, the greater number of them means that the areal coverage of snowfall is often greater than LLAP events. Over Lake Erie, the focus of this study, Rodriguez et al. (2007) and Laird et al. (2017) found that WPB were the most common type of lake-effect clouds which developed during the cool season.

An example of the LLAP and WPB types of lake-effect convection can be seen in Figure 2.1, captured by GOES-16 and provided courtesy of the Cooperative Institute for Research in the Atmosphere (CIRA) (Cooperative Institute for Research in the Atmosphere, 2022). In this image, captured on 25 January 2022, WPB are present over Lakes Superior and Michigan, while a LLAP is visible over Lake Ontario. Both types of convection are visible over Lake Huron, while WPB convection is present over Northeast Lake Erie.

Typically the cold air masses which produce lake-effect snow over the Great Lakes are associated with northerly, northwesterly, or westerly winds (Niziol et al., 1995; Hjelmfelt, 1990). The

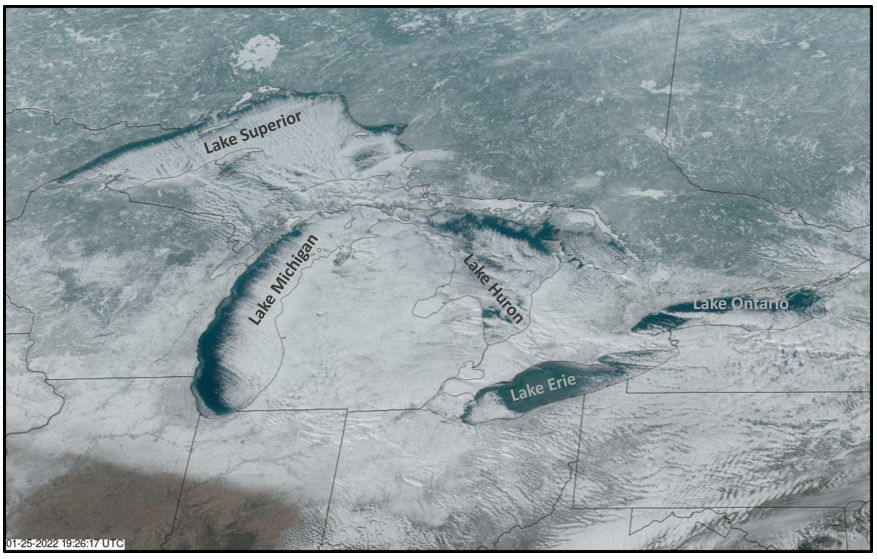

Figure 2.1: A variety of lake-effect cloud morphologies over the Great Lakes on 25 January 2022 as seen by GOES-16, provided courtesy of the Cooperative Institute for Research in the Atmosphere (Cooperative Institute for Research in the Atmosphere, 2022). Wind-Parallel Bands (WPB) are seen over Lakes Superior and Michigan, while a Long Lake Axis-Parallel (LLAP) band can be seen over Lake Ontario.

relative location of the lakes often leads to the same cold airmass passing over more than one lake (Rodriguez et al., 2007). This passage over multiple lakes creates what is known as a Lake-to-Lake (L2L) connection, in which the near-surface air is modified by the upstream lake before encountering the downstream lake (Kristovich et al., 2018; Hjelmfelt et al., 2004). Previous modeling studies which have looked at certain aspects of L2L snowfall events have revealed that L2L connections increase snowfall over the downwind lake by warming, moistening, and deepening the planetary boundary layer (Rose, 2000; Sousounis and Mann, 2000; Mann et al., 2002; Hjelmfelt et al., 2004; Wright et al., 2013).

Rodriguez et al. (2007) used visible satellite imagery to identify L2L events from 2000-2004. They found that the most common L2L connections are Lake Superior-Lake Michigan, Lake Superior-Lake Huron, Lake Huron-Lake Erie, and Lake Huron-Lake Ontario. Using a 17-year satellite record, Laird et al. (2017) found similar results to those of Rodriguez et al. (2007).

Evidence of lake-to-lake enhancement has also been seen in observational studies of lake-effect events. Villani et al. (2017) examined radar, satellite, and modeled sounding data to identify

predictors of the inland extent of lake-effect snowfall. They found that the existence of an L2L connection (referred to in their paper as a Multi-Lake Connection, or MLC) was strongly associated with snowfall propagating far inland of the lake. Using visible satellite imagery to identify L2L events over Lake Ontario, and the National Operational Hydrologic Remote Sensing Center's Snow Data Assimilation System (SNODAS) to estimate daily snowfall, Lang et al. (2018) noted that L2L WPB events produced up to 160% greater snowfall in parts of Western New York than single-lake WPB events. Kristovich et al. (2018) used airborne and surface observations from the Ontario Wintertime Lake-effect Snowstorm (OWLeS) campaign to evaluate the impact of Lake Erie on banded lake-effect convection over Lake Ontario. They concluded that convective bands grew deeper with greater precipitation rates within a "plume" stretching from Lake Erie to Lake Ontario, compared with bands over Lake Ontario outside of the plume.

Together, these studies paint a fairly consistent picture of L2L enhancement. They indicate that upwind lakes modify the convective environment over the downwind lake, raising the PBL (although Kristovich et al. (2018) found some counter-intuitive observational results suggesting that they may actually lower the PBL near the upwind shoreline of the downwind lake), temperature, and humidity near the surface. Multiple studies suggest that this "preconditioning" allows for stronger and deeper banded lake-effect convection over the downwind lake, enhancing precipitation relative to what would be expected with no upwind influence (Rose, 2000; Sousounis and Mann, 2000; Mann et al., 2002; Niziol et al., 1995; Hjelmfelt et al., 2004). However, while these studies have revealed the significant effects that upwind lakes have on the overall convective environment, they have not addressed in detail the effects of upwind lakes and their associated convective bands on the storm-scale dynamics over the downwind lake.

Finally, Niziol (1987) highlighted that a minimum overwater fetch of 80 km was generally required for the formation of precipitation in lake-effect systems. However, the long aspect ratio of Lakes Michigan, Erie, and Ontario means that, under northwesterly winds, there is often less than 80 km of fetch available for air parcels traveling over the lake. Yet, these conditions are still associated with heavy snowfall downwind of these lakes. These same conditions often lead to L2L

connections, suggesting that the minimum required fetch for heavy snowfall under L2L conditions may be shorter than 80 km (Rose, 2000; Mann et al., 2002). Kristovich and Laird (1998) noted that lower levels of static stability on the upwind side of a lake accelerated the development of lake-effect convection. Although Kristovich and Laird (1998) did not look specifically at lake-to-lake events, the work of Rose (2000); Sousounis and Mann (2000); Hjelmfelt et al. (2004) would suggest that modification of air by upwind lakes, via increased temperature and moisture and reduced static stability, would likewise accelerate the development of convection over a downwind lake. As such, a major aim of this study will be to examine the impacts of upwind lakes on the storm-scale dynamics occurring over the downwind lake.

The goal of this study is to examine the processes responsible for L2L enhancement on the scale of individual convective bands. Specifically, this study will address the following questions: 1). Does the presence of a large upwind lake enhance snowfall over and downwind of a short-fetch lake? 2). If so, what are the storm-scale processes responsible for this enhancement?

2.2 Event Description

To examine the impact of large upwind lakes on short-fetch downwind lakes, I chose the 1-6 January 2010 lake-effect snowstorm. This long-duration lake-effect snow event began with a Continental Arctic airmass on the east side of the Canadian Rockies at 12 UTC on 1 January 2010. Aloft, a 500 mb trough located over Northwestern Ontario slowly began to move southeast over the Great Lakes. As it did so, a strong cold front moved through the East Coast of the United States around 00 UTC on 2 January. In the wake of this cold front, northwesterly flow developed, increasing in strength through the morning of 2 January. Meanwhile, the Arctic airmass moved south over Ontario and spilled south across the Eastern US, bringing subfreezing temperatures southward to northern Mississippi and coastal North Carolina. At the same time, the 500 mb trough moved southeast and deepened, developing a closed upper-level low with heights less than 5220 m over Pennsylvania and New York by the night of 2 January (Figure 2.2a). This trough intensified an extratropical cyclone off the coast of Nova Scotia. The strong pressure gradient between the low to

the northeast and the high to the northwest led to the strengthening of cold northwesterly low-level winds over the eastern Great Lakes (Figure 2.2c,d). By the night of 2 January, 850 mb winds were approximately 25 kts from the northwest, and 850 mb temperatures over the Great Lakes were between -21 and -23 °C (Figure 2.2c). Lake Huron's surface temperature was approximately 4 °C while Lake Erie's average surface temperature was approximately 2 °C (NOAA, 2020). As a result, there was a 23-27 °C difference between lake surface temperature and 850 mb, sufficient to establish lake-effect convection (Niziol, 1987).

Lake-effect convection developed on the morning of 2 January and intensified through the afternoon and early evening. Heavy snow fell over much of NW PA and W NY through the morning of the 4 January. By this time a blocking pattern had set up and the surface low remained stalled offshore of Nova Scotia. This continued the pattern of cold northwesterly flow and allowed lake-effect snow to continue for the next few days, though weakening in intensity after 4 January. Between 1-6 January 2010, Erie International Airport reported 16.1 inches (40.9 cm) of snow, while a Community Collaborative Rain, Hail, and Snow network (CoCoRaHS) station 5.6 miles to the southwest reported 31.0 inches (78.7 cm) of snow over the same period. Snowfall reports from the National Operational Hydrologic Remote Sensing Center (NOHRSC) indicate that a broad swath from Cleveland, OH to Oswego, NY received in excess of 30 inches (76 cm) of snow from 1-6 January, with portions of NW PA and SW NY receiving >45 inches (114 cm) (Figure 2.3a). The event finally came to an end early on the morning of 7 January, as southerly flow across the Great Lakes region brought higher temperatures, eliminating the instability necessary for lake-effect convection.

Though the 1-6 January 2010 storm was a long-lived event spanning several days, the overall pattern of flow and structure of lake-effect convection remained almost stationary during that time. The northwesterly flow setup promoted an L2L between Lake Huron and Lake Erie, the focus of this study. To examine the processes responsible for the establishment and maintenance of this L2L, I modeled the first two days of the lake-effect event, from 12 UTC 1 January 2010 to 12 UTC

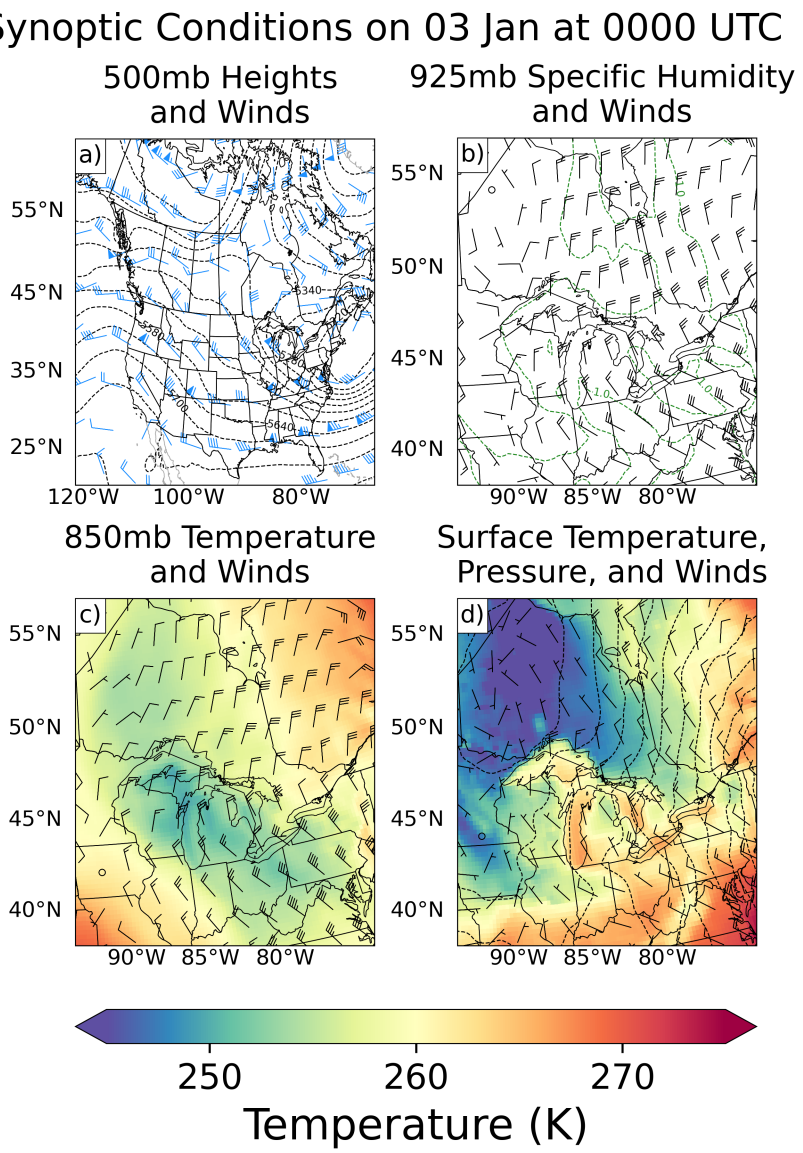

Figure 2.2: Synoptic weather conditions from ERA5 at 0000 UTC 3 January 2010, 1 hour after the time examined in Figures 2.8 through 2.12 (Hersbach et al., 2020). A deep 500 mb trough over the Great Lakes and Northeast regions and an associated extratropical cyclone brought cold northwesterly flow over the Great Lakes. (a) depicts 500 mb geopotential height in meters, with 500 mb winds plotted as blue barbs. (b) shows the 925 mb winds in black barbs, with isosurfaces of specific humidity in green dashed lines. (c) and (d) show temperature and winds at 850 mb and the surface, respectively. (d) also shows the mean sea level pressure in black dashed contours.

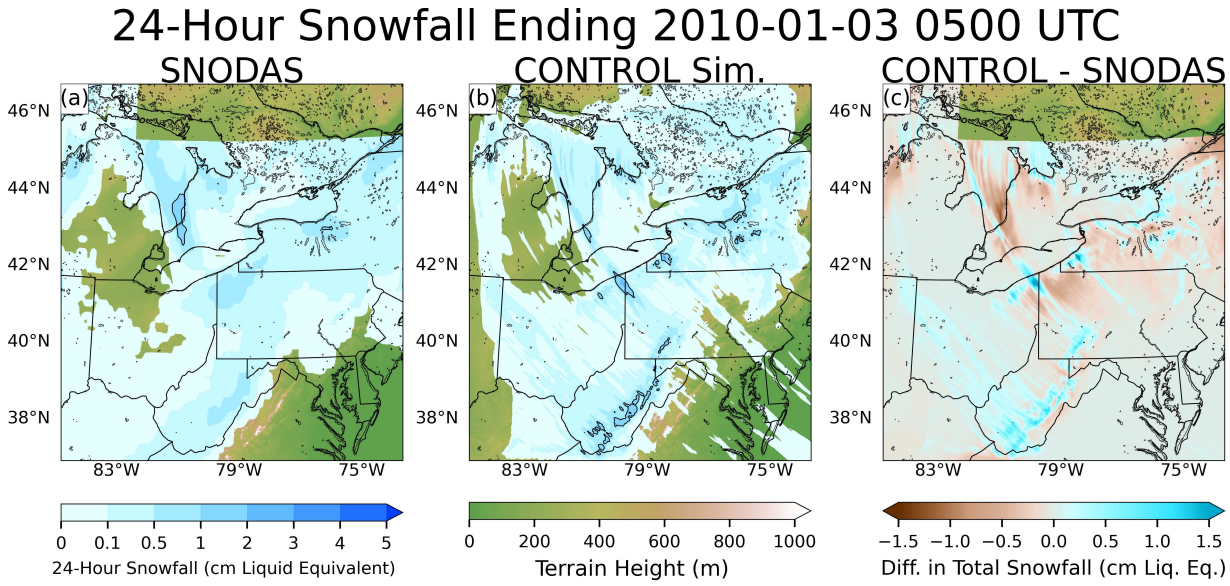

Figure 2.3: 24-Hour Snowfall Liquid Equivalent from 0500 UTC on 2 January to 0500 UTC on 3 January, with estimates from the Snow Data Assimilation System in (a), from RAMS model CONTROL simulation in (b), and the difference between the two in (c). The green and brown shading indicates terrain height, the thin black contour indicates water bodies, and the thick black contour in (a) and (b) indicates areas of > 1 cm liquid equivalent of snowfall. The block of no data in the northeast portions of (a) and (c) is an artifact of SNODAS, which did not include snow data in that region for the time of interest.

3 January 2010. Given the quasi-stationary flow pattern, the two-day simulation period I conducted is sufficient to examine the processes at play during the six-day storm.

2.3 Experiment Design

I simulated this event with the Regional Atmospheric Modeling System (RAMS), a nonhydrostatic, cloud-resolving model (Cotton et al., 2003). For this study, RAMS was run with the Land-Ecosystem-Atmosphere Feedback (LEAF-3) surface model developed by Walko et al. (2000). In an attempt to isolate the effect of Lake Huron on snowfall downwind of Lake Erie, I conducted two simulations: a CONTROL simulation to recreate the conditions observed between 1-3 January 2010 and an NLH (No Lake Huron) simulation in which Lake Huron was removed. The simulation domains were a polar stereographic grid extending roughly from 37°N to 47°N and 86°W to 74°W (Figure 2.4).

I ran these simulations on a single grid with 1 km horizontal spacing and variable vertical spacing, from 30 m near the surface to a maximum of 300 m aloft. I chose a 1 km horizontal grid spacing as a compromise between allowing for a sufficiently large domain on a and adequately resolving the band morphology and associated processes. Jensen et al. (2020) showed that 1.33 km horizontal grid spacing was sufficient to capture the morphology and snowfall patterns of LLAP lake-effect snow bands, and their results implied that band dynamics are dominated by processes resolvable with $O(1\ \mathrm{km})$ simulations. While LLAP bands are wider than the WPBs which are the focus of this study (20-50 km vs 5-20 km), even narrow WPBs should be resolvable with 1 km grid spacing, given that the minimum resolvable feature size at 1 km horizontal grid spacing is 4 km (4 times the horizontal grid spacing). Wright et al. (2013) also found that their 1 km grid spacing was sufficient to capture the evolution of snow bands and the distribution of precipitation. I chose a vertical grid spacing of 30 m near the surface in an attempt to capture superadiabatic temperature structures and mesoscale circulations just above the lake surface.

Both the CONTROL and NLH simulations were initialized and nudged at the lateral boundaries with the fifth-generation ECMWF ReAnalysis (ERA5) temperature, pressure, humidity, and

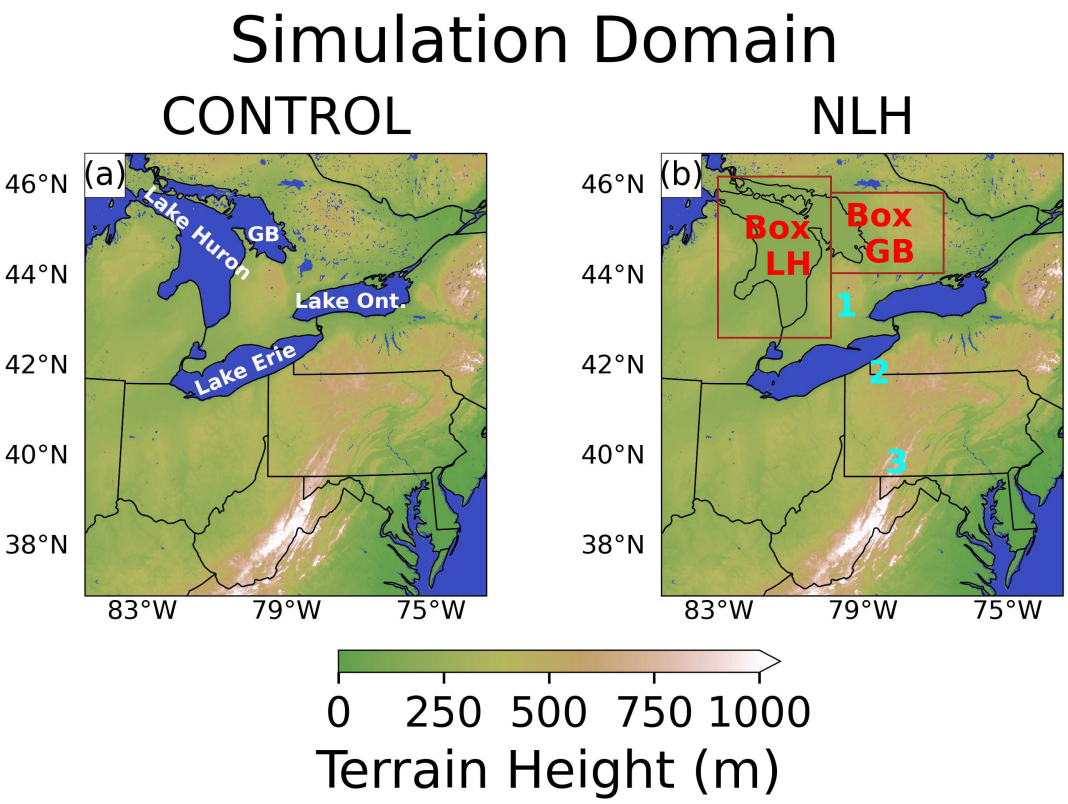

Figure 2.4: Lake-effect snow simulation domains. Terrain height is shown in the green-white shading, while water bodies are shown in light blue. Major Great Lakes in the CONTROL simulation are labeled (Georgian Bay, the easternmost part of Lake Huron, is denoted by "GB"). Note that Lake Huron is not present in the NLH simulation. "BOX LH" and "BOX GB" indicates the box used to modify variables over and downwind of Lake Huron and Georgian Bay, respectively. The cyan numbers 1, 2, and 3 highlight the Ontario Peninsula, the Allegheny Plateau on the PA/NY border, the Laurel Highlands in SW PA, respectively.

Table 2.1: Model Parameter Settings for the CONTROL and NLH Simulations.

Model Parameter	Value
Grid	Arakarwa C-Grid Arakawa and Lamb (1977)
Horizontal Grid Spacing (km)	1
Horizontal Domain	1100 x 1000
Vertical Grid Spacing (m)	Stretched (30-1000)
Vertical Levels	90
Timestep (seconds)	2
Simulation Duration (hours)	48
Initialization and Boundary Nudging	ERA5 Hourly Data on Pressure Levels (Hersbach et al., 2020)
Horizontal Boundary Scheme	Radiative (Klemp and Wilhelmson, 1978)
Upper Boundary Conditions	Rigid Model Top at 18 km.
Surface Model	LEAF-3 (Walko et al., 2000)
Land Cover	1 km OGE Data
Soil Type	1 km FAO Data
Soil Levels	11 Levels from -0.5m to -0.01m
Snow Levels	5 (prognostic thickness)
Water Temperature	1 ° global reanalysis Reynolds et al. (2002)
Microphysics Scheme	Two-moment bulk microphysics with 8 hydrometeor species (Saleeby and Cotton, 2004)
Radiation Scheme	Two-stream radiation, with tendencies updated every 10 minutes (Harrington, 1997)
Aerosol Initialization	$\frac{450}{cm^3}$ at surface, decreasing exponentially with height (Saleeby and van den Heever, 2013)
Aerosol-Radiation Direct Effects	None
Aerosol Sources and Sinks	None
Turbulence Scheme	(Smagorinsky, 1963) with modifications by (Hill, 1974) and (Lilly, 1962)

wind data (Hersbach et al., 2020). In addition, the lower boundaries of both simulations were initialized with ERA5 soil moisture, soil temperature, and snow cover data (although the NLH simulation required modifications to these fields, as discussed below). Full model settings for both simulations are shown above in Table 2.1. Water bodies in the simulations were initialized with a 1 ° resolution global water temperature reanalysis (Reynolds et al., 2002). I also set all lakes to be fully open water in our simulations, even though partial ice cover was present on some of the lakes (NOAA, 2020). I should note that while full ice cover does strongly suppress lake-effect convection, most ice coverage over the Great Lakes at this time was under 10%, which Wright et al. (2013) and Fujisaki-Manome et al. (2020) noted only slightly suppresses latent and sensible heat fluxes compared to open water. However, the presence of thick ice over western Lake Erie, Saginaw Bay, and northeast Georgian Bay likely eliminated most latent and sensible heat fluxes in those areas, which our simulations did not account for. While it is possible that this artificial inclusion of open water in Saginaw Bay and Georgian Bay may have induced weak lake-effect circulations, I saw very little difference in thermodynamics and dynamics in these regions between the CONTROL and NLH simulations, suggesting that the influence of these areas of open water and associated circulations was marginal on the processes involved elsewhere in the domain.

To remove Lake Huron in the NLH simulation, I made several modifications to the land surface and initial surface variable fields in the model. LEAF-3 uses subgrid "patches" to model land surface (Walko et al., 2000). This means that a single horizontal grid cell can contain several patches of different land surface type which are proportional to the fraction of the cell area that these land surface types comprise in the raw surface data files. This is done in an attempt to capture land-surface heterogeneity with grids of coarser resolution. In the case of the CONTROL and NLH simulations, I only needed two patches per grid cell: a water patch and a land patch. As shown in Figure 2.4b, I created two boxes, one around the main body of Lake Huron (roughly 42.8 °N to 46.4 °N, 84.3 °W to 80.0 °W, denoted by LH) and one over and east of Georgian Bay (roughly 44.3 °N to 46.0 °N, 81.0 °W to 77.6°W, denoted by GB). Within these boxes, the water patch fraction of each model grid cell was set to 0, while the land patch fraction was set to 1 (no permanent water

surfaces in the grid cell). While there are several different land surface types surrounding Lake Huron, the principal land surface types are mixed deciduous-coniferous forest along the Northern Michigan and Northern Ontario shorelines, and cropland along the southern Lower Michigan and Ontario Peninsula shorelines. For simplicity, I assigned a mixed forest land surface type to the entire region replacing the lake, although this is admittedly more representative of the land cover adjacent to the northern half of the lake than to the land cover adjacent to the southern half of the lake.

In addition to modifications of land cover, four other variables, Normalized Difference Vegetation Index (NDVI), soil water content, soil temperature, and Snow Water Equivalent (SWE), had to be modified over and downwind of Lake Huron in NLH. The NDVI over the former lake surface was set to the average NDVI value of mixed-forest land north of 44N (excluding the subtropical mixed forests of the Mid-Atlantic). Similarly, soil water content, soil temperature, and SWE were filled in with their average value found along the upwind (northwest) Lake Huron shoreline. Unlike for NDVI, which was modified just over water patches within the LH and GB boxes shown in Figure 2.4b, I altered soil temperature and Snow Water Equivalent throughout the entirety of the boxes, including both land and water patches. The reason for this is that Lake Huron's presence modifies the amount of snow cover both over *and downwind* of the lake. I wanted to completely remove the influence of Lake Huron on the environment as much as possible, so I tried to match soil and snow conditions downwind of Lake Huron with those found upwind of the lake.

Both simulations were run from 12 UTC 1 January 2010 to 12 UTC 3 January 2010. However, the first 12 hours of the simulation are considered a model spin-up period and are not considered in this analysis.

2.4 Results

Snowfall in the CONTROL simulation was validated against the Snow Data Assimilation System (SNODAS) modeled precipitation at 1 km horizontal grid spacing from that time period (National Operational Hydrologic Remote Sensing Center, 2004). It's important to note that while

SNODAS assimilates observations of snowfall and SWE, it is itself a model as opposed to a true observational dataset. However, there were few measurements of SWE in this region for this event, and there was a particular gap in measurements downwind of Lake Erie, which is the focus area of this study. As such, I chose to compare RAMS estimates of accumulated SWE from the CONTROL simulation with those of SNODAS.

As Figure 2.3a,b shows, the RAMS CONTROL simulation captures the overall spatial pattern of snowfall downwind of Lake Erie, although coverage of 1 cm liquid equivalent of snowfall (the thick black contour in Figure 2.3) downwind of Lake Erie is present in CONTROL and absent in SNODAS. Compared to SNODAS, the simulation underestimates snowfall over Central Pennsylvania. Snowfall amounts are overestimated compared to SNODAS over the Laurel Highlands in Southwestern Pennsylvania, with an average of ~ 4.1 mm liquid equivalent in the simulation vs ~ 2.4 mm liquid equivalent in SNODAS (Figure 2.3c). Differences in exact snowfall amounts notwithstanding, the CONTROL simulation depicts similar coverage and location of lake-effect snowfall to that of SNODAS.

There are two main phenomena that I will focus on in this chapter: the main L2L band which makes landfall in extreme northeast OH and a small area of intense banding in extreme southwest NY downwind of northeast Lake Erie. Note that in this section, I will first describe the differences in snowfall between the CONTROL and NLH simulations across the entire simulation domain, highlighting regions of particular interest. I will then describe the process responsible for snowfall in these areas.

For ease of reference, I constructed boxes, shown in Figure 2.5d-f which roughly parallel these features. Region B corresponds to the area of heavy snowfall produced by the main L2L band, while Region D corresponds to the area of heavy snow produced by the intense banding in the northeast part of Lake Erie. I should emphasize that these boxes are subjectively constructed and *descriptive*; they just outline areas of heavy snow and do not define areas of dynamic or microphysical behavior. While snow totals described below are obtained from averages over these boxes, will discuss the *dynamics* without reference to these boxes. Region A in Figure 2.5 encompasses the re-

gion downwind of Lake Erie where large differences in snowfall are seen between the CONTROL and NLH simulations. Region C refers to the region between the main L2L band (Region B) and the northeast bands (Region D), where much less snowfall is seen in the CONTROL simulation compared to the NLH simulation. Note that in Figure 2.5 and following plan view figures, the outline of Lake Huron in the NLH simulation indicates where Lake Huron *would have been*, and serves to help orient the reader. In the NLH simulation, however, the area corresponding to Lake Huron has been replaced with land, not water (Figure 2.4).

Downwind of Lake Erie (calculated as an average over Region A), total snowfall in the NLH simulation is $\sim 16\%$ lower than in the CONTROL simulation, with mean accumulated snowfall downwind of Lake Erie of ~ 1.57 mm liquid equivalent in NLH compared to ~ 1.87 mm liquid equivalent in the CONTROL simulation. This is a result of weaker convective snow bands in the NLH simulation compared to the CONTROL simulation (discussed below). Even more striking, the narrow axis of heavy snow (Region B in Figure 2.5d) present in the CONTROL simulation is completely absent in the NLH simulation. In the CONTROL simulation, an average of ~ 8.70 mm liquid equivalent of snow fell in this small area in association with heavy snow from the main L2L band, more than 3 times the ~ 2.38 mm liquid equivalent which fell in the NLH simulation.

It is worth highlighting that in Region C (between Regions B and D in Figure 2.5d,e), the total snowfall is actually $\sim 65\%$ greater in the NLH simulation than the CONTROL simulation, with mean accumulated snowfall of ~ 3.52 mm liquid equivalent in NLH compared to ~ 2.18 mm liquid equivalent in CONTROL. The reason for this is the presence of more weak auxiliary bands in the NLH simulation over the northeast part of Lake Erie compared to the CONTROL simulation as seen in the time-averaged 700 m vertical velocity field in Figure 2.6b. Looking to Figure 2.7b,c, I see that average 700 m AMSL vertical velocities in northeast Lake Erie (where Distance Along Lake Erie is between 0 and 100 km) are slightly positive in the NLH simulation and slightly negative in the CONTROL simulation, indicating that lake-effect convection (and associated snowfall) in this area is more favored in the NLH simulation than the CONTROL simulation. The reasons

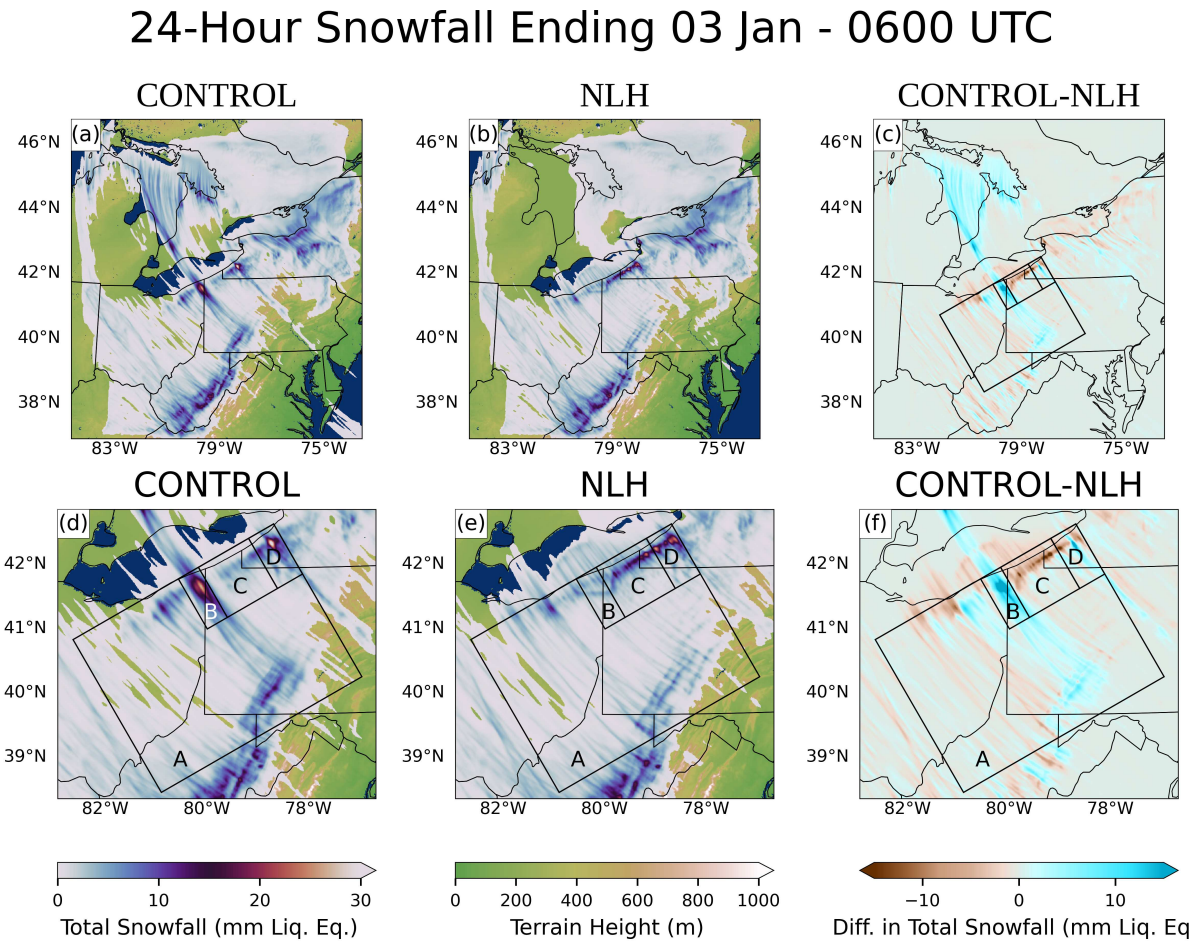

Figure 2.5: Comparison of 24-hour snowfall between CONTROL (a,d) and NLH (b,e) simulations. The difference in total snowfall, in mm. liquid equivalent, is plotted in (c,f). (d-f) show zoomed-in versions of (a-c) centered on the black boxes in (c). Regions of interest (discussed in the text) are shown in black boxes.

for this difference in the weak auxiliary bands between the CONTROL and NLH simulations are somewhat unclear.

In Region D, downwind of extreme northeast Lake Erie in Figure 2.5f, snowfall amounts are very similar between the CONTROL and NLH simulations. A mean snowfall of ~ 5.58 mm liquid equivalent is seen in the CONTROL simulation compared to a mean snowfall of ~ 5.19 mm liquid equivalent in the NLH simulation, a $\sim 7\%$ increase.

Figures 2.8 through 2.12 examine a snapshot in time at 1800 LT (2300 UTC) on 2 January. I chose to focus on this time as it is broadly representative of conditions and processes which were present at other times throughout the simulation, while also presenting a clearly visible strong main L2L band over the Ontario Peninsula (Figures 2.8a and 2.9a). As Figure 2.6 indicates, the behavior of lake-effect convection (as indicated by vertical velocity) at this time is representative of conditions in the 24-hour period between 0600 UTC 2 January and 0600 UTC 3 January.

Figure 2.7 further supports the use of 1800 LT as representative of the whole simulation. The main L2L band near the middle of Lake Erie, which is visible in Figure 2.7(b), the CONTROL simulation, but absent in Figure 2.7(c), the NLH simulation, does not vary much in location or strength throughout the simulation. Nor does the band in extreme northeast Lake Erie seen in the far right of (b) and (c) move much throughout the simulation.

Clear differences in thermodynamic conditions are visible between the NLH and CONTROL simulations (Figure 2.10). The boundary layer height is ~ 700 m lower in the NLH simulation compared to the CONTROL simulation. In the NLH simulation, the average boundary-layer air temperature over Lake Erie is ~ 3 K lower compared to the CONTROL simulation, while average dewpoints over Lake Erie are ~ 2.5-3 K lower in the NLH simulation than the CONTROL simulation (Figure 2.10). These differences in boundary-layer characteristics are in accordance with those of other L2L modeling experiments (Rose, 2000; Mann et al., 2002). These differences allow auxiliary convective bands in the CONTROL simulation to grow deeper than those in the NLH simulation, which has the counter-intuitive effect of reducing snowfall totals in Region C (Figure 2.5f) in the CONTROL simulation compared with the NLH simulation.

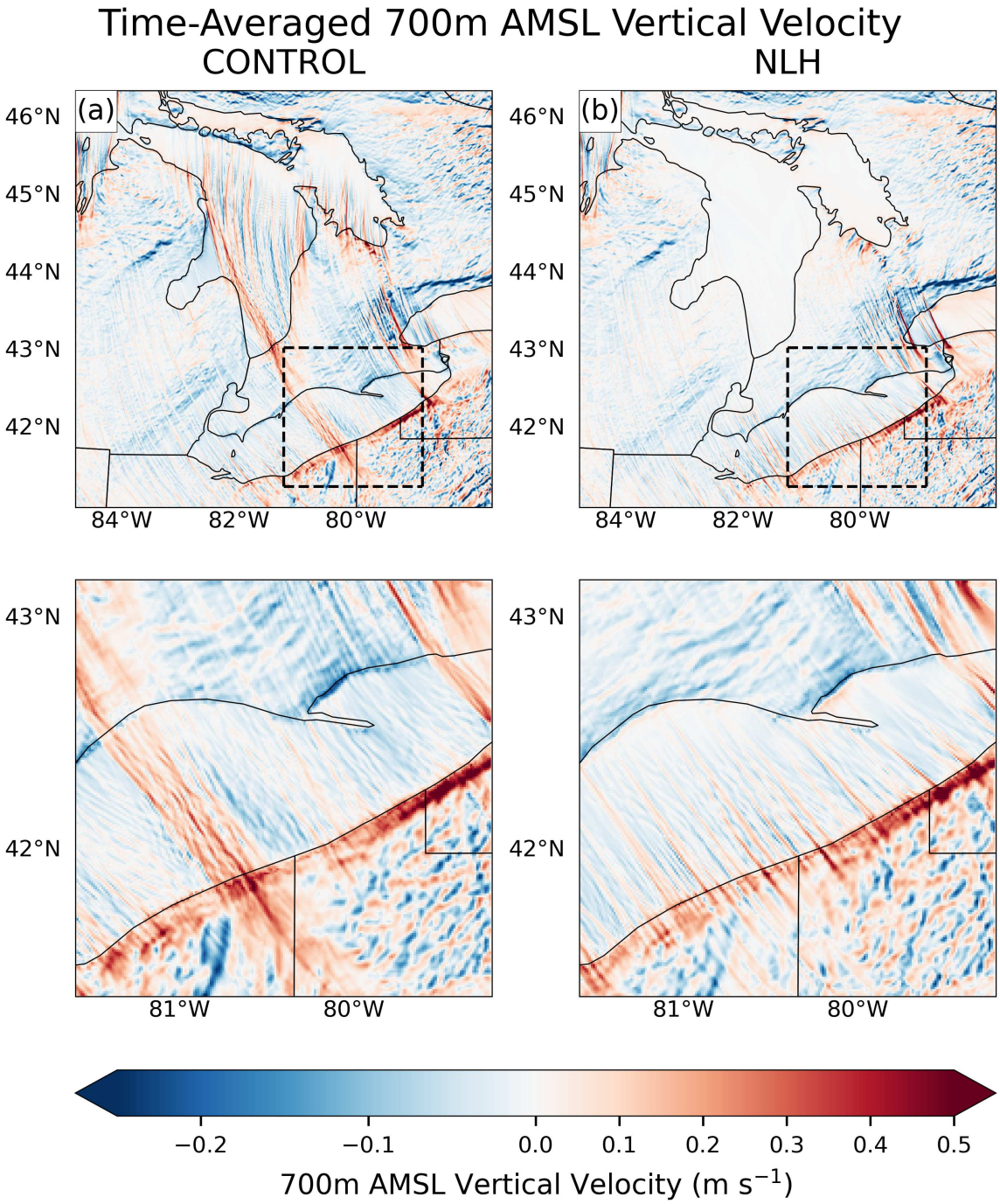

Figure 2.6: Time-averaged 700 m AMSL vertical velocity for the CONTROL simulation (a) and NLH simulation (b) between 0600 UTC 2 January and 0600 UTC 3 January 2010. The main L2L band stretching from Lake Huron to Lake Erie is clearly visible in the CONTROL simulation (a) but absent in the NLH simulation (b). (c,d) show zoomed regions over central Lake Erie (the dashed box in (a,b)), highlighting the presence of more auxiliary bands in the NLH simulation compared to the CONTROL simulation.

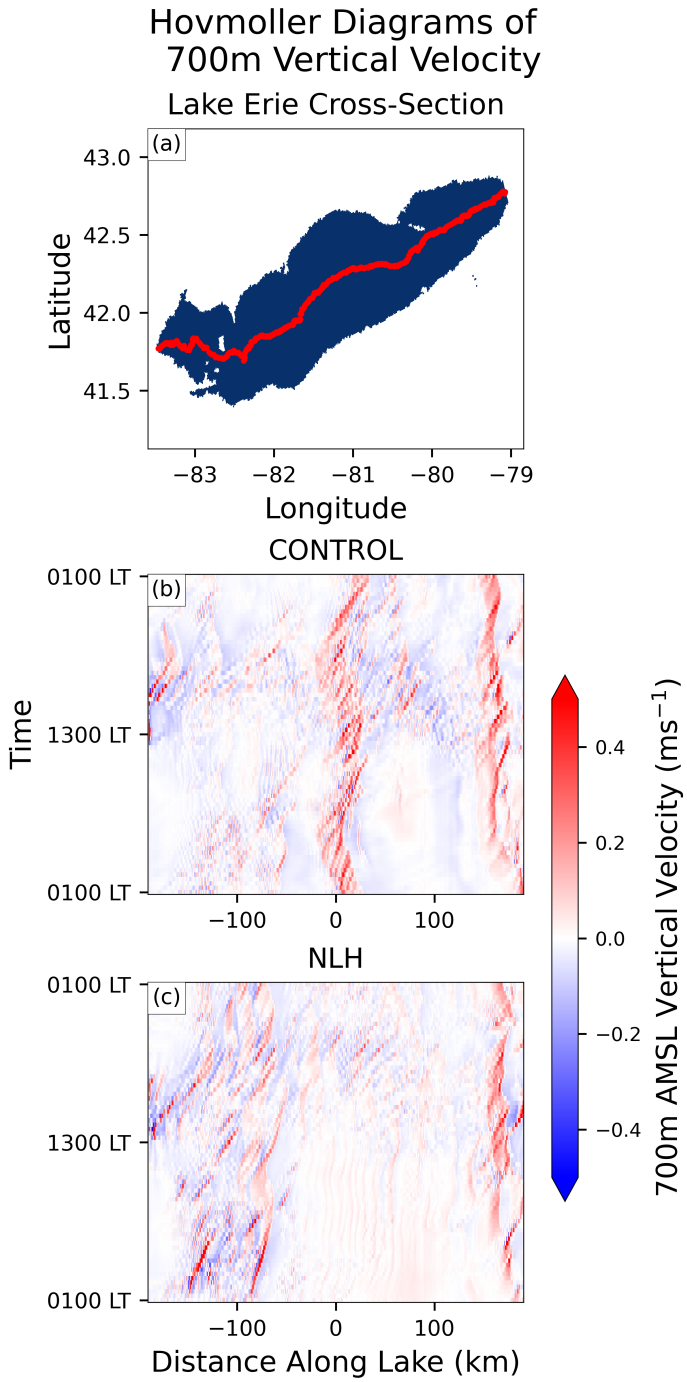

Figure 2.7: Hovmöller diagram of 700 m AMSL vertical velocity over Lake Erie, averaged along the minor axis of the lake. The main L2L band in the CONTROL simulation is visible as a persistent area of positive vertical velocity around 0 km in the "Distance Along Lake" in (b). The red line in Panel a indicates the midline of Lake Erie, which is approximately the path followed by the x-axis in panels b and c.

The differences in snowfall in Region B are due to the presence of a "main L2L band" in the CONTROL which is absent in the NLH simulation. Figure 2.8 shows instantaneous vertical velocity at 700 m AMSL at 1800 LT on 2 January 2010, during a period of intense lake-effect snowfall in the CONTROL simulation. A strong band stretching from Lake Huron to the southeast Lake Erie shoreline is clearly visible in CONTROL but missing in NLH. In the NLH simulation, weak lake-effect circulations (seen by areas of low-level convergence in Figure 2.9) begin to form less than 20 km southeast of the northwest shoreline of Lake Erie. These circulations intensify as air parcels move southeastward along the bands across Lake Erie, and reach 700 m AMSL vertical velocities of $\sim 1 - 1.5\ \mathrm{m\ s^{-1}}$. These are $\sim 50\%$-70% weaker than the $\sim 3\ \mathrm{m\ s^{-1}}$ updraft in the main band of the CONTROL simulation. Although the bands in the NLH simulation strengthen as air parcels within them traverse the lake, the short fetch of Lake Erie means that the air parcels within the bands move ashore before the bands attain the strength of the main band in the CONTROL simulation. In effect, the bands in the NLH simulation "run out of runway" before they can fully mature ("mature" in this chapter will refer to bands reaching a constant depth and maximum vertical velocity), leading to weaker vertical velocities and smaller snowfall rates immediately downwind of the lake compared to the CONTROL simulation. Another factor inhibiting the vertical development of the bands in the NLH simulation is the lower inversion height compared to the CONTROL simulation. In the NLH simulation, the boundary layer height above Lake Erie is ~ 700 m AMSL, compared to ~ 1400 m AMSL in the CONTROL simulation (Figure 2.10).

In contrast to the bands over Lake Erie in the NLH simulation, the main L2L band of the CONTROL simulation originates as one of several circulations over Northern Lake Huron. Like the NLH bands, it starts out weak and strengthens slowly as distance from the shore of Manitoulin Island (the large island in the north of Lake Huron) increases. As air parcels within the band move southeast over Lake Huron, a secondary circulation develops with horizontal convergence at 350 m and horizontal divergence at 2000 m AMSL (Figures 2.9a, 2.11b). As Bergmaier et al. (2017) found, the development of this secondary circulation promotes a positive feedback, as rising motion in the center of the band generates condensation and latent heat release, which in turn

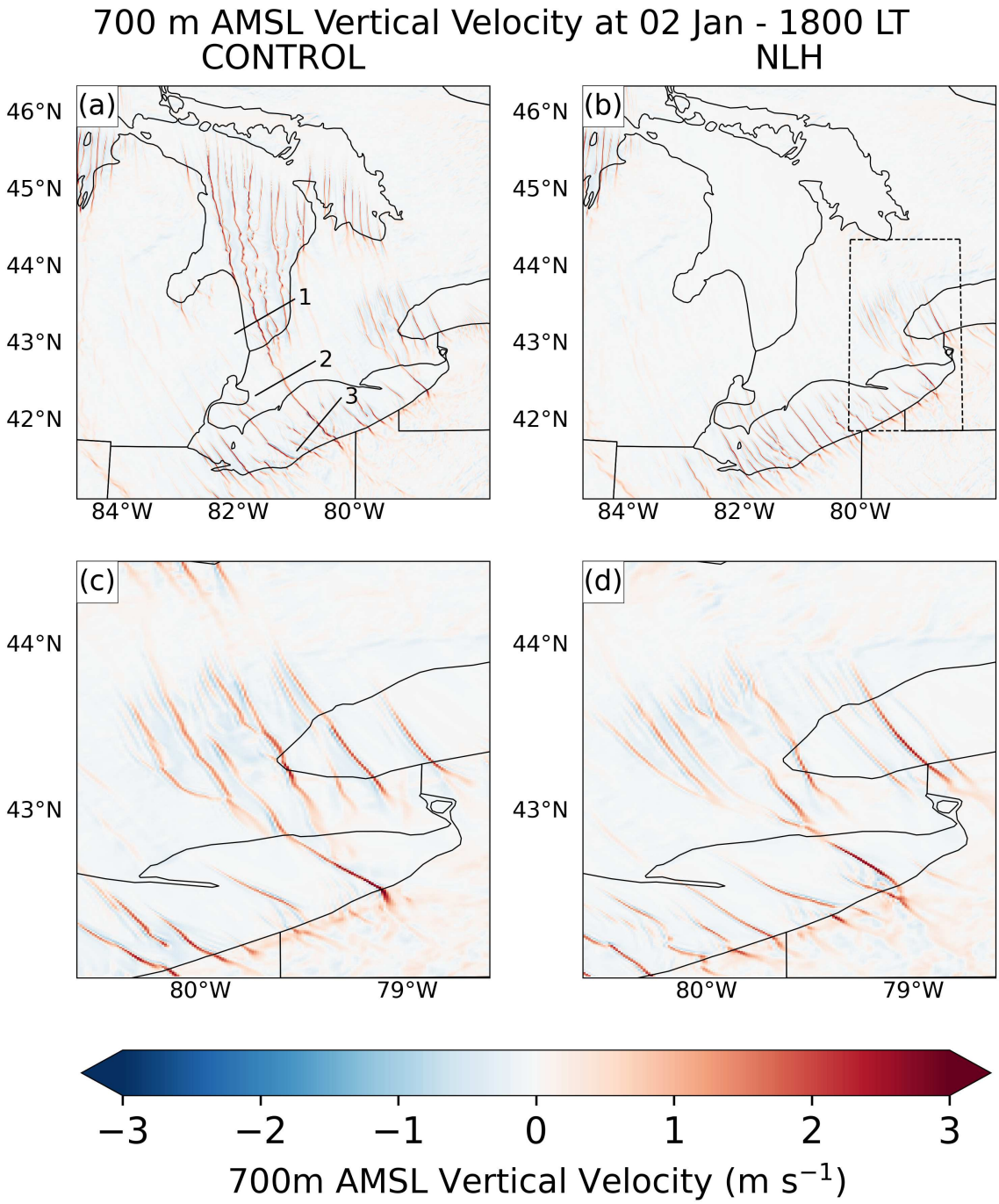

Figure 2.8: Simulated vertical velocity at 700 m above mean sea level at 1800 LT on 2 January. A single dominant band of high vertical velocity is present in the CONTROL simulation but absent in the NLH simulation (a,b). In both simulations, bands of vertical velocity are visible northwest of Lake Ontario and in extreme northeast Lake Erie (c,d). The locations of the vertical cross-sections in Figure 2.11 are shown in (a), with numbers corresponding to their respective cross-sections in Figure 2.11. (a,b) show the area from Lake Huron to just south of Lake Erie, while (c,d) show a zoomed-in view of the snow-free area west of Lake Ontario. This area plotted in (c,d) is marked in (b) with a dashed square.

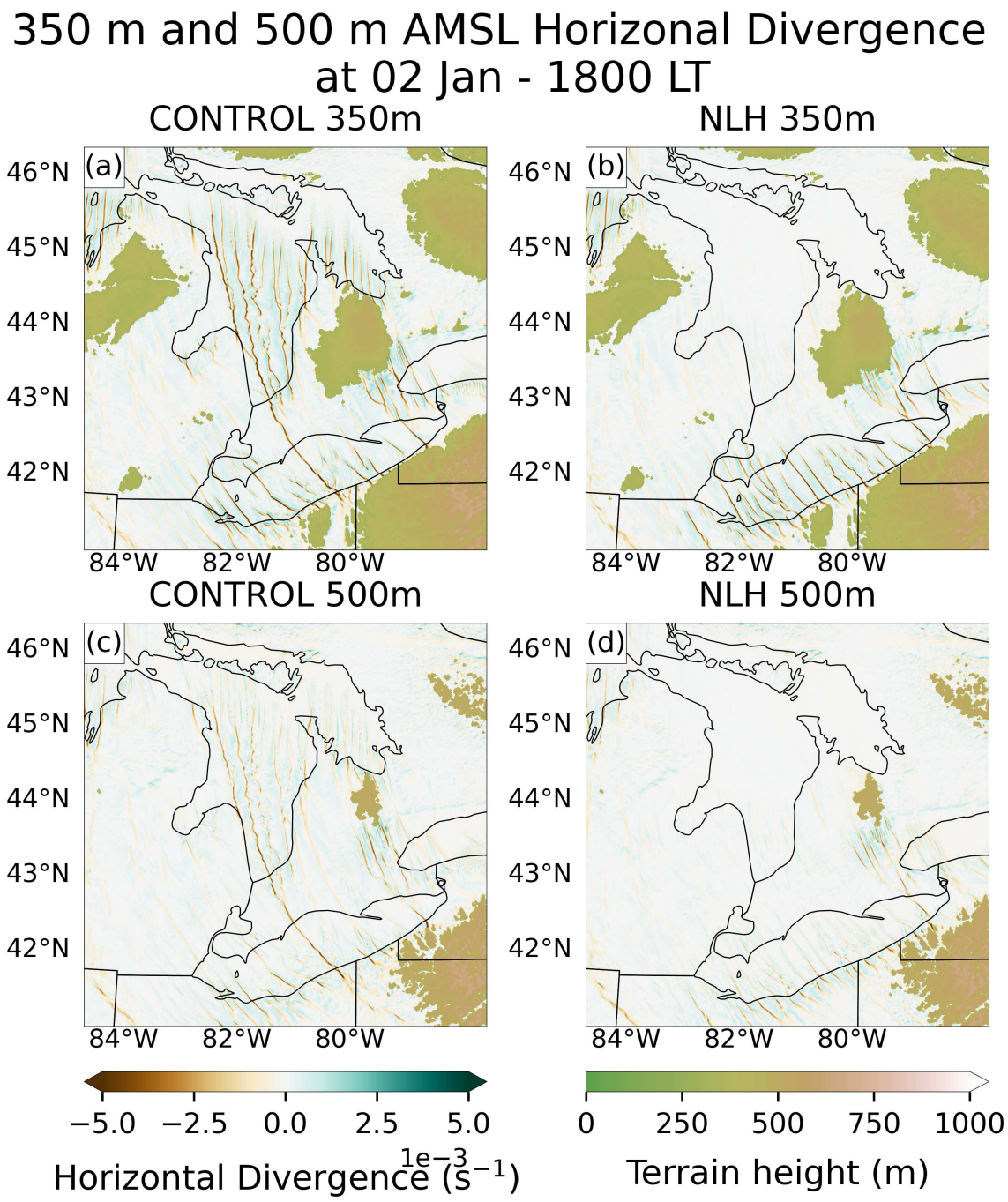

Figure 2.9: Simulated horizontal divergence at 350 m (a,b) and 500 m (b,c) Above Mean Sea Level at 1800 LT on 2 January. A band of convergence originating as one of several bands over Lake Huron persists over the Ontario Peninsula before reintensifying over Lake Erie. Convergence bands also develop over snow-free ground on the Ontario Peninsula before moving over Northeast Lake Erie. Water bodies are outlined in black, while terrain above the respective panel's level is shaded in green and brown.

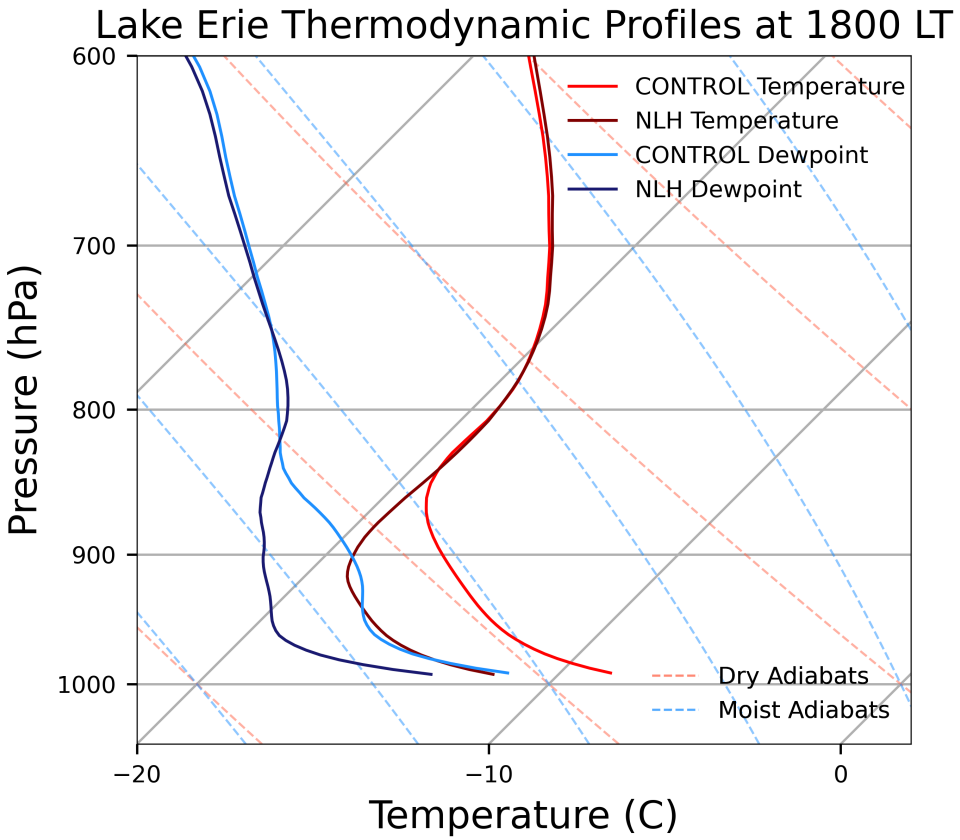

Figure 2.10: Horizontally-averaged (over all grid points over Lake Erie with a water patch fraction of 1) thermodynamic profiles at 1800 LT over Lake Erie in the CONTROL and NLH simulations. CONTROL and NLH simulation temperatures are shown in red and dark red, respectively, while CONTROL and NLH simulation dewpoint temperatures are shown in green and dark green, respectively. Low-level temperatures and dewpoint temperatures are both lower in the NLH simulation relative to the CONTROL simulation, indicating that the presence of Lake Huron warms and moistens air before it reaches Lake Erie. The lower temperature inversion height in the NLH simulation vs the CONTROL simulation also indicates that the presence of Lake Huron, and its associated lake-effect convection, raises the height of the boundary layer over Lake Erie.

lowers pressure and increases surface convergence and the strength of near-surface lifting beneath the band (Figure 2.11b). Unlike Lake Erie, Lake Huron's North-South fetch is over 300 km, providing adequate fetch for the band to fully mature, reaching a 700 m AMSL vertical velocity of $\sim 2\ \mathrm{m\ s^{-1}}$ approximately 85 km south of the shore of Manitoulin Island. 700 m AMSL vertical velocities within the band vary between $\sim 1-2\ \mathrm{m\ s^{-1}}$ until the band enters the narrower southern portion of Lake Huron, where it intensifies reaching 700 m AMSL vertical velocities of $\sim 3\ \mathrm{m\ s^{-1}}$ just northwest of the Ontario Peninsula (Figure 2.8a).

As the band moves inland over the Ontario Peninsula (which is labeled 1 in Figure 2.4b), vertical velocities rapidly decrease from $\sim 3\ \mathrm{m\ s^{-1}}$ to $\sim 1\ \mathrm{m\ s^{-1}}$ (the exact strength of the residual band over the Ontario Peninsula depends on its location, as discussed below) (Figures 2.8a, 2.11c). However, the secondary circulation associated with the band persists over the Peninsula, although it weakens in strength (Figure 2.9a, 2.11c,d). Latent heat release of over $10\ \mathrm{K\ hr^{-1}}$ continues while the residual circulation is over the Ontario Peninsula (Figure 2.11d), which may help it maintain its strength in the absence of large surface sensible heat fluxes. As this residual circulation passes back over the warm water of Lake Erie, the surface convergence and lifting helps to "kickstart" convection once again over the lake in the CONTROL simulation. This new convection and its associated latent heat release re-invigorates the secondary circulation (Figure 2.11e,f). As a result, by the time the air parcels in the main L2L band have traveled ~ 30 km from the lakeshore, the band once more has updraft speeds of $\sim 3\ \mathrm{m\ s^{-1}}$, which it maintains until it moves inland over the Allegheny Plateau in northeast OH (Figure 2.8a).

In addition to the main L2L band, multiple weaker auxiliary lake-effect bands are present over Lake Erie in the CONTROL simulation (Figure 9a,c). While less intense than the main band, they do produce snow, as is seen in Figure 2.12a. In the NLH simulation, there are more of these auxiliary bands compared to the CONTROL simulation (Figure 2.6c,d), but these auxiliary bands have 700 m AMSL vertical velocities which are $\sim 10\%$ lower than those in the CONTROL simulation (Figure 2.8).

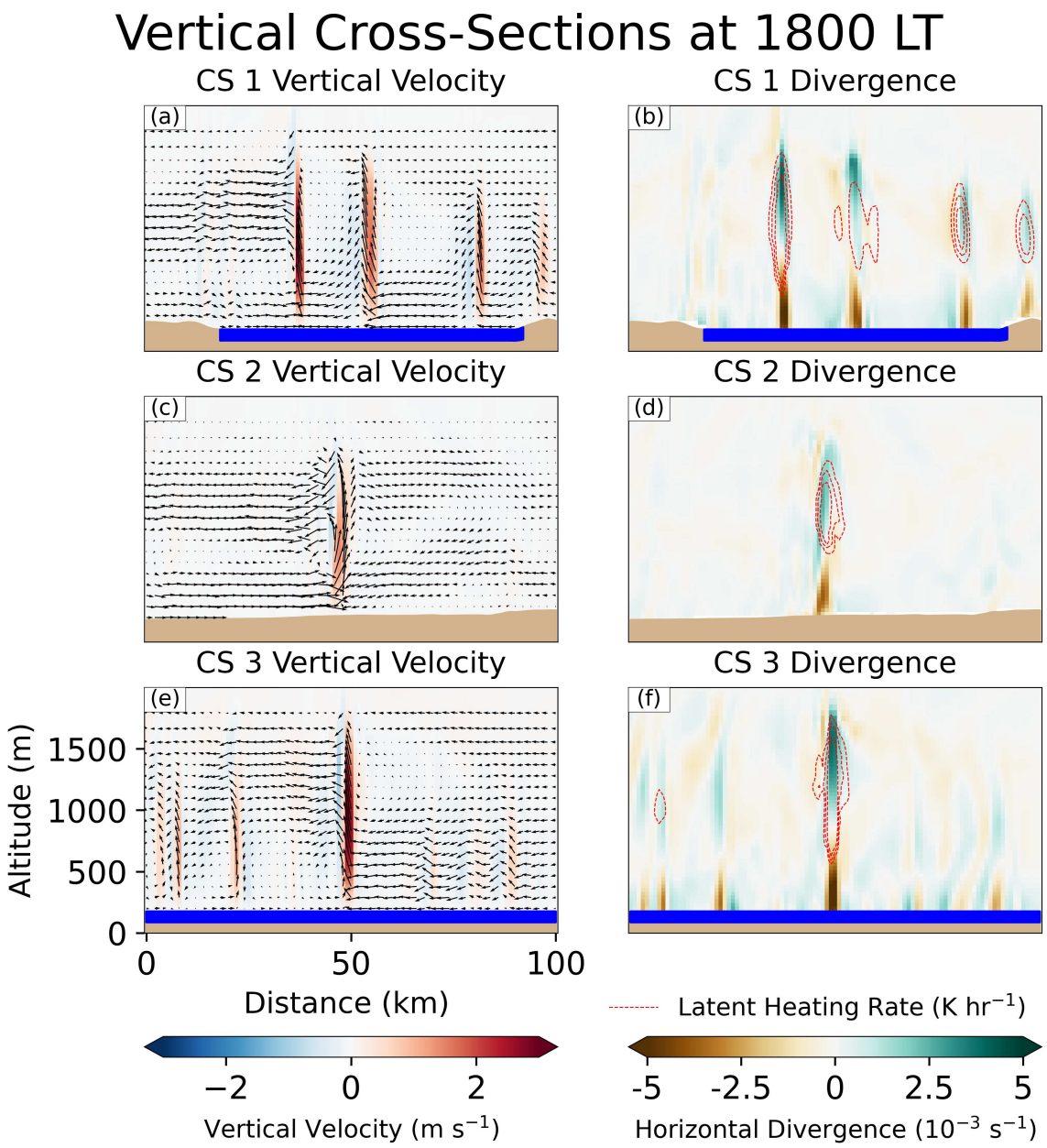

Figure 2.11: Vertical cross-sections oriented southwest to northeast through the main L2L band in the CONTROL simulation, corresponding to those shown in Figure 2.8. Vertical velocity is shown in the left column and horizontal divergence in the right column. In-plane winds are shown on the left, highlighting the presence of secondary circulations within the bands. Contours of latent heating, shown at 2, 5, and 10 K hr^{-1} are shown in red dashed contours on the right, indicating the warming effect of latent heating within the bands.

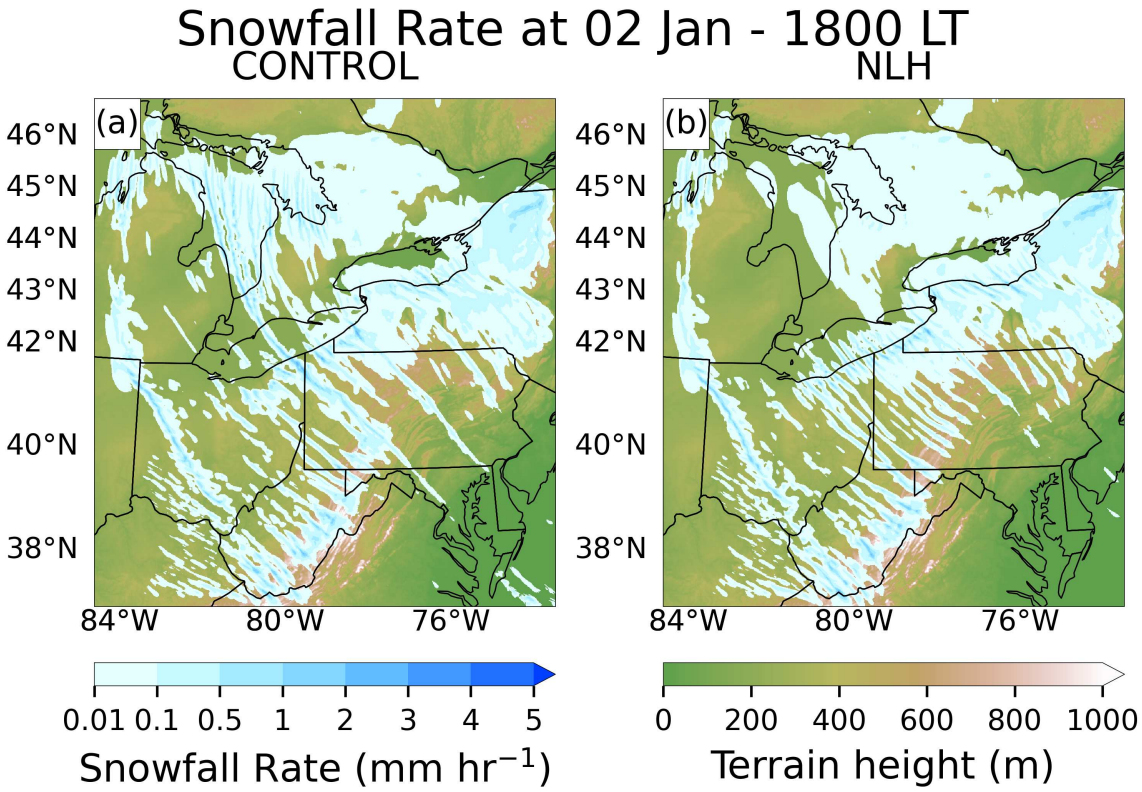

Figure 2.12: Simulated instantaneous snowfall rates at 1800 LT on 2 January. High snowfall rates in northeast OH associated with the Lake Huron - Lake Erie band is seen in CONTROL, but not NLH. A moderate snowband in extreme northeast Lake Erie is seen in both CONTROL and NLH.

The reason for the different behavior of the auxiliary bands between the two simulations is still somewhat unclear. I attempted to use a momentum-budget analysis to identify processes responsible for enhancement and suppression of individual convective bands. Vertical accelerations were calculated following Eq. 1 in Marinescu et al. (2021), using a 40 km horizontal triangular convolution to generate a reference state. However, this is significantly different from the way RAMS calculates vertical velocity, which uses implicit time differencing. As a result, our calculations of acceleration had an unacceptably large residual and were not used for this analysis.

In the NLH simulation, the air over Lake Erie is unmodified by Lake Huron, resulting in colder and drier near-surface air relative to the CONTROL simulation (Figure 2.10). This results in greater sensible heat flux from the lake surface in the NLH simulation compared with the CONTROL simulation (Figure 2.13), and a strongly superadiabatic near-surface layer which encourages weak lifting. Weak updrafts and secondary circulations develop quickly over Lake Erie, but as discussed above, are unable to attain the same strength as the main L2L band before moving ashore (Figure 2.11). In the CONTROL simulation, by contrast, the air over Lake Erie has been modified by Lake Huron, and thus is relatively warmer and moister near the surface relative to the NLH simulation. This results in reduced sensible heat flux from Lake Erie, and a more weakly superadiabatic surface layer which is not quite as favorable for the development of weak convection (Figures 2.13, 2.10). This means that the auxiliary bands over Lake Erie which are dynamically unconnected to an upstream band take longer to develop in the CONTROL simulation compared with those in the NLH simulation.

As discussed above, the boundary layer height is ~ 700 m higher over Lake Erie in the CONTROL simulation relative to the NLH simulation (Figure 2.10. This allows auxiliary bands in the CONTROL simulation to grow stronger (with greater 700 m AMSL vertical velocities) than their NLH counterparts, even though they form later (Figure 2.8). These stronger bands in the CONTROL simulation have a stronger secondary circulation than the bands in the NLH simulation, resulting in greater lifting and convergence within the band, and stronger divergence and sinking outside the band. This sinking outside the band acts to suppress convection nearby. In the NLH

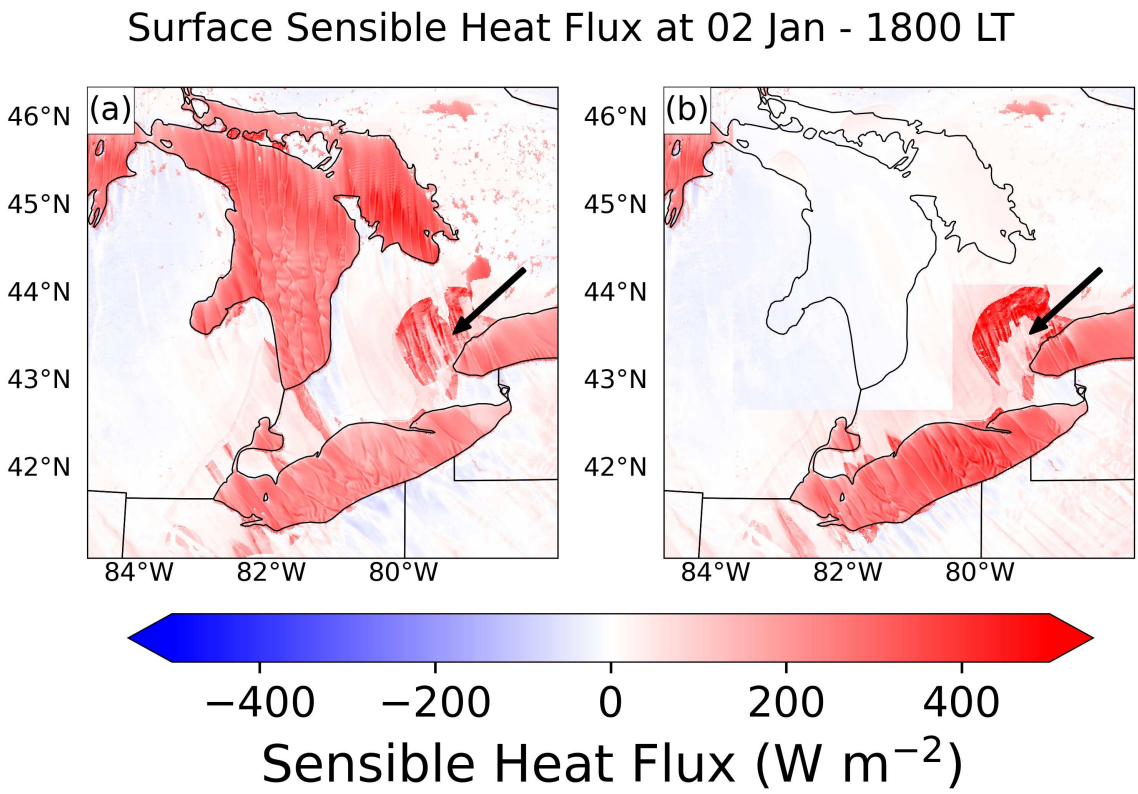

Figure 2.13: Simulated sensible heat fluxes at 1800 LT on 2 January. Greater sensible heat fluxes over Lake Erie are seen in NLH compared to CONTROL. An area of high sensible heat flux is seen in both simulations over snow-free ground west of Lake Ontario, indicated by an arrow. "Blocks" of sensible heat flux are seen in the NLH simulation as a result of the alterations to snow cover and soil temperature described in the "Experiment Design" section.

simulation with weaker bands, the compensating subsidence outside the bands is likewise weaker, meaning that the area around a band in which convection is suppressed is narrower. This allows multiple weaker bands to be present close together in the NLH simulation, while in the CONTROL simulation the few strong auxiliary bands act to completely suppress activity around them.

Interestingly, the 700 m AMSL vertical velocities over Lake Erie are $\sim 10\%$ greater within the auxiliary bands in the CONTROL case compared to those in the NLH case (Figure 2.8), even though sensible heat fluxes over Lake Erie are $\sim 32\%$ lower in CONTROL than NLH (Figure 2.13). In CONTROL, the average sensible heat flux over Lake Erie is $\sim 205\ \mathrm{Wm}^{-2}$, compared to $\sim 272\ \mathrm{Wm}^{-2}$ in NLH. This agrees with the findings of Sousounis and Mann (2000), who concluded that the presence of upstream lakes reduces sensible heat fluxes over Lake Erie through modification of the overlying air, but enhances vertical velocities and snowfall.

Readers noticing the smaller axis of heavy snowfall downwind of the extreme northeast portion of Lake Erie (Region D in Figure 2.5), which is present in both the CONTROL and NLH simulations, might question whether Lake Huron's presence is necessary to produce heavy snowfall downwind of Lake Erie. However, the processes leading to snowfall in this part of the domain are present in both simulations and are significantly different than those driving the main L2L band which produces heavy snowfall in Region B. Looking more closely at the patterns of 700 m AMSL vertical velocity and 500 m AMSL divergence (Figures 2.8c,d and 2.9c-d), one can see that this band doesn't originate over Lake Erie, but actually starts over the Ontario Peninsula. As Figure 2.9 shows, convergence bands form just northwest of Lake Ontario in both simulations. Here, there is an area of snow-free land which is surrounded by snow-covered land (I should note that this area of snow-free land is a result of initialization with ERA5 snow cover, and was not present during the actual lake-effect event of 1-6 January 2010. Nevertheless, the model physics with regard to this area appear realistic, and so will be analyzed in this study). Sensible heat fluxes are much larger over this area of bare soil than the surrounding snow-covered land (Figure 2.13). There are three main reasons for this. First, the relatively dark ground absorbs more sunlight than the snow, with its high albedo, does. Second, snow insulates the soil, thereby inhibiting fluxes of heat between the

surface and the atmosphere. Third, snow can act to reduce surface roughness, by burying rocks and small plants. This reduced roughness inhibits mixing of near-surface air, such that less air comes in contact with the snow surface. Taken together, these three factors dramatically reduce surface sensible heat flux over snow-covered land relative to snow-free land. The large sensible heat fluxes over the snow-free land destabilize the boundary layer, leading to the development of convective bands.

The convective bands over the snow-free area are stronger in the CONTROL simulation than the NLH simulation, which is likely due to the influence of Georgian Bay in the CONTROL simulation and its absence in the NLH simulation. Looking at Figures 2.8 and 2.9c-d, weak but clear residual bands are visible stretching from Georgian Bay to just northwest of Lake Ontario. It is likely that, similar to L2L bands, these residual bands help to "kickstart" convection over this area of snow-free land. As with the lake-effect convection over Lake Erie, the modification of cold Continental Arctic air by Georgian Bay also raises the height of the boundary layer, allowing bands which develop over this area to grow in height and strength compared to the NLH simulation.

Like lake-effect convection, these bands are reliant on strong surface sensible heat fluxes from the surface to the cold overlying atmosphere which acts to destabilize the boundary layer. In the case of lake-effect convection, once air moves onshore, surface sensible heating quickly decreases and the bands rapidly lose strength (although the secondary circulations do not disappear, as was shown above). In the case of these convective bands over the Ontario Peninsula, their source of strong sensible heating is the area of snow-free land. As shown in Figure 2.13, this area does not extend all the way to Lake Erie. As bands move southeast from the snow-free land to the snow-covered land, the strength of the sensible heating quickly decreases and the bands rapidly lose strength. However, as with lake-effect convection, the secondary circulations persist even after the source of sensible heating is gone. In this case, as the secondary circulations move back over Lake Erie, they reintensify just as with the Huron-Erie band, and subsequently lead to heavy snowfall in Region D (Figures 2.6, 2.9, 2.11, 2.5). This process occurs similarly in the CONTROL and NLH simulations, although, in the NLH simulation, the upstream secondary circulation which

reintensifies over Lake Erie switches back and forth between the band over the snow-free area and a band which originates over western Lake Ontario.

Snow cover also affects the intensity of the main L2L band over Lake Erie in the CONTROL simulation. Looking at Figure 2.13, a stripe of greater sensible heat flux is visible between Lake Huron and Lake Erie. This is an "isthmus" of no snow cover surrounded on the left and right by areas of snow cover. Much as with the area of bare ground northwest of Lake Ontario, this area promotes rising motion within the stripe. As a result, when the "residual" portion of the L2L band (the portion over the Ontario Peninsula between Lake Huron and Lake Erie) is located directly over this snow-free stripe, it is stronger than when it is slightly west or east of this stripe. Compare the vertical velocity of the main L2L band over the Ontario Peninsula in the left panel of Figure 2.8 vs the panels of Figure 2.14, where the residual band weakens as it shifts east away from the snow-free stripe. A similar stripe of no snow cover is present in the NLH simulation as well, and is responsible for the development of a convective band just upwind of Lake Erie near (42.5N, 82W).

2.5 Discussion

Our findings indicate that Lake Erie, on its own, cannot produce very intense snow bands when the prevailing winds are northwesterly. In this environment, the fetch over Lake Erie is too short to support the development of intense lake-effect convection. Instead, intense bands which occur over Lake Erie are dependent on the development of upstream secondary circulations. In the CONTROL simulation, many weak convective bands develop over northern Lake Huron, and move southeastward over the lake. One of these convective bands persists over the Ontario Peninsula and moves over Lake Erie, where it quickly reintensifies into the strongest convective band in the domain (Figures 2.8a, 2.9a). In the NLH simulation, by contrast, Lake Huron is absent. Therefore, no upstream bands develop in this region which can subsequently reintensify over Lake Erie (Figures 2.8b, 2.9b). As a result, the "main L2L band" is entirely absent in the NLH simulation. Since this main band has the greatest snowfall rates of any lake-effect band in the domain (Figure 2.12a), the presence of this band leads to an intense snowfall maximum in Region

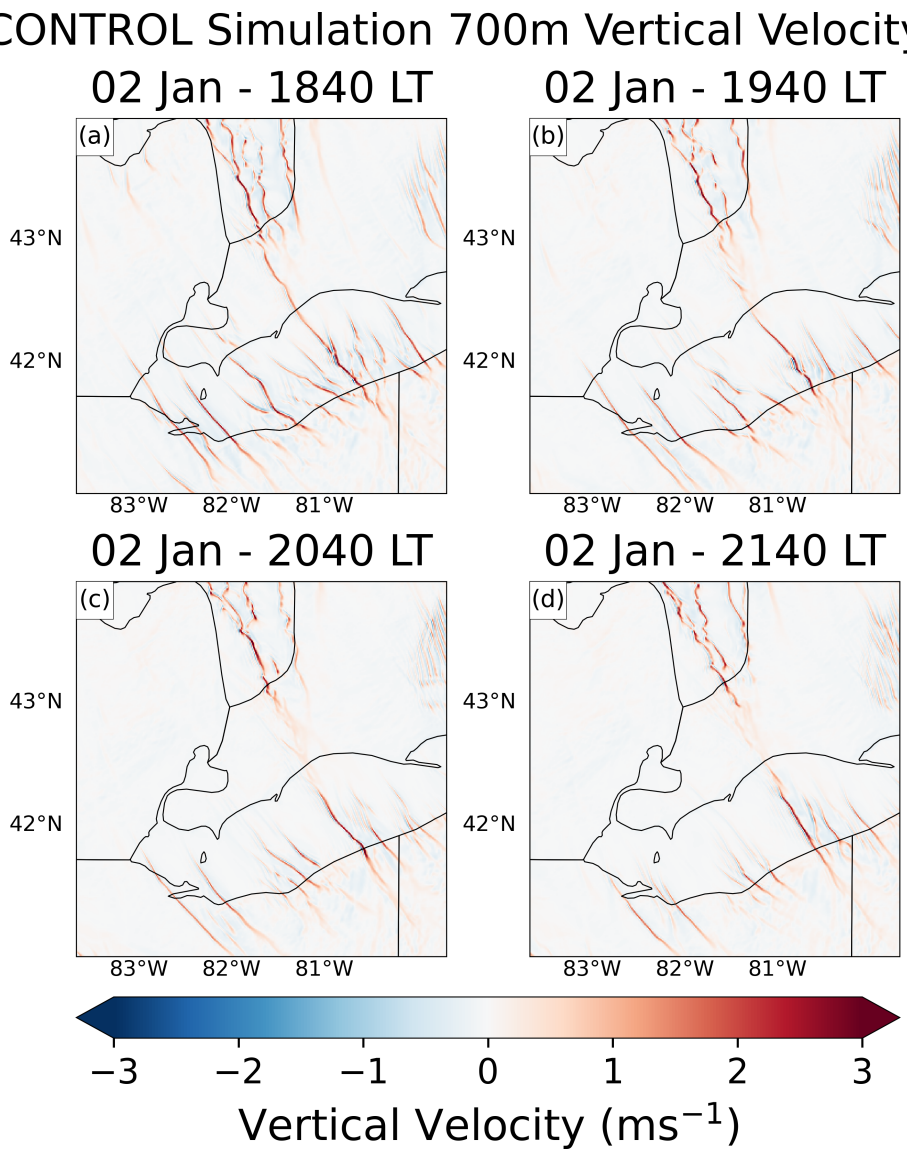

Figure 2.14: 4-Panel plot showing the evolution of vertical velocity at 700 m Above Mean Sea Level over 3 hours from 1840 LT to 2140 LT on 2 January. As the lake-effect band over Lake Huron shifts east from (a) to (b), the connected L2L band over Lake Erie subsequently shifts east as well (c,d).

B near the PA/OH border in the CONTROL simulation which is not present in the NLH simulation (Figure 2.5d-f).

The dependency of the main L2L band on convection over Lake Huron can be seen in the Figure 2.14. The main band of convection over Lake Erie actually "follows" the band from Lake Huron. As the band over Lake Huron position east or west, the main L2L band over Lake Erie subsequently shifts its position over the course of a few hours.

Should the physical processes driving the initial band formation and subsequent downwind band linkage and development shown in this study prove robust, this pattern of movement may present a potential forecasting opportunity; since movement of the Lake Huron band will be followed by movement of the Lake Erie band, forecasters looking to predict where heavy snow will occur downwind of Lake Erie in the next few hours could watch the motion of the convective band near the southern end of Lake Huron. If that band shifts east, the convective band over Lake Erie would, as described above, subsequently shift east after some amount of time. Of course, whether this behavior holds for most L2L events over Lake Erie is unknown. Future studies examining the establishment of L2L band connections and time lags between upwind and downwind band movements should be conducted using additional case study simulations as well as satellite and radar observations to necessary to verify existence of this behavior in L2L bands.

While I did not run ensemble simulations to test whether this L2L band would have formed under slightly different initial conditions, the underlying physics behind the L2L connection are unlikely to change significantly. The number of cases in which L2L connections between Lake Huron and Lake Erie have been observed indicates that these events occur under a range of environmental conditions (Rodriguez et al., 2007; Laird et al., 2017). The initial conditions would likely impact exactly where lake-effect bands form over Lake Huron, and that in turn may impact exactly where the main L2L band re-intensifies over and makes landfall downwind of Lake Erie, but the fundamental processes linking the bands are expected to be similar to those described above.

While this study focused on lake-to-lake connections between Lake Huron and Lake Erie, these results are potentially applicable to the other Great Lakes, particularly Lake Superior-Lake Michigan, Lake Superior-Lake Huron, Lake Michigan-Lake Huron, and Lake Huron-Lake Ontario, as well as sea-to-lake, lake-to-sea, and sea-to-sea snowfall events which occur in the North Sea, Baltic Sea, and Gulf of Finland. These events have similar surface and dynamic characteristics to lake-to-lake events, so the above findings on the impacts of lake-to-lake connections may apply around the world.

The impact of snow-free land on lake-effect convection, while not the main focus of this study, presents an interesting and novel phenomenon. To recap the processes described above, surface sensible heat fluxes are much larger over snow-free land than over surrounding snow-covered land, due to the effect of snow cover on albedo, thermal insulation, and roughness length. The high sensible heat flux over snow-free land heats the near-surface air, destabilizing the boundary layer and allowing weak convection to form. As seen with the lake-effect band over extreme northeast lake Erie in Figure 2.8c,d in both simulations, circulations associated with this weak convection can act to "kickstart" *lake-effect convection* much like a lake-to-lake connection.

Since the snow-free land provides a strong sensible heat source and initiates convective bands which behave similarly to those which form due to lake-effect convection, I propose that this convection initiation which occurs when cold Arctic air blows over areas of warm snow-free land be termed the "brown lake-effect", in the same vein as the "brown ocean effect", which occurs when tropical cyclones maintain strength or intensify after landfall as strong surface sensible/latent heating over land allows convection to persist inland.

A simple schematic comparing sensible heat fluxes and near-surface air temperatures in true lake-effect and the "brown lake-effect" is shown in Figure 2.15. In both cases, an area of stronger sensible heat fluxes relative to its surroundings heats the near-surface air and destabilizes the lower atmosphere and initiates weak convection. Because of the role of this weak convection in "kick-starting" lake-effect convection over downwind narrow lakes, this may present an additional forecasting opportunity. Areas of snow-free land (identifiable via satellite imagery, surface snow depth

monitoring, and ground-level cameras) upwind of narrow lakes may indicate the potential for heavier snowfall in areas on the side of the lake downwind of the snow-free land compared to areas on the same side of the lake but downwind of snow-covered land. I should be careful not to be too bold with these predictions; this is a phenomenon observed in one mesoscale model simulation using one land surface scheme, one microphysical parameterization, and one dynamical core. Whether this occurs in other models, let alone the real world, is unknown. The area of snow-free land west of Lake Ontario present in the CONTROL and NLH simulations arose as a result of ERA5 initialization, and was not present during the real event, meaning that no impacts from snow-free land on lake-effect convection were observed. That said, the model processes over the snow-free land appeared realistic, and could reasonably be expected to occur in nature were such a snow-free area to exist. Additional research is necessary to confirm or refute the existence of this phenomenon.

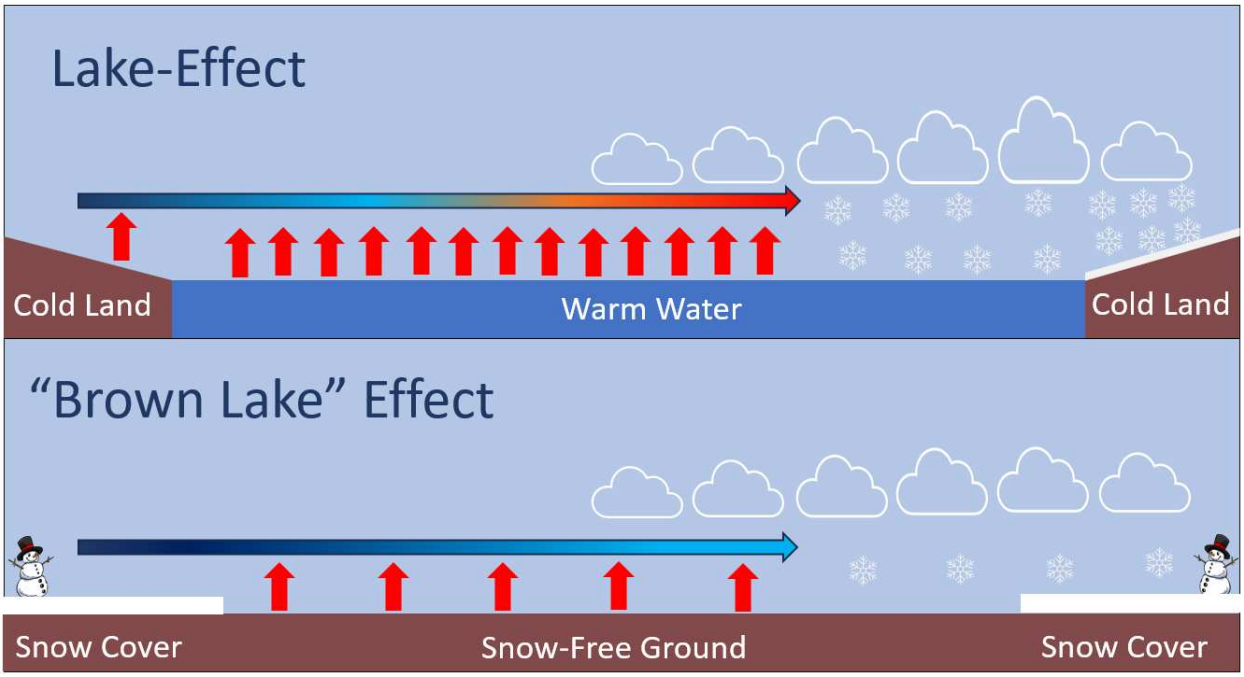

Figure 2.15: A schematic of traditional lake-effect processes (top) and "brown lake" effect processes (bottom). Red upward arrows indicate sensible heating. The color of the horizontal arrow indicates the temperature of near-surface air flowing from left to right. Dark blue indicates cold air, light blue less cold, orange warm, and red very warm. While traditional lake-effect snow occurs due to heating by the warm lake in contrast to the surrounding colder ground, "brown lake" effect occurs due to heating by snow-free ground in contrast to the surrounding snow-covered ground.

2.6 Conclusion

In this study, a lake-effect snow event which occurred between 1-3 January 2010 was simulated with the RAMS model, both with a realistic land surface (CONTROL) and a surface in which Lake Huron was replaced with mixed forest (NLH). The spatial pattern and intensity of snowfall in the CONTROL simulation was similar to that of SNODAS.

I have shown in our numerical simulations that the presence of an upwind lake significantly enhances lake-effect snowfall over a downwind lake compared to similar lake-effect events in which an upwind lake is not present. Lake-effect convection over the upwind lake leads to the formation of near-surface convergence bands, which persist overland as they move toward the downwind lake. These convergence bands "kickstart" convection over the downwind lake, building intense L2L bands with strong vertical velocities and secondary circulations and large snowfall rates. In the absence of an upwind lake and these pre-existing convergence bands, convection over the downwind lake must develop from scratch. In the case of a narrow lake with short fetch, as Lake Erie is under northwesterly flow, these convective bands do not have sufficient time to intensify and mature before they move inland, leading to weak convection with little snowfall. In our simulations, the impact of the pre-existing convergence bands was seen in the development of the strong L2L snow band over Lake Erie near the PA-OH border in the CONTROL simulation and its absence in the NLH simulation. The alignment and subsequent movements of these L2L bands may present a short-term forecasting opportunity for predicting where heavy snow will occur in the next few hours.

Additionally, I demonstrated that convective bands also originate over areas of bare soil surrounded by areas of snow-covered land. These “brown lakes” have much greater sensible heat flux than their snow-covered surroundings, and act to initiate convection like unfrozen lakes. As with an lake-effect bands initiated over upwind lake, the convergence bands associated with this convection over bare soil persist as they move downwind over snow-covered land, thereby accelerating the subsequent development of convection over the downwind lake. In our simulations, convective bands initiated over the snow-free areas of the Ontario Peninsula and moved down-

wind over northeast Lake Erie, where they intensified and produced heavy snow in western NY. Like L2L bands, the secondary circulations associated with these "brown lake-effect" bands enhance true lake-effect convection over narrow lakes and enhance snowfall. Knowledge of these "brown lake-effect" processes associated with bare soil may present a forecasting opportunity during early-season lake-effect snow events, or lake-effect snow events in regions without consistent winter snow cover.

Chapter 3

Impacts of Forest Breezes, Cold Pools, and Sea Breezes on Coastal Convective Storms

3.1 Introduction

The location and timing of convective storms, as well as their impacts and hazards, are highly dependent on the surrounding patterns of temperature, wind, and humidity, referred to in this chapter as the "convective environment" (Weisman and Klemp, 1984; Derbyshire et al., 2004; Rapp et al., 2011) This convective environment is affected by the development of the PBL throughout the day. The development of the PBL is itself affected by land surface properties, as different land surfaces absorb different amounts of solar radiation, impart different latent and sensible heat fluxes on the overlying atmosphere, and lead to changes in atmospheric stability, moisture, and wind speed and direction (Anthes, 1984; Chen and Avissar, 1994; Segal et al., 1995; Drager et al., 2022). For example, a desert with a smooth, highly reflective surface and no transpiring vegetation will likely have lower energy fluxes to the atmosphere and a larger Bowen ratio than a lush tropical jungle with tall, dark-leaved trees and large amounts of transpiration.

Several studies have examined the relationship between land surface properties and the occurrence of cloud formation and precipitation. 1D numerical modeling experiments over uniform terrain have found that lower Bowen ratios result in more favorable conditions for deep convection over both bare soil and vegetated surfaces, while 3D numerical modeling experiments have reported an increase in precipitation over more moist bare soils, but a non-monotonic relationship between surface Bowen ratios and precipitation over vegetated surfaces (Segal et al., 1995; Drager et al., 2022). A satellite study over Costa Rica and Nicaragua noted that cloud cover was lower over deforested areas than over adjacent forests, while a similar study examining rainfall and land surface temperature in the Brazilian Amazon found that deforested areas experienced in-

creased surface temperatures and reduced precipitation compared to adjacent areas of intact forest (Nair et al., 2003; Maeda et al., 2021). However, a study analyzing lightning strikes over Northern Australia reported that grasslands had a higher strike density than adjacent woodlands (Kilinc and Beringer, 2007). While all three studies attributed these differences in cloud cover to higher sensible heat flux over nonforested areas relative to adjacent forests, they reported different effects of this change in sensible heat flux on cloud cover and convective storm activity.

It is important to note that, in landscapes with heterogeneous land cover, the development of convection is strongly affected by the gradients in land surface properties between "patches" of different land cover types. For example, a storm which forms over a square of pasture in a checkerboard landscape of pasture and broadleaf forest will behave differently than a storm which forms over a uniform pasture landscape. The reason for this is that gradients in land cover produce mesoscale circulations at the boundary of different land cover types. These mesoscale circulations arise as different land cover properties lead to differences in heat, vapor, and momentum fluxes to the atmosphere, which in turn leads to gradients in the convective environment (Anthes, 1984; Giorgi and Avissar, 1997; Emori, 1998). These gradients then induce baroclinic circulations which can help initiate convection in certain areas and suppress it in others.

The existence of gradients in land surface properties, and their effects on convective storms and precipitation, have been seen in numerous observational and modeling studies. Several observational studies have examined the occurrence of clouds over areas of sharp contrasts in vegetation and soil moisture and found that shallow convective clouds were favored to occur over hotter, drier surfaces adjacent to cooler, more humid areas (Rabin et al., 1990; Esau and Lyons, 2002; Chagnon et al., 2004; Sato et al., 2007; Taylor et al., 2012). By contrast, Brown and Arnold (1998) found that the initial development of convective clouds during the day was more likely on the moist side of vegetation and soil type boundaries, but that deep convection was equally likely to develop on either side of the boundaries. While not directly examining clouds, Phillips et al. (2022) analyzed data from the Great Plains Irrigation Experiment (GRAINEX) field campaign in Nebraska to determine that the presence of irrigated areas on elevated terrain weakened diurnally-driven upslope

winds, which the authors speculated may likewise affect the development of clouds and precipitation.

In addition to observations, many modeling experiments have analyzed the relationship between vegetation and soil moisture gradients and convective cloud development. Case study simulations of the development of deep convection over Oklahoma have found that both shallow and deep convection developed first over drier soil areas relative to their surroundings (Fast et al., 2019; Chen et al., 2020). Other modeling experiments which varied land use patterns in China, Oman, and Israel have found that gradients in latent and sensible heating along soil moisture and vegetation boundaries induce mesoscale circulations which favor cloud development and precipitation over the hotter surface (Kawase et al., 2008; Branch and Wulfmeyer, 2019).

Finally, many idealized modeling studies examining the relationship between soil moisture and convection have been performed at various scales and with various patterns of surface heterogeneity. Large Eddy Simulations (LES) with checkerboard patterns of land surface properties found that mesoscale circulations developed on the boundaries of the wet and dry patches, leading to inflow, rising motion, and convection over the dry patches, and suppression of convection and precipitation over the wet patches (Wang et al., 2011; Rieck et al., 2014; Harvey et al., 2022; Lee et al., 2019; Rieck et al., 2015). Other idealized simulations varied land surface properties in a stripe pattern (Avissar and Liu, 1996; Lee and Kimura, 2001; Wang et al., 2011; Lynn et al., 1998; Chen and Avissar, 1994; Hong et al., 1995; Cioni and Hohenegger, 2018; Emori, 1998; Garcia-Carreras et al., 2011; Kang and Bryan, 2011; Rieck et al., 2015) . All results from these studies demonstrated that circulations between the stripes led to convergence and rising motion over the warm patches, favoring precipitation there.

The size of the land surface patches or stripes greatly affects the locations and strengths of these land surface-induced circulations, and hence the convection they initiate. Too small of a patch may not allow sufficient temperature contrasts to build to drive strong mesoscale circulations, while too large of a patch will confine these circulations to the edges of each patch, preventing them from helping initiate convection in the center of the patch. Chen and Avissar (1994) hypothesized that

there is an "ideal patch size" which allows strong circulations to develop and collide in the center of the patch while conditions are still favorable for further convective storm development. They determined that this "ideal patch size" was equivalent to the local Rossby Radius of Deformation, which was approximately 100 km in their simulations. Lynn et al. (1998) demonstrated this in their 2D simulations, where patches 128 km wide allowed for collision of circulations and intense precipitation, while patches 256 km wide did not produce a collision of circulations before conditions were no longer favorable for convection. However, Rieck et al. (2014) were not able to find a clear monotonic relationship between patch size and the onset time or domain total of precipitation as they experimented with checkerboard patch sizes ranging from 3.2 to 51.2 km across. Additionally, Hong et al. (1995) demonstrated that this "ideal patch size" depends on atmospheric stability; greater static stability decreases the "ideal patch size" by favoring the development of narrower circulations, while low static stability increases the "ideal patch size" by favoring wider circulations.

In addition to the direct effect of mechanical lifting arising from these land surface-induced circulations, many authors have noted that, because these circulations are divergent near the surface of wet patches, and convergent and rising over dry patches, they act both to transport water vapor from the surface of wet patches to dry patches, and to lift that water vapor into upper levels of the boundary layer over dry patches (Cioni and Hohenegger, 2018; Rieck et al., 2014; Emori, 1998; Lee et al., 2019; Harvey et al., 2022; Kawase et al., 2008; Chen and Avissar, 1994; Avissar and Liu, 1996; Hong et al., 1995). This increase in upper-PBL water vapor acts to lower the Lifted Condensation Level (LCL) and the Level of Free Convection (LFC) over the dry patch, at the same time as the warm temperatures and rising motions raise the height of the PBL. Together, these factors combine to encourage the development of deep convection over the dry patch. At the same time, divergence aloft over the dry patch and convergence and sinking aloft over the wet patch act to bring dry air from higher in the atmosphere down closer to the surface of the wet patch, while simultaneously stabilizing the atmosphere through adiabatic warming of the subsiding air. This acts to suppress convective development over the wet patch.

Despite ample evidence from modeling and observations demonstrating that heterogeneous land surface properties induce mesoscale circulations which affect convection, many outstanding questions remain. In particular, none of the idealized modeling studies described above have simulated a coastal environment. The interaction of sea breeze circulations with land surface-induced circulations has not been well-explored, and the combined effects of these interacting circulations on convection initiation is unclear. Furthermore, although Rieck et al. (2015) explored the role of cold pools in increasing the propagation speed of these circulations, they did not demonstrate if or how this affected the collision of the circulations at the center of the dry patch. Finally, the modeling studies described above have compared variations in prescribed surface fluxes, soil moisture, vegetated vs bare soil surfaces, or single parameters of the vegetation (such as LAI in Rieck et al. (2014) and Rieck et al. (2015)), but they have not contrasted multiple vegetation types with different surface roughnesses, albedos, leaf properties, or vegetation fractions.

Therefore, the goal of this study is to examine two outstanding questions related to landscape heterogeneity-induced convection in coastal environments. 1. How does the interaction of the sea breeze with landscape heterogeneity-induced circulations affect the location and impacts of convection? 2. How do cold pools produced by the initial convection associated with these circulations affect the subsequent development of these circulations and future convection?

3.2 Experiment Design

To examine the impact of heterogeneous land surfaces on convection in a coastal environment, I ran six idealized simulations using the Regional Atmospheric Modeling System (RAMS), a non-hydrostatic, cloud-resolving model (Cotton et al., 2003). For this study, RAMS was run with the LEAF-3 land surface parameterization (Walko et al., 2000). Common model settings for all simulations are provided in Table 3.1.

A major motivation for this study was the Experiment of Sea Breeze Convection, Aerosols, Precipitation, and Environment (ESCAPE), a field campaign conducted around Houston, TX in the summer of 2022 alongside the Tracking Aerosol Convection Interactions Experiment (TRACER)

(Kollias et al., 2023; Jensen et al., 2023). The Houston area is a coastal location which also possesses many different land surface types, including the urban core and sprawling suburbs of Houston itself, coniferous forest to the north and east of the city, and agricultural pasture and cropland to the south and west. As such, I designed simulations which presented coastal domains with land surfaces representative of those found around Houston (described in more detail below). All simulations prescribed an ocean area south of a land area with a straight east-west coastline. The ocean extended 150 km north from the southern boundary, and spanned the entire 200 km east-west width of the domain (the ocean is shown by the blue area in Figure 3.1). North of the ocean was a land area extending 250 km in the north-south direction to the northern boundary of the simulation and the entire 200 km east-west domain width. To prevent the complicating effects of topography, all land areas were completely flat with a terrain height at sea level.

A set of six simulations was run with varied land surface types (Figure 3.1). These simulations were initialized with a volumetric soil moisture of 0.19 $m^3 m^{-3}$, representative of the conditions found in the Houston area on 17 June 2022 (Dashtian and Young, 2023). During this time, Houston was experiencing a severe drought, resulting in dry soils in the region. These simulations were also initialized with a horizontally uniform southerly background wind profile which increased logarithmically with height from 2 ms^{-1} at the surface to 8 ms^{-1} at 900 hPa. This wind profile was representative of that observed in the PBL on 17 June 2022, while the constant wind profile above the boundary layer simplified analysis (Keeler et al., 2022). The real wind profile on this day did vary weakly above the PBL, but there was little vertical wind shear present above the PBL which would affect convective organization.

The only differences between the six simulations were the type and spatial distribution of land cover north of the ocean. The first three simulations had uniform land surface types; simulations UP - uniform pasture, simulation UF - uniform coniferous forest, and US - uniform suburbs. (Figure 3.1a-c). I chose these land surface types to represent the landscape found in and around Houston, with different land surface types adjacent to one another and near the coast. Simulations 4-6 employed a striped land surface pattern (Figure 3.1d-f). The leftmost and rightmost 50 km

from the zonal boundaries consisted of one land type, while the center 100 km was another land type. Because of the periodic zonal boundary conditions, this is identical from a modeling perspective to having two 100 km wide stripes adjacent to one another. Simulation PF consisted of a center stripe of coniferous forest surrounded by pasture (Figure 3.1d), simulation SF consisted of a center stripe of coniferous forest surrounded by suburbs (Figure 3.1e), and simulation SP consisted of a center stripe of pasture surrounded by suburbs (Figure 3.1f). Table 3.2 illustrates a few key properties of the three different land surface types.

As stated above, the simulations used periodic boundary conditions in the east-west dimension and made use of radiative boundary conditions in the north-south dimension. The Coriolis force was disabled in this simulation, even though it does significantly affect the development of the sea breeze at this latitude (Fisher, 1960; Yan and Anthes, 1987). This was done for simplicity purposes, as I wanted to focus on the basic interactions of vegetation-induced circulations perpendicular to an idealized sea breeze. This lack of a Coriolis force also allows the vegetation-induced mesoscale circulations to maintain their orientation parallel to the vegetation stripes, thereby simplifying the analysis of their interactions with cold pools.

The initial thermodynamic profile for our simulations was obtained from the 0538 UTC 17 June 2022 sounding launched from the Atmospheric Radiation Measurement (ARM) sounding site at La Porte, TX during the TRACER field campaign (Keeler et al., 2022). This sounding was chosen because 17 June 2022 was a day which featured widespread isolated convection over the Houston area which was well observed by airborne and ground-based measurement platforms during the ESCAPE field campaign (Kollias et al., 2023). To disrupt initial atmospheric homogeneity and encourage more realistic boundary layer behavior, small random perturbations were applied to the potential temperature field at simulation initialization. First, each grid point at the lowest atmospheric model level (15 m above the surface) had its potential temperature perturbed by a randomly chosen value from a normal distribution with a standard deviation of 0.3 K. All perturbations greater than 1 K or less than -1 K were set to 1 K and -1 K, respectively. A Gaussian smoothing was then applied to minimize sharp gradients in potential temperature between adja-

cent horizontal grid points. This Gaussian smoothing had the effect of reducing the magnitude of temperature perturbations at the surface to between approximately -0.5 K and 0.5 K. The magnitude of the temperature perturbation in each column decreased exponentially with height up to 1 km, at which point the perturbations were set to zero, to confine the turbulent motions early in the simulation to near the surface and within the nocturnal boundary layer.

3.3 Results

3.3.1 Uniform Land Surface Simulations

A weak sea breeze develops in all simulations starting at approximately 1000 LT. The sea breeze front moves inland throughout the day, reaching y = +75 km at approximately 1500 LT, though this timing varies slightly over different land cover types (Figure 3.2). This sea breeze front does not present a well-defined convergence zone and is difficult to identify within dynamical fields of meridional velocity or low-level horizontal convergence. However, it is clearly visible as a meridional gradient of low-level water vapor mixing ratio at y $\approx +50$ km in Figure 3.2a-c.

In addition to the sea breeze, horizontal convective rolls (HCRs) developed in all three uniform land surface simulations. These circulations are parallel to the mean northward background wind and have rising and sinking branches, consistent with prior observations of HCRs (Sykes et al., 1988; Weckwerth et al., 1996). These circulations are visible in Figure 3.2 as alternating north-south oriented bands of larger and smaller vapor mixing ratio, and in Figure 3.3 as bands of greater and lower temperature. The greater temperature and larger vapor mixing ratio bands are associated with the buoyant, rising branch of these roll circulations, while the lower temperature and smaller vapor mixing ratio bands are associated with the sinking branch. The difference in vapor mixing ratio occurs as the rising branches of the plumes lift higher vapor mixing ratio air from near the surface into the middle and upper PBL, while the sinking branches transport the relatively drier air of the middle PBL downward to the surface.

Deep convection (defined here as storms with cloud top heights above 6 km AMSL following Lee et al. (2019)) develops along and inland of the sea breeze front in all three uniform land surface

Table 3.1: Settings Used for Idealized Simulations of Coastal Convection.

Model Parameter	Value
Grid	Arakarwa C-Grid Arakawa and Lamb (1977)
Horizontal Grid Spacing (m)	500
Horizontal Domain	802 x 402
Vertical Grid Spacing (m)	Stretched (30-300)
Vertical Levels	105
Timestep (seconds)	1.5
Simulation Duration (hours)	18
Thermodynamic Initialization	0528 UTC 17 June 2022 La Porte, TX Sounding (Keeler et al., 2022)
Zonal Boundary Conditions	Periodic
Meridional Boundary Conditions	Radiative (Klemp and Wilhelmson, 1978)
Upper Boundary Condition	Rigid model top at 23 km
Surface Paramterization	LEAF-3 (Walko et al., 2000)
Soil Levels	8 Levels from -0.5m to -0.09m
Soil Type	Clay Loam
Soil Moisture	0.19 $m^3 m^{-3}$
Water Temperature	300 K
Microphysics Scheme	Two-moment bulk microphysics with 8 hydrometeor species (Saleeby and Cotton, 2004)
Radiation Scheme	Two-stream radiation, with tendencies updated every 10 minutes (Harrington, 1997)
Aerosol Initialization	$\frac{450}{cm^3}$ at surface, decreasing exponentially with height (Saleeby and van den Heever, 2013)
Aerosol-Radiation Direct Effects	On (Saleeby and van den Heever, 2013)
Aerosol Sources and Sinks	Aerosol depletion from nucleation and wet/dry deposition (Saleeby and van den Heever, 2013)
Turbulence Scheme	(Smagorinsky, 1963) with modifications by (Hill, 1974) and (Lilly, 1962)
Coriolis Force	Inactive
Latitude (degrees)	30
Day of Year	17 June

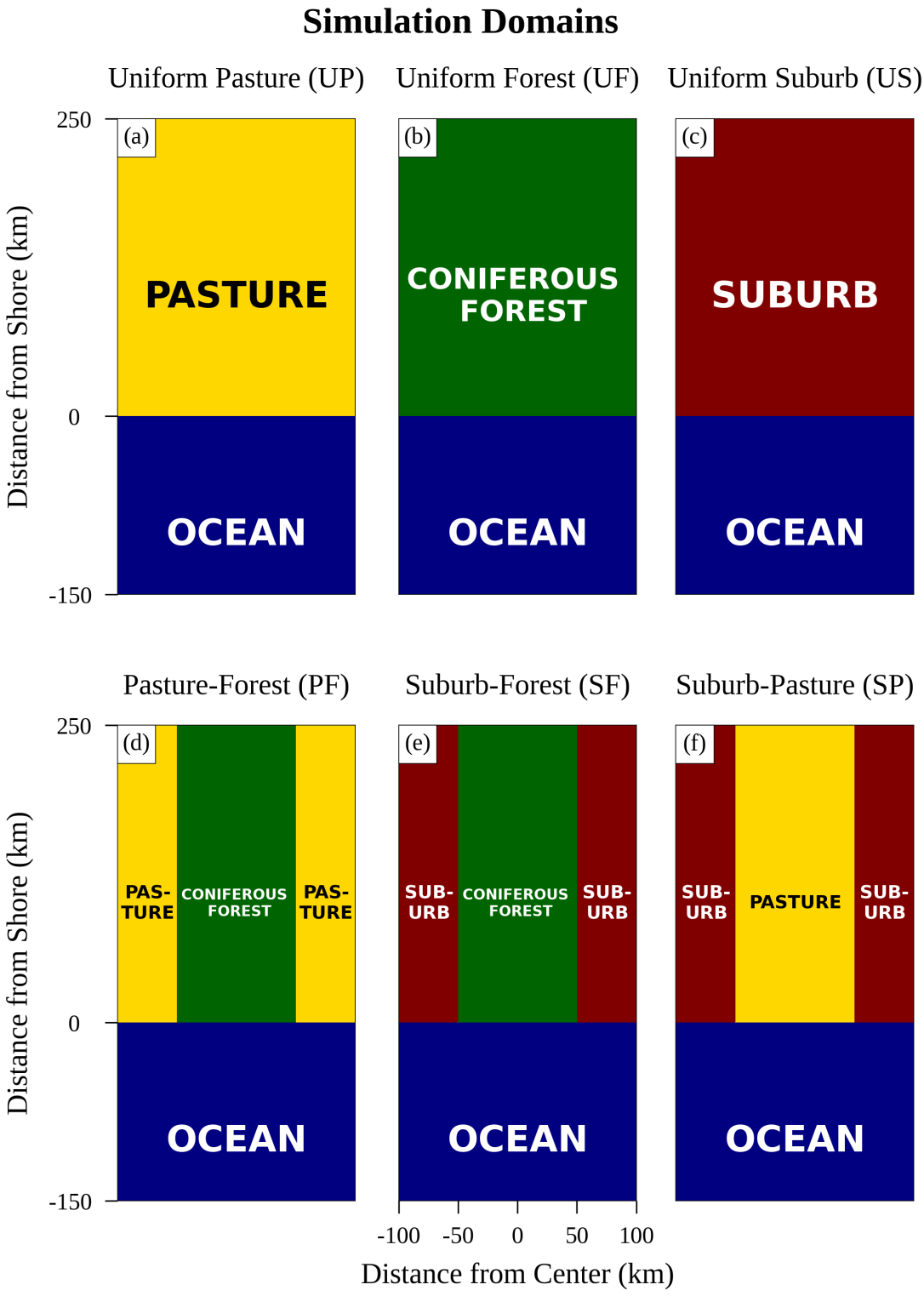

Figure 3.1: Comparison of the six model domains used in the study. Land surface types in each area of the domain are labeled.

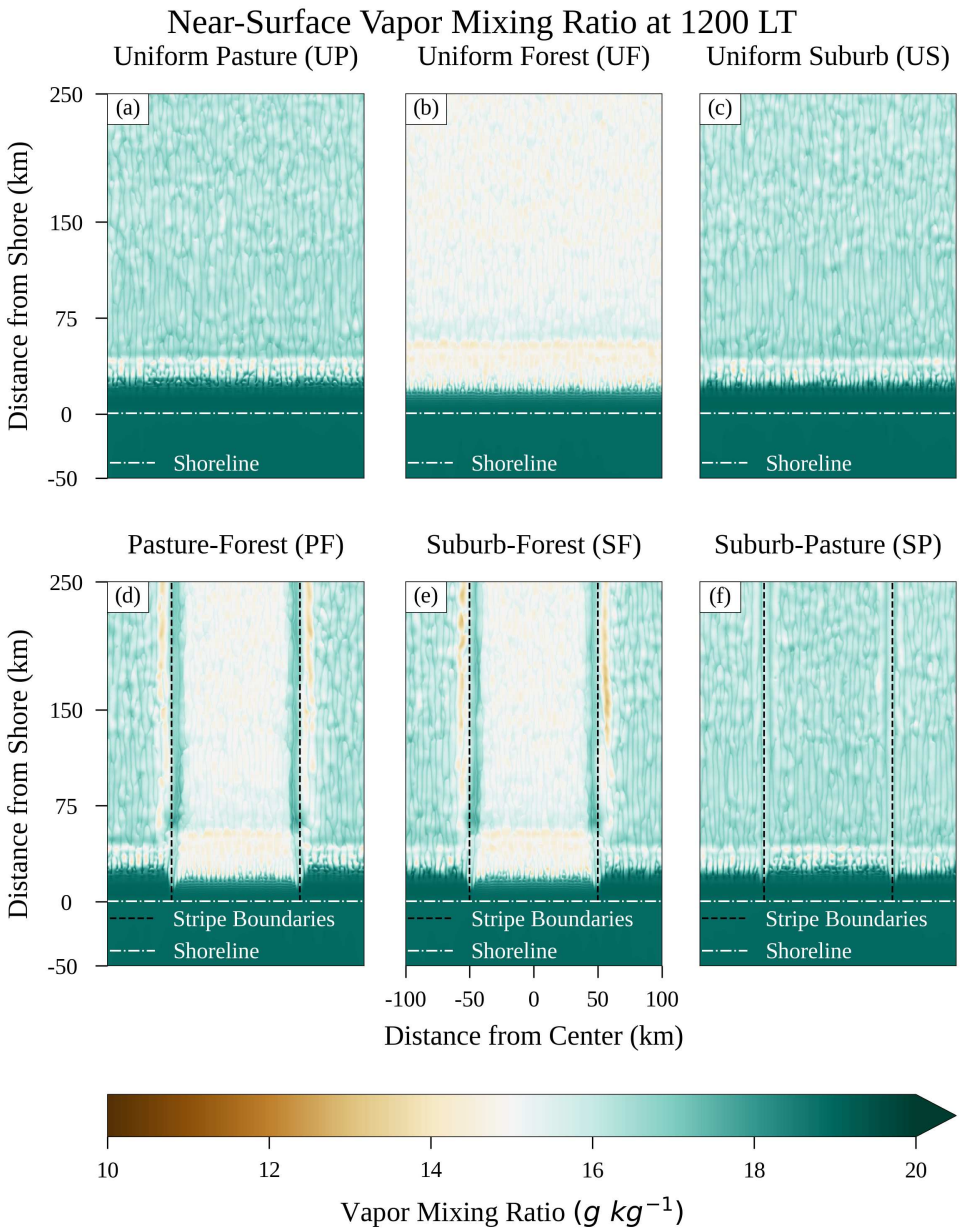

Figure 3.2: Plan view of water vapor mixing ratio at 200 m AMSL at 1200 LT. Increased low-level water vapor is present on the forest side of the vegetation boundary, while decreased water vapor is present on the pasture and suburban sides. The white dashed line indicates the shoreline, while the black dashed line indicates boundaries between land surfaces. To save space, the southernmost 100 km of the ocean have been omitted from this and similar plots.

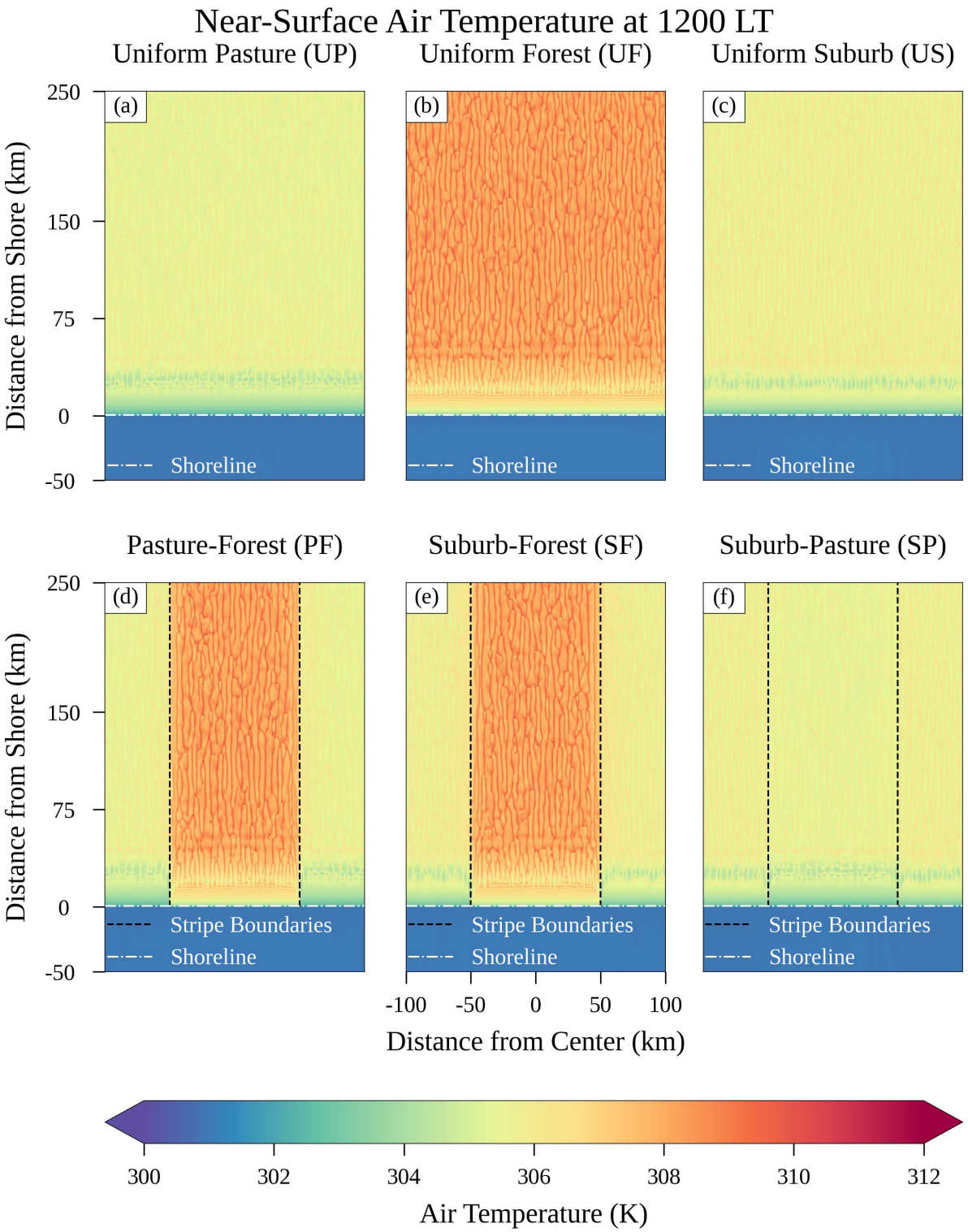

Figure 3.3: As in Figure 3.2, but for near-surface (15 m AMSL) air temperature at 1200 LT. The near-surface air temperature is greater over the forest than the pasture or suburbs.

Table 3.2: Land Surface Properties

Land Surface Type	Pasture	Suburbs	Coniferous Forest
Vegetation Broadband Shortwave Albedo	0.283	0.305	0.154
Vegetation Fraction	0.430	0.395	0.774
Surface Broadband Shortwave Albedo	0.179	0.184	0.129
Leaf Area Index	0.909	0.525	5.890
Vegetation Height (m)	1	6	20
Total Roughness Length (m)	0.100	0.602	2.716

simulations. However, even though deep convective storms as defined above occur throughout the domains of the UP, US, and UF simulations, they are strongest (with respect to cloud top heights and vertically integrated condensate) along and just inland of the sea breeze front, in association with near-surface convergence along the sea breeze front. In the UF simulation, for example, storms with cloud top heights above 10 km AMSL and vertically integrated condensate greater than 20 mm liquid equivalent are found primarily in a line which moves with the sea breeze front until 1440 LT, after which strong convective storms begin to develop inland of this line (Supplemental Animation 3b). These strong inland storms develop along intersections of HCRs and the cold pools produced by the initial weaker and shallower inland convection, and are not primarily driven by the cold pools from the strong convection associated with the sea breeze front (Supplemental Animation 2b).

In simulation UF, the first deep convection emerges at 1250 LT, while in simulations US and UP the onset of deep convection is delayed until 1400 and 1410 LT, respectively. The presence of deep convection in the UF simulation, and its absence in the UP and US simulations, at 1330 LT is evident in Figure 3.4a-c. The development of strong storms inland of the sea breeze, like that of the initial sea breeze induced deep convection, is delayed in the US and UP simulations relative to the UF simulation. In the Us and UP simulations, strong storms inland of the sea breeze front begin to develop at approximately 1530 LT in the US simulation and 1550 LT in the UP simulation (Supplemental Animation 3a,c), approximately 1 hour later than in the UF simulation. The difference in convective behavior between the UF and UP/US simulations is primarily driven by the

greater near-surface air temperature over the forest relative to the pasture or suburbs. The pasture and suburbs have nearly identical domain mean 15 m air temperatures of approximately ~ 305.5 K at 1200 LT (Figure 3.3a,c) and ~ 308.7 K at 1500 LT (Supplemental Animation 2a,c). By contrast, the coniferous forest has a domain mean 15 m air temperature of approximately ~ 308.3 K at 1200 LT (Figure 3.3b), and ~ 309.9 K at 1500 LT (although by 1500 LT, cold pools from convective storms are widespread over the forest, contaminating temperature estimates) (Supplemental Animation 2b).

The reasons for the greater near-surface air temperatures over the forested areas are twofold: first, the greater vegetation fraction of the coniferous forest as opposed to the pasture or suburbs means that more of the incoming solar radiation is absorbed by the vegetation rather than the soil (Table 3.2). This in turn allows more energy to be transferred to the model canopy layer as opposed to being stored in the ground. Secondly, the greater vegetation roughness length of the coniferous forest as opposed to the pasture or suburbs allows for more efficient mixing of this canopy layer air with the overlying atmospheric air, thereby facilitating more sensible heating of the atmosphere. These greater near-surface air temperatures over the forest increase the PBL height in the UF simulation compared to the UP and US simulations. This means that air parcels can more easily reach their LCL and LFC in the UF simulation, allowing an earlier onset of deep convection compared to the UP and US simulations.

On the other hand, the reduced latent heating over the forest relative to the pasture or suburbs is primarily due to the forest's greater vegetation fraction. Because the soils are dry throughout their entire depth in all simulations, stomatal resistances of the forest, pasture, and suburbs are large, preventing almost all transpiration. As a result, what little latent heat flux does occur is driven by direct evaporation from soil. Because little radiation reaches the soil under the forest due to the forest's large vegetation fraction (Table 3.2), little energy goes into evaporating water from the soil under the forest, thereby reducing latent heat flux over the forest. By contrast, more radiation is able to reach the soil through the low vegetation fractions of pasture and suburbs to evaporate water from there. The differences between forest and pasture and suburb are visible in

Figure 3.5a-c, where the surface latent heat fluxes over the forest in the UF simulation is lower than those over the pasture and suburb in the UP and US simulations. Partially as a result of this greater latent heat flux over the pasture and suburb, vapor mixing ratios at 200 m above ground at 1200 LT are approximately 15.0 gkg^{-1} over the forest and 16.9 gkg^{-1} over the pasture and suburb (Figure 3.2a-c).

The differences in surface latent heat fluxes between the forest and pasture and suburb are not the entire reason for the greater near-surface mixing ratios over the pasture and suburbs, however. The deeper boundary layer over the forest allows for vertical mixing of moisture compared to the pasture or suburbs, in which water vapor is more concentrated near the surface in the shallower and more stable boundary layers over these land surfaces. This reduction of near-surface water vapor mixing ratio increases the mean cloud base height in the UF simulation, which at 1800 LT is 2010 m AMSL, compared to 1531 m in the UP simulation and 1532 m in the US simulation (not shown).

The earlier emergence and greater coverage of strong deep convective storms in the UF simulation compared to the US/UP simulations leads to greater rainfall totals over the UF domain compared to the UP or US domains. The mean accumulated rainfall in the UF simulation is ~ 0.875 mm, which is $\sim 70\%$ and $\sim 49\%$ more the mean rainfall in the UP and US simulations (~ 0.515 mm and ~ 0.588 mm, respectively) (Figure 3.6a-c).

South of approximately y = +100 km in simulations UP and US, and y = +75 km in the UF simulation, the boundary layer is cooled and moistened by the southerly inflow of marine air from the south. This results in a stabilized boundary layer with little Convective Available Potential Energy (CAPE, not shown) which inhibits deep convection close to the coast (Figure 3.6a-c). *To avoid including this marine-influenced air in our subsequent discussions of atmospheric properties and convection over different surfaces, subsequent comparisons of environmental variables and precipitation between simulations will focus only on the region north of y = +100 km.* The fact that convection is able to occur 25 km closer to the coast in the UF simulation compared with the US or UP simulations, despite the slightly faster sea breeze in the UF simulation, indicates that

the forest more rapidly destabilizes the overlying atmosphere compared to the pasture or suburbs. This faster destabilization is due to the greater sensible heat flux over the forest compared to the pasture and suburbs (Figure 3.7a-c).

3.3.2 Striped Land Surface Simulations

The rainfall patterns in simulations PF and SF, which consist of a stripe of forest surrounded by stripes of pasture and suburbs, respectively, are completely different from those of the uniform land surface simulations. Again, the influence of the marine air in suppressing convection near the coast is clearly visible in Figure 3.6d-f. As before, our subsequent comparisons of the different simulations will thus focus only on the region north of y = +100 km to avoid the effect of this marine-influenced air. However, while the coverage of rainfall was scattered more or less randomly inland of approximately 75 km from the coast in the UP, UF, and US simulations, the rainfall in simulations SF and PF is heavily concentrated over the forest, with comparatively little rainfall over the pasture or suburbs (Figure 3.6d,e). The reasons for this are driven by thermodynamic differences between the forest and the surrounding pasture and suburbs, and are discussed in greater detail below.

In addition to there being more rainfall overall in the forested areas, a line of heavy rainfall is present in the center of the forest stripe in both the PF and SF simulations (Figure 3.6d,e). Notably, the accumulated rainfall totals over the forest in these striped simulations are greater than in the uniform land surface simulations. In simulations PF and SF, the mean rainfall over the forest is ~ 1.795 mm and ~ 1.858 mm, a $\sim 105\%$ and $\sim 112\%$ increase in accumulated rainfall per unit area compared to the uniform forest simulation.

However, while rainfall is enhanced over the forest, it is suppressed over the pasture and suburbs. Over the pasture in simulation PF, mean rainfall is ~ 0.252 mm, a $\sim 51\%$ decrease from the average rainfall per unit area over the uniform pasture. Over the suburbs in simulation SF, mean rainfall is ~ 0.372 mm, a $\sim 37\%$ decrease from the average rainfall per unit area over the uniform suburbs.

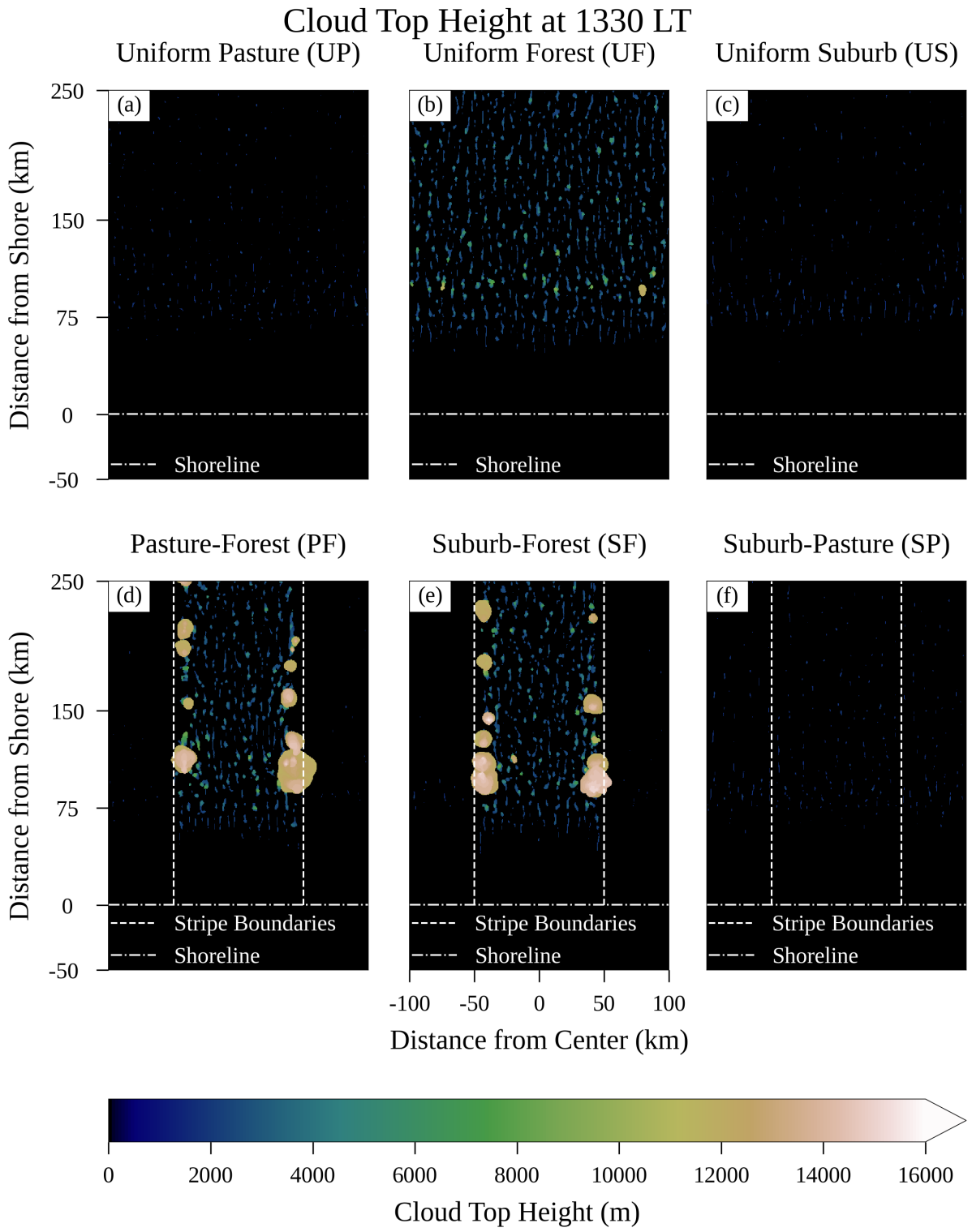

Figure 3.4: Plan view of cloud top heights at 1330 LT. Coverage of high cloud tops is greater in simulations PF and SF than in the other four simulations. The shoreline and land surface boundaries are denoted by horizontal and vertical white dashed lines, respectively.

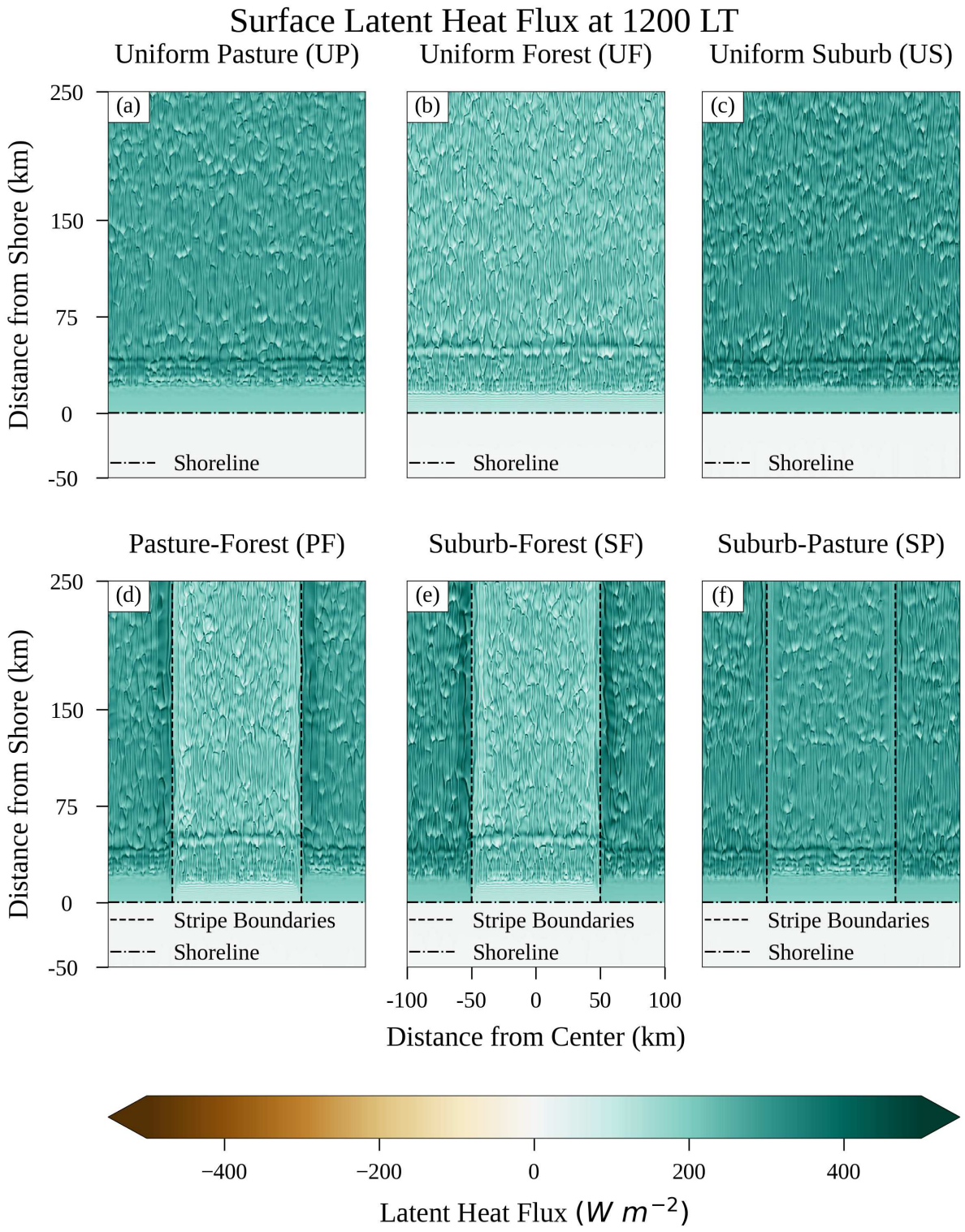

Figure 3.5: As above, but for surface latent heat flux at 1200 LT. Latent heat fluxes are larger over the pasture and suburbs relative to the forest.

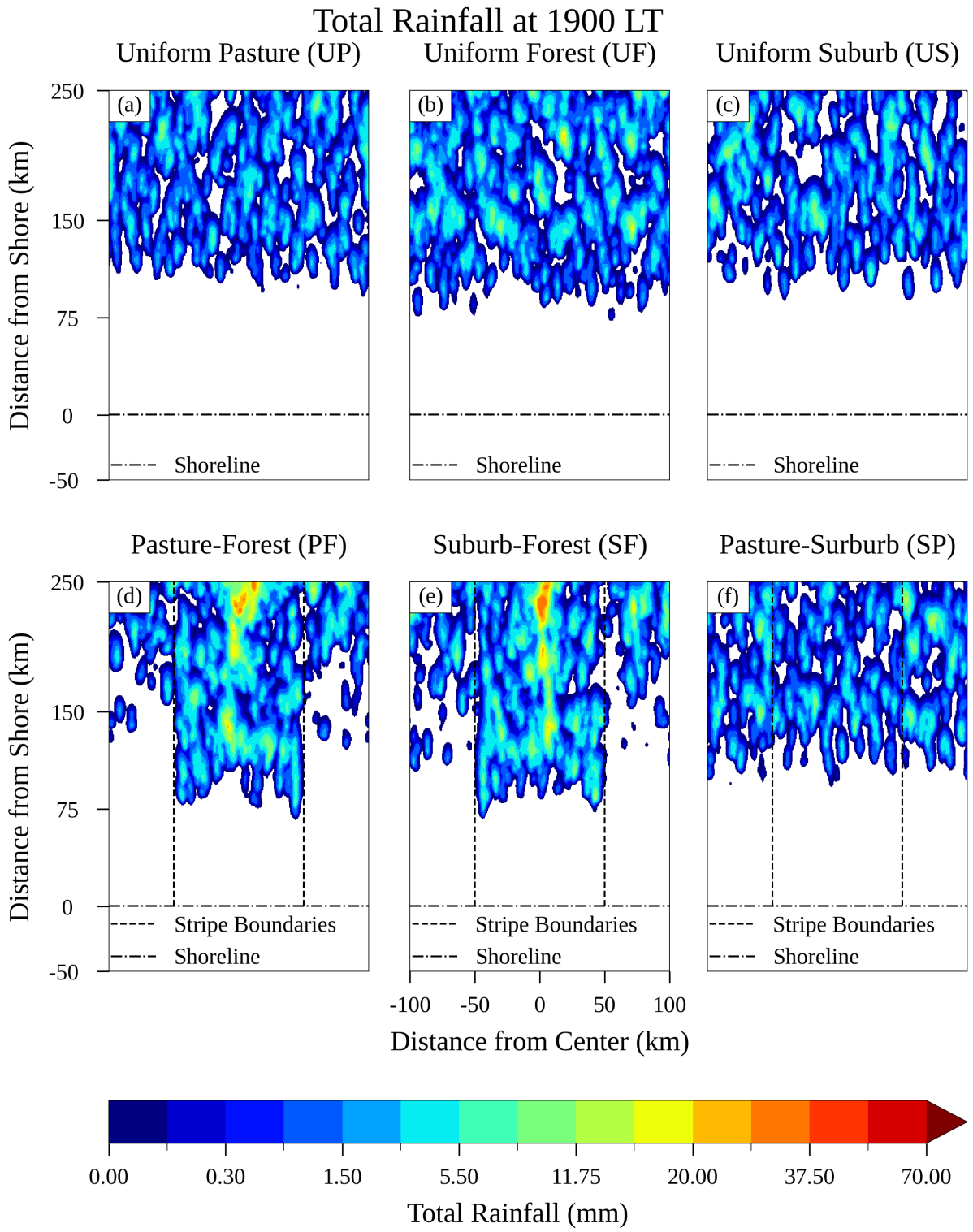

Figure 3.6: As in Figure 3.2, but for total accumulated rainfall over the course of the simulation. Rainfall in (d,e) is enhanced over the forest compared to over the surrounding pasture and suburbs, respectively.

Interestingly, even with the decreases in rainfall over the pasture and suburbs compared to the UP and US simulations, simulations PF and SF both have greater domain-total rainfall than any of the uniform land surface simulations. Simulation PF has a mean accumulated rainfall of ~ 1.02 mm over all land, which is $\sim 17\%$, $\sim 74\%$, and $\sim 99\%$ more than the mean accumulated rainfall in the UF, US, and UP simulations, respectively. Simulation SF has a mean accumulated rainfall of ~ 1.12 mm over all land, a $\sim 27\%$, $\sim 90\%$, and $\sim 117\%$ increase over the mean accumulated rainfall in the UF, UP, and US simulations.

In our discussions of the processes in the PF, SF, and SP simulations, I will refer to the situation at 1200 LT when discussing the convective environment over the forest, pasture, and suburbs. I choose this time because the environmental conditions and dynamical processes at that time are representative of those in the pre-storm environment of the simulation.

As mentioned above, patterns of rainfall in the PF and SF simulations are driven by differences in thermodynamics between the forest and pasture/suburbs. Similar to the uniform land surface simulations, the forested areas in simulations PF and SF are approximately 3K hotter than the surrounding pasture and suburbs, respectively, at 1200 LT (Figure 3.3d,e). The greater near-surface air temperature over the forest is driven by larger sensible heating over the forest compared to the pasture/suburbs (Figure 3.7d,e). At 1200 LT, the average sensible heat flux over the forest in simulations PF and SF are approximately 397.7 $W\ m^{-2}$ and 397.5 $W\ m^{-2}$, respectively. Over the pasture in simulation PF and the suburbs in simulation SF sensible heat fluxes are just 240.0 $W\ m^{-2}$, and 251.8 $W\ m^{2}$, respectively. At the same time, the average latent heat flux over the forest in simulations PF and SF are 216.4 $W\ m^{-2}$ and 216.2 $W\ m^{-2}$, compared to 284.68 $W\ m^{-2}$ over the pasture in simulation PF and 300.61 $W\ m^{-2}$ over the suburbs in simulation SF (Figure 3.5d,e). This difference in latent and sensible heat fluxes leads to different Bowen ratios between the pasture/suburbs and forest (Figure 3.8d,e).

The different average vertical profiles of temperature and dewpoint over the forest and pasture can be seen in Figure 3.9. The average vertical profile over the suburbs is not shown as it is nearly identical to that of the pasture. The boundary layer over the forest is warmer and deeper than

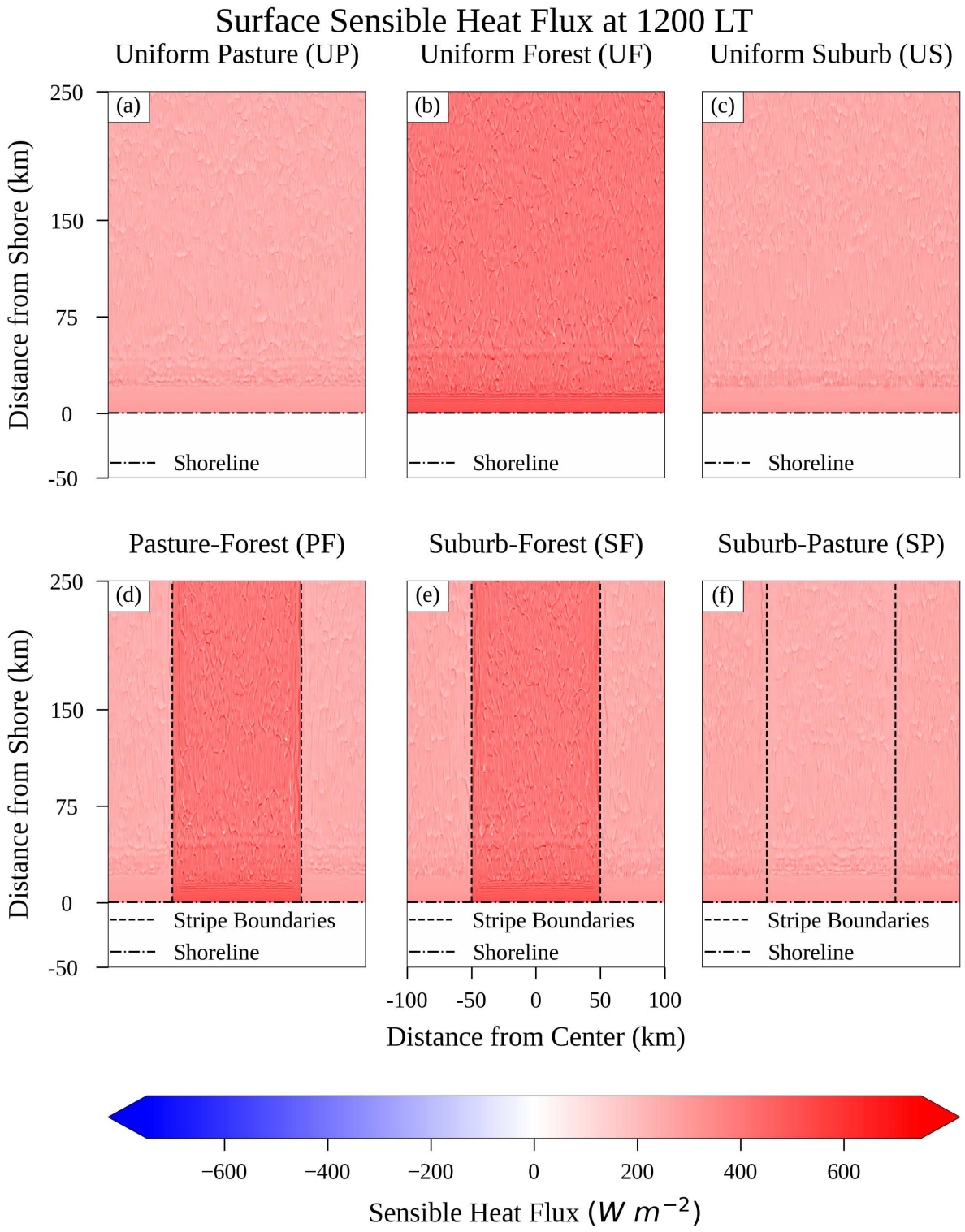

Figure 3.7: As above, but for surface sensible heat flux at 1200 LT. Sensible heat flux is greater over the forest relative to the pasture and suburbs.

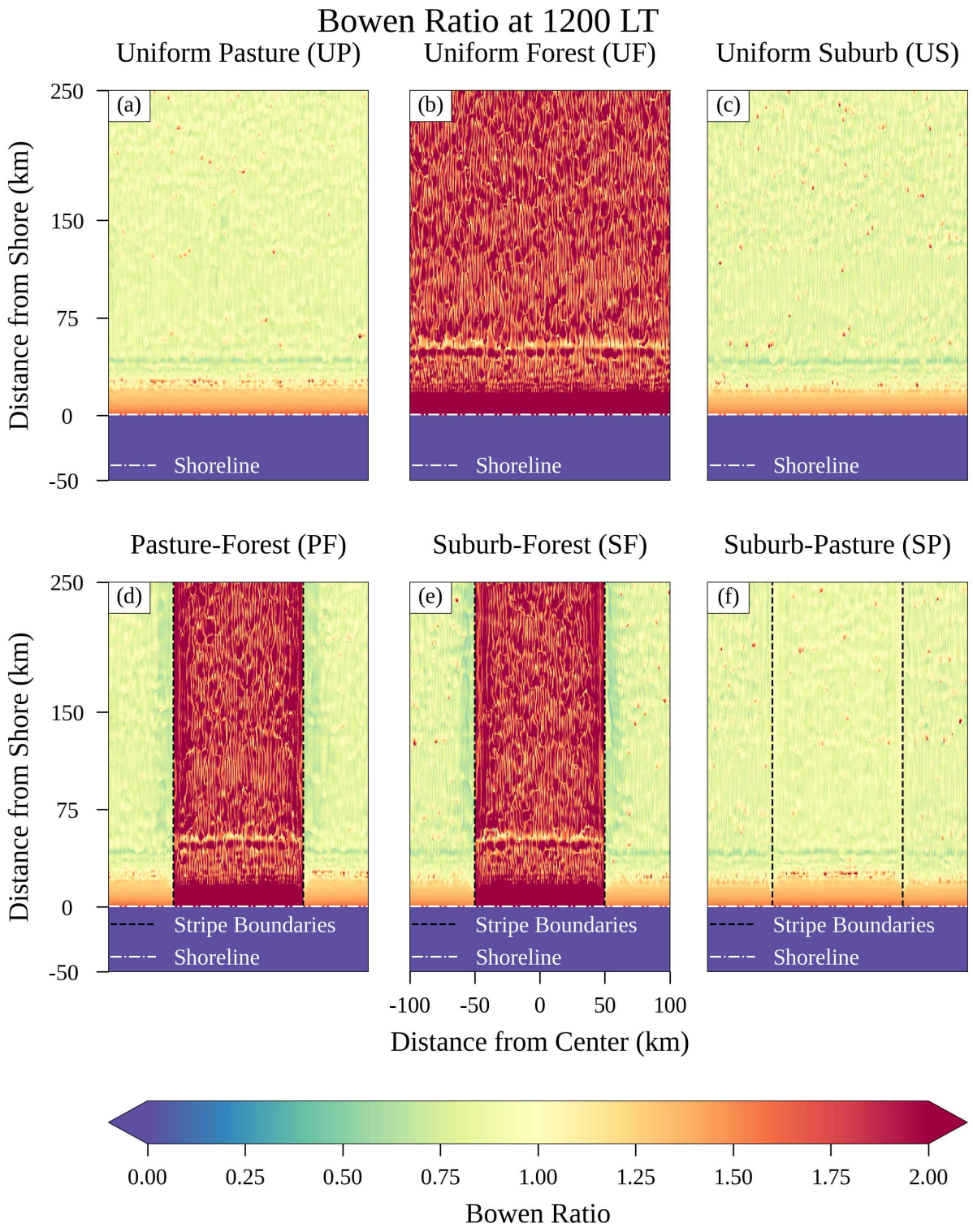

Figure 3.8: As above, but for the surface Bowen ratio at 1200 LT. The Bowen ratio is greater over the forest than the suburbs or pasture.

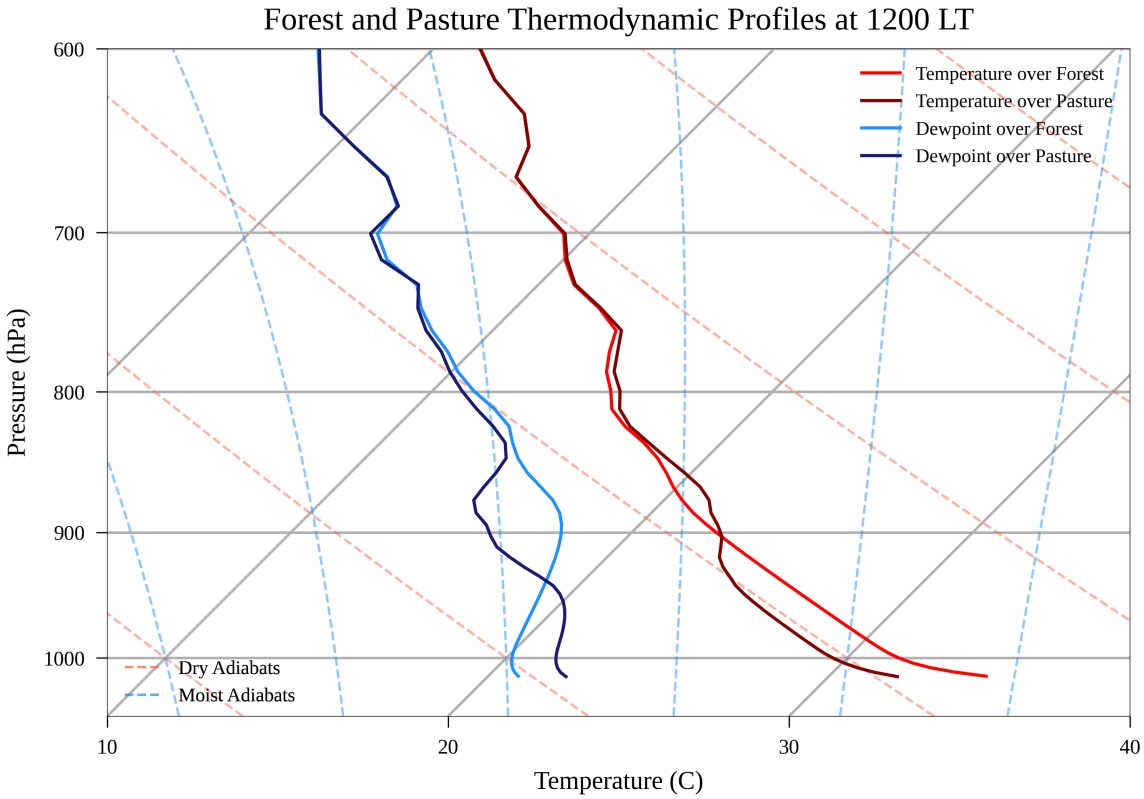

Figure 3.9: Skew-T/Log-P diagram illustrating the warmer and deeper boundary layer of the coniferous forest compared to the pasture in the PF simulation. Temperature and dewpoint averaged over the center 50 km of forest north of y = +100 km are shown in red and light blue lines, respectively. Temperature and dewpoint averaged over the center 50 km of the pasture stripe north of y = +100 km are shown in maroon and dark blue lines, respectively.

that over the pasture, driven by the greater temperatures over the forest. As discussed above, this deeper boundary layer over the forest increases the vertical mixing of water vapor throughout the PBL over the forest compared to the pasture and suburbs. While vapor mixing ratios over the forest are lower than those over the pasture below 950 hPa, they are actually greater above 950 hPa. This greater level of moisture in the upper boundary layer over the forest reduces the effects of dry air entrainment on parcels rising to their LCL and LFC compared to over the pasture and suburbs. This lowers the thermodynamic barriers to convection initiation over the forest stripe compared to over the pasture and suburbs.

The greater near-surface air temperature over the forest relative to the pasture or suburbs leads to lower near-surface air pressures (Figure 3.10d,e). The average surface air pressure over the forest in both the SF and PF simulations at 1200 LT is approximately 1017.40 hPa, compared to 1017.04 hPa for both the suburbs and pasture in the SF and PF simulations, respectively. This lowered surface pressure over the forest in turn induces solenoidal mesoscale circulations similar to those described by Anthes (1984), with near-surface convergence over the forest (Figure 3.11). This near-surface convergence subsequently produces rising motion over the forest, divergence aloft above the forest, upper-PBL convergence and associated sinking motion over the pasture, and near-surface divergence over the pasture (Figure 3.12).

The near-surface convergent branches of these land surface-induced solenoidal circulations advect more moist air from the pasture and suburbs stripes over the forest, similar to what has been seen in other idealized simulations in which low-level flow from cooler/wetter to hotter/drier patches advects moisture over the hotter/drier patch (Rieck et al., 2014; Lee et al., 2019; Cioni and Hohenegger, 2018; Harvey et al., 2022; Kawase et al., 2008; Chen and Avissar, 1994; Avissar and Liu, 1996; Hong et al., 1995; Emori, 1998). This moisture then rises just inside of the forest edge, creating a plume of greater vapor mixing ratios which lowers the LFC and LCL locally (Figure 3.13a,b). This has a noticeable effect on cloud base heights over the forest, with cloud bases in these plumes approximately 300 m lower than cloud bases in the center of the forest stripe (not shown).

It is unclear whether the lowered LCL and LFC in these plumes is more important for the initiation of deep convection than the direct mechanical lifting associated with the rising branches of these circulations. Nevertheless, the fact that deep convection initiates nearly simultaneously at 1230 LT in the PF and SF simulations just inside the forest edges suggests that the combination of these two effects is sufficient to initiate deep convection. This convection initiation also occurs 20 minutes earlier than the initiation of deep convection in the UF simulation. Furthermore, a mere 20 minutes later at 1250 LT in the PF and SF simulations, these first deep convective storms have reached heights above 12 km, something that does not occur in the UF simulation until 1320 LT,

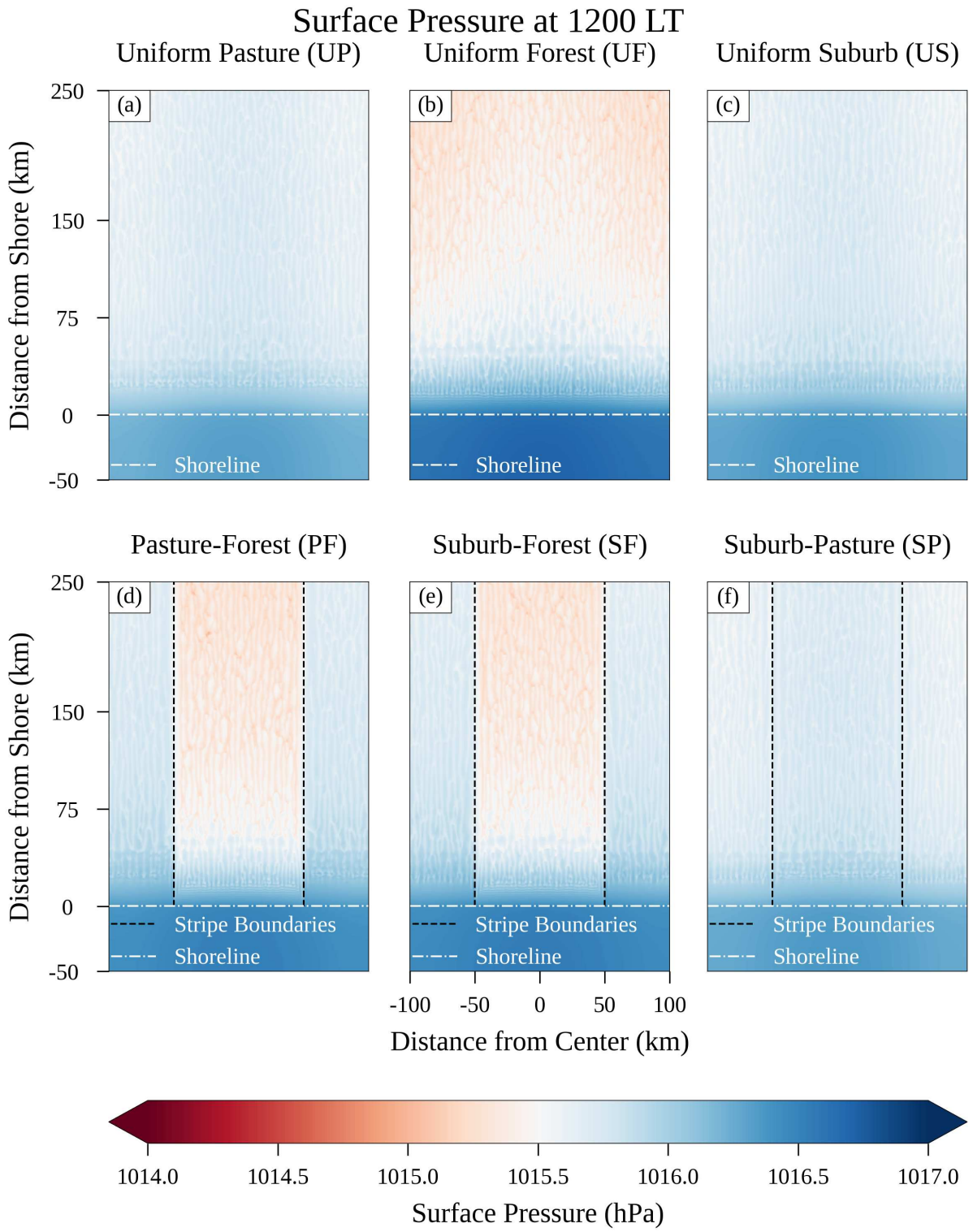

Figure 3.10: Plan view of air pressure at the surface. Surface air pressure is lower over the forest than over the surrounding pasture and suburbs.

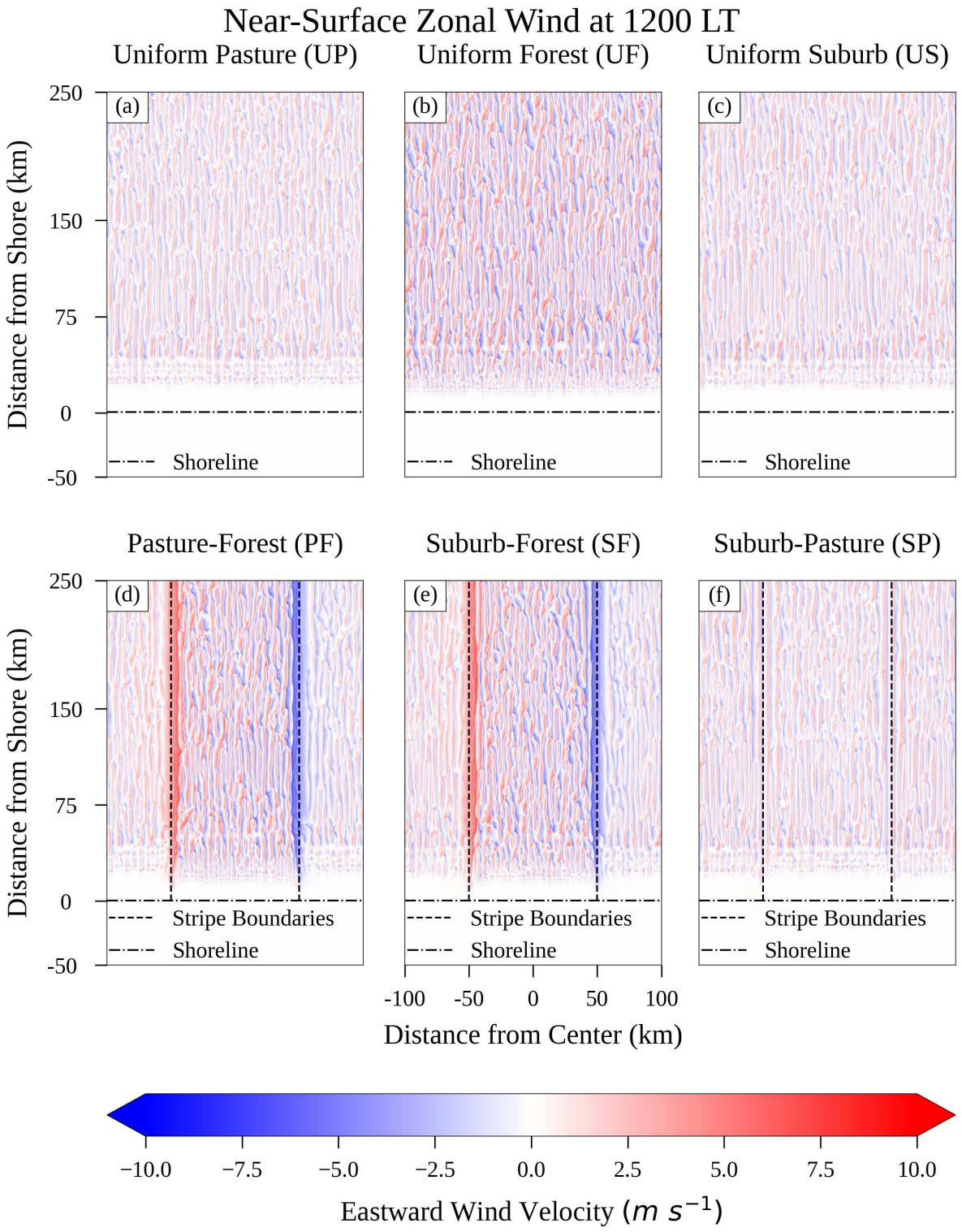

Figure 3.11: Plan view of zonal winds at 200 m above sea level. Converging zonal winds at the edges of the forest are seen in d,e.

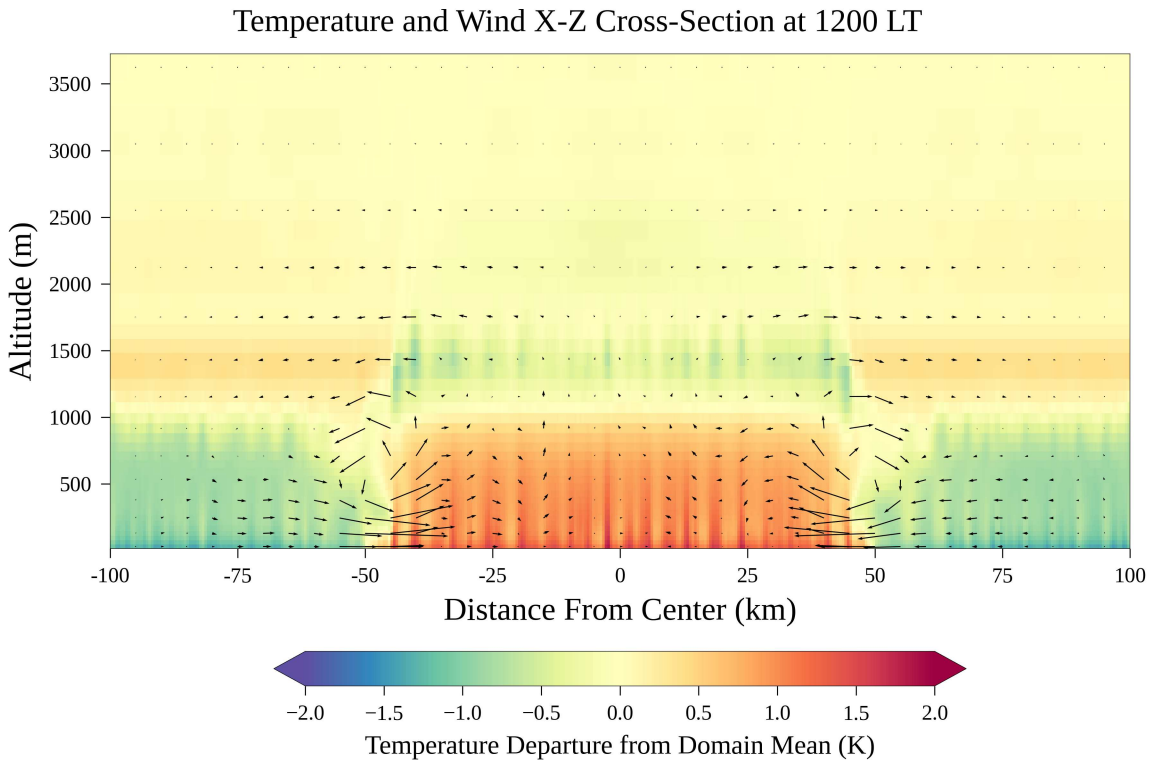

Figure 3.12: X-Z vertical cross-section showing wind (in arrows) and air temperature (in shading) at 1200 LT in the PF simulation averaged over the y direction from y = +100 km to y = +250 km. A circulation with rising motion over the forest and sinking motion over the pasture is visible at x = +50 km and x = -50 km.

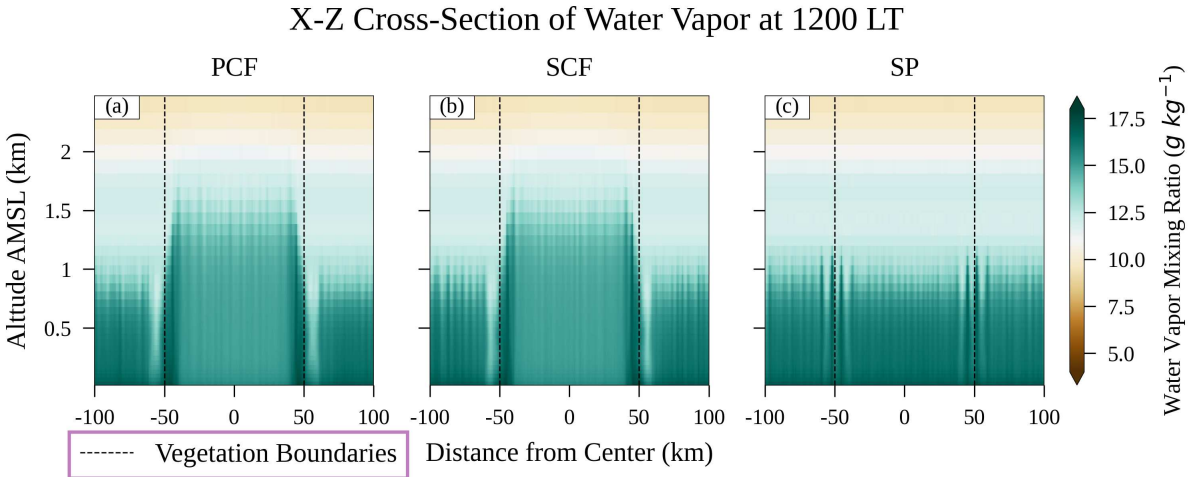

Figure 3.13: X-Z vertical cross-section of water vapor mixing ratio (shaded) at 1200 LT in the PF, SF, and SP simulations, averaged over the y direction from y = +100 km to y = +250 km. "Plumes" of increased water vapor mixing ratio are seen at the edges of the forest in a,b.

30 minutes after convection initiation in that simulation. These results clearly indicate that the rising branches of the land surface-induced solenoidal circulations accelerate the development of deep convection. Figure 3.4d,e clearly shows the wide areal coverage of convective clouds with heights above 12 km (including convective anvils) just inside the edges of the forest stripe at 1330 LT, while only two storms have reached this height in the UF simulation.

In addition to the rising branches of the solenoidal circulations along the edges of the forest, the sea breeze is an important, if not primary, determinant in the initiation of the first storms in the PF and SF simulations. The first deep convective storms in both simulations occur along the edges of the forest at the meridional position of the sea breeze front, which is approximately 75 km north of the coastline at this time. Plan views of vertical velocity at 1 km AMSL (not shown) confirm that the intersection of the two circulations (land surface-induced and sea breeze) in these regions leads to the strongest lifting in the domain, helping initiate the first convective storms there. However, unlike the UF simulation in which the strong convective storms are restricted to the sea breeze front until nearly 2 hours after the emergence of the first deep convective storms, strong storms are visible along the forest edges well inland of the sea breeze front by 1310 LT, only 50 minutes after the first emergence of deep convection in the PF and SF simulations. *This indicates that the solenoidal circulations induced by the vegetation boundary are more important than the sea breeze front in determining the location and timing of convection initiation.* Figure 3.4 shows this same general behavior at a slightly later time, where tall convective storms can be seen in the PF and SF simulations along the length of the forest edges.

While the land surface-induced solenoidal circulations enhance convection over the forest, they suppress it over the pasture and suburbs. Referring again to Figure 3.12, we see that there are clear sinking motions on the pasture side of the land surface boundary, which bring drier air from aloft down to the surface. In addition to this vertical transport of dry air, which can also be seen in Figure 3.13a,b, the sinking branches of the solenoidal circulations act to warm the atmosphere in this region by adiabatic compression. However, these two effects are localized to a small region along the edges of the pasture and suburbs, and cannot account for the suppression of precipitation seen

across the entire pasture and suburb regions in Figure 3.6d,e. At 1000 m and 1500 m AMSL, temperatures over the entire pasture and suburban stripes in the PF and SF simulations, respectively, are greater than the temperatures at those altitudes over the pasture and suburbs in the UP and US simulations (Figure 3.12). This indicates that upper-PBL warming is produced by the broad, weak divergent flow regions of the solenoidal circulations. I suspect that this upper-PBL warming is the result of weak adiabatic compression which accompanies these branches of the solenoidal circulations and which acts to stabilize the upper levels of the boundary layer above the pasture and suburban stripes. This warming also increases the dewpoint depression at these levels, thereby exacerbating the effects of dry air entrainment on parcels rising to their LCL and LFC. Compare the vertical profiles of temperature and dewpoint of the forest and pasture in Figure 3.9. The upper boundary layer over the pasture is warmer and drier than over the forest. The combined effects of the diverging, downward branches of the land surface-induced solenoidal circulations with in the PF and SF simulations act to suppress convective development and precipitation over the pasture and suburban stripes relative to their uniform simulation counterparts.

Returning again to the forest stripe in the PF and SF simulations, the evolution of convection after the initiation of the first storms is quite different from the initial convective development. As the first storms along the forest edges mature, they produce precipitation. Cold pools develop as this precipitation evaporates and spread inward toward the edge of the forest (Supplemental Animation 2d,e). These cold pools notably remain almost entirely confined to the forest stripe for many hours after the emergence of deep convection, likely as a result of the convergent flow into the forest from the land surface-induced solenoidal circulation. They do expand inward toward the center of the forest stripe, reinforcing the pattern of inflow as they do so. As they expand inward, lifting along the cold pool edges triggers new convection further inside the forest. As these new cold pool-induced storms develop, they too produce cold pools which further reinforce the low-level inflow. This feedback acts to propagate the low-level winds associated with the original land surface-induced solenoidal circulations inward toward the forest center, as is seen in Figure 3.14 between 1300-1500 LT. These results are in general agreement with those of Rieck et al.

(2015). The two sides of this low-level inflow collide at roughly 1500 LT at y = +125 km at the center of the forest, although the collision happens approximately 30 minutes later at the northern end of the forest. Examining Figure 3.14, I should note that although the inflow does propagate inward without assistance of cold pools between 1000 and 1300 LT, it does so slowly. Without the assistance from cold pools in propagating this circulation inward toward the forest center, it is possible the circulations may not have collided in the center of the forest at all.

The collision of the sides of this low-level inflow, and the convergence associated with this collision, triggers intense mechanical lifting in the center of the forest, initiating intense convection along the center line of the forest from approximately y = +125 km to y = +250 km. These convective storms quickly grow in intensity, with heights of over 14 km and vertically integrated condensate levels exceeding 50 mm liquid equivalent in many storms (Supplemental Animation 3d,e, 11d,e). Given the intensity of these storms, it is unsurprising that they lead to heavy precipitation totals, which are reflected by the stripe of heavy rainfall in the center of the forest strip in Figure 3.6d,e.

These collision-initiated storms also produce intense cold pools associated with the evaporation of the heavy precipitation along the center of the forest stripe. By 1600 LT, the average 15 AMSL air temperature over the forest has decreased to ~ 302.8 K in the PF simulation (Figure 3.15) and ~ 302.0 K in the SF simulation, compared to ~ 309.6 K for both the pasture and suburbs in the PF and SF simulations, respectively (Supplemental Animation 3d,e). I should note that these lower temperatures are restricted to $y > +100km$, where convective storms have developed over the forest. South of this line, the forest remains warmer than the surrounding pasture and suburbs. This leads to *two* distinct circulation patterns that are now present at each forest boundary. North of y = +100 km, the lower temperatures over the forest produced by the strong cold pool have induced higher pressures there than the surrounding suburbs or pasture (approximately 1.2 hPa higher over the forest than pasture in the PF simulation and 1.3 hPa higher than the suburbs in the SF simulation), which in turns leads to *divergent* near-surface flow over the forest (Figure 3.14). This divergent flow advects cool, moist air from the forest over the pasture and suburbs. These

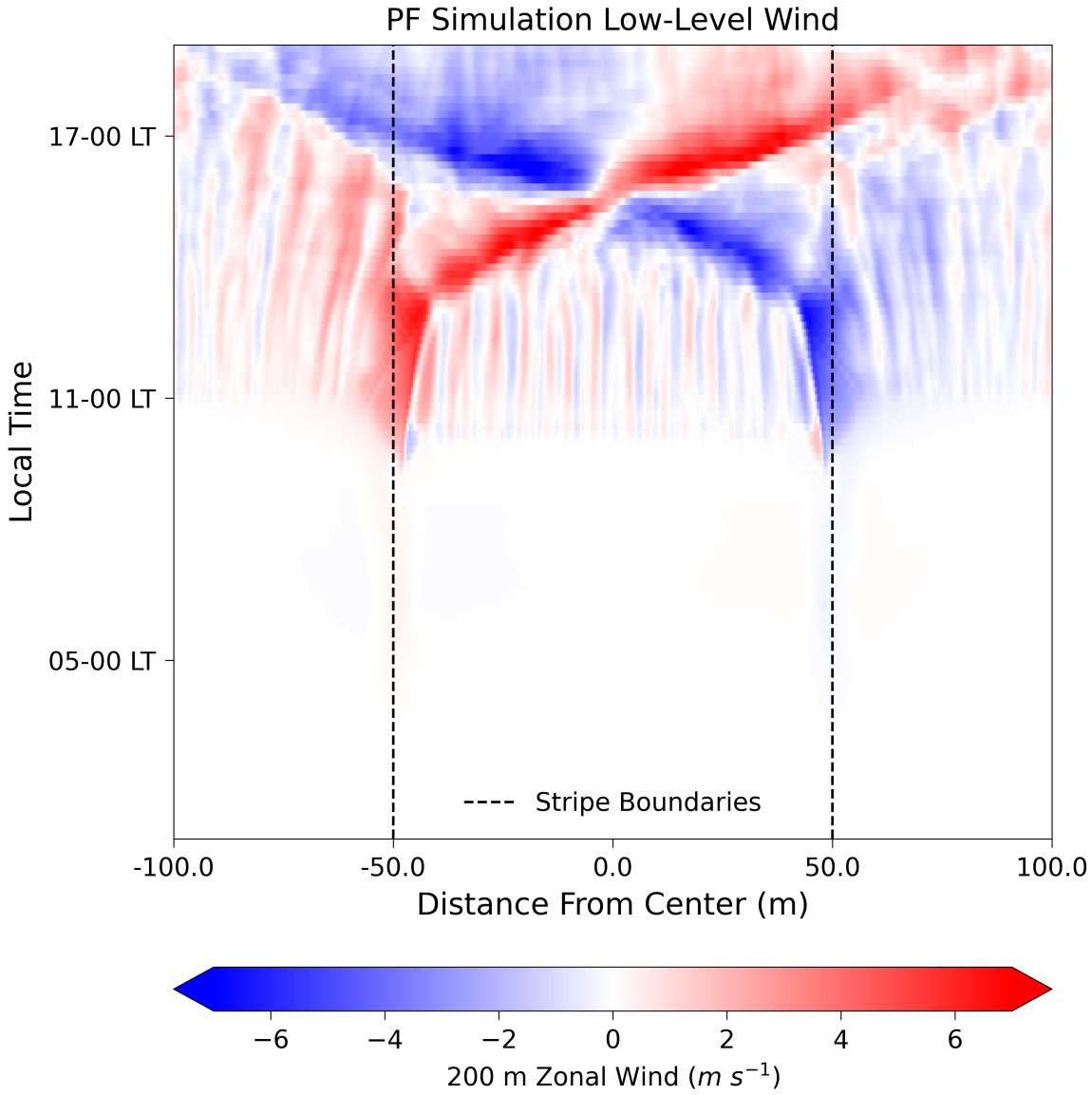

Figure 3.14: Hövmoller Diagram of 200 m zonal wind velocity in the PF simulation averaged over the y-direction from y = +100 km to y = +250 km. Distance from the center of the forest stripe is shown on the x axis, while time is displayed on the y axis. The collision of the two converging branches of the solenoidal circulations in the middle of the forest stripe can be seen at 1530 LT.

findings are in line with those of Harvey et al. (2022), who noted that after deep convection had initiated and cold pools had been produced over the drier patches, inflow over the dry patches transitioned to outflow associated with the cold pools. South of y = +100 km, the temperatures over the forest remain greater than those over the pasture and suburbs, resulting in lower pressures and continued near-surface inflow over the forest from the original solenoidal circulations (Supplemental Animation 9d,e).

The cold pool circulation and the residual vegetation boundary-induced solenoidal circulation intersect over the forest at y = +100 km, resulting in the initiation of new deep convection along this line after 1600 LT (Supplemental Animation 2d,e, Supplemental Animation 3d,e). Additionally, storms form over the pasture and suburbs in the PF and SF simulations, respectively, as the cold pool from the forest spreads outward.

In contrast to the PF and SF simulations, the differences between the SP simulation and the uniform land surface simulations are more subtle. The rainfall is concentrated over the suburbs, with a mean accumulated of ~ 0.729 mm compared with a mean accumulated rainfall over the pasture of ~ 0.464 mm (Figure 3.6f). This translates to an enhancement of accumulated rainfall per unit area over the suburbs of $\sim 24\%$ relative to the US simulation, and a decrease of $\sim 10\%$ over the pasture relative to the UP simulation. The mean accumulated rainfall in the SP simulation is ~ 0.596 mm, which is $\sim 1\%$ and $\sim 16\%$ more than the US and UP simulations, respectively. However, it is $\sim 32\%$ lower than the mean accumulated rainfall of the UF simulation.

The processes in the SP simulation behave differently from those of the PF and SF simulations. Unlike the coniferous forest, which is hotter and drier near the surface than either the pasture or suburbs, the suburbs and pasture have similar near-surface air temperatures, vapor mixing ratios, and pressures (Figures 3.3f, 3.2f, 3.10f). There are subtle differences, which arise as a result of the different albedos, roughness lengths, and vegetation fractions of the two surfaces (Table 3.2). In particular, the suburbs have slightly greater sensible and latent heat fluxes than the pasture at 1200 LT (Figures 3.7f, 3.5f). The suburbs and pasture have average latent heat fluxes of 296.9 Wm^{-2} and 278.9 Wm^{-2}, respectively, and average sensible heat fluxes of 253.0 Wm^{-2} and 241.1 Wm^{-2}.

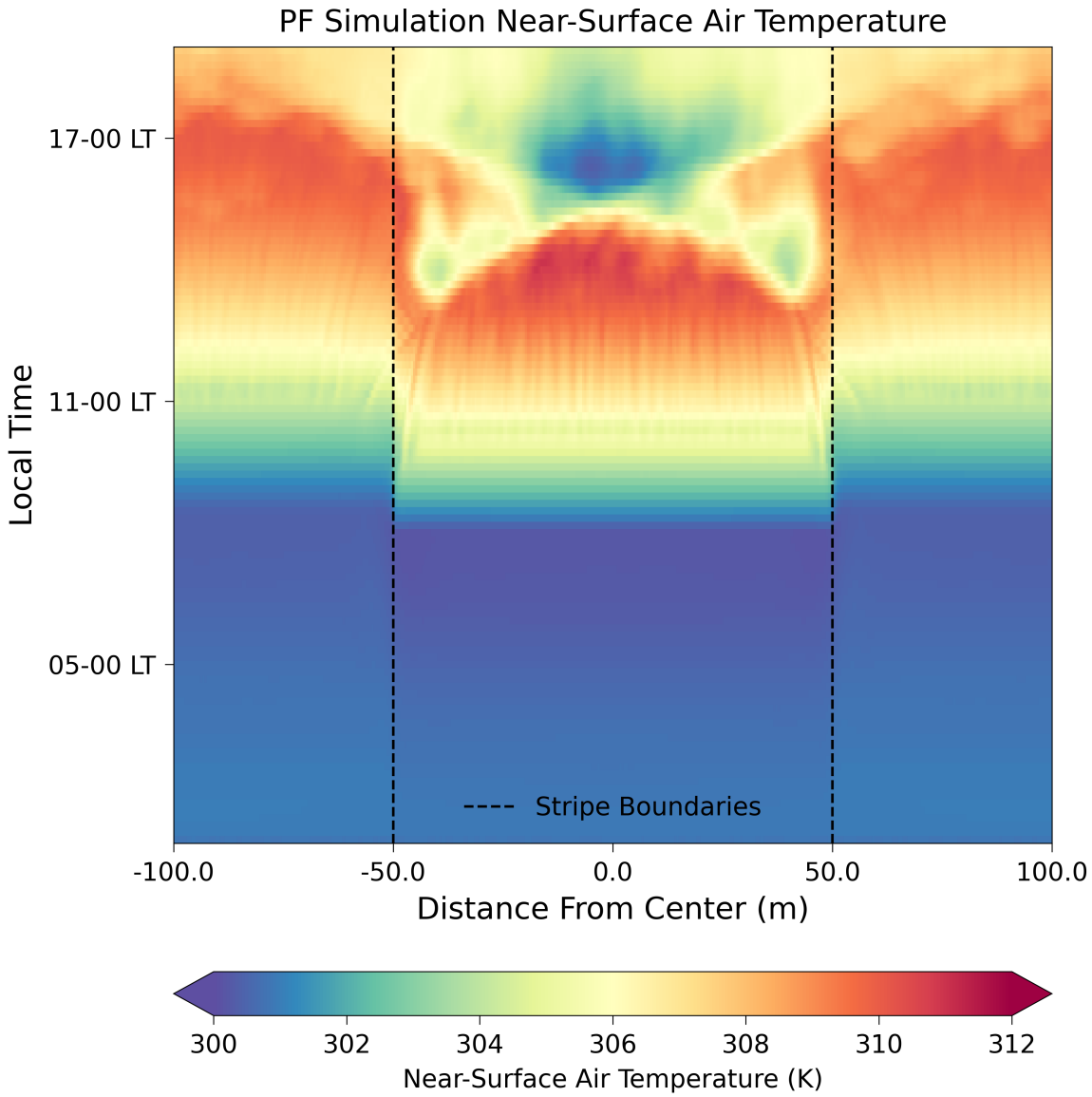

Figure 3.15: Hövmoller Diagram of near-surface (15 m AMSL) air temperature in the PF simulation averaged over the y-direction from y = +100 km to y = +250 km. X-and y-axes are as in Figure 3.14. Cold pools develop over the forest edges at approximately 1300 LT and spread inward toward the center of the forest. After 1600 LT, the forest becomes colder than the pasture as intense convection in the center of the forest generates strong cold pools.

Interestingly, this means that the suburbs and pasture have nearly identical Bowen ratios of 0.852 and 0.864, respectively, (Figure 3.8f). The slight difference in fluxes lead to 15 m AMSL air temperatures and 200 m vapor mixing ratios of ~ 305.8 K and ~ 305.5 K over the suburbs and pasture, respectively, and 200 m vapor mixing ratios of 16.32 $g\ kg^{-1}$ and 16.26 $g\ kg^{-1}$ (Figures 3.3f, 3.2f).

The difference in the Bowen ratio is primarily due to the slightly lower vegetation fraction of the suburbs compared to the pasture, which, as discussed above in Subsection 3.3.1, allows for greater latent heating. The reason for the overall greater surface fluxes over the suburbs are due to a combination of larger surface roughness length (0.602 m compared to 0.100 m for the pasture) and reduced longwave emissivity of the suburbs compared to the pasture (0.90 vs 0.95), which reduces the rate of energy loss from the vegetation by radiative cooling.

Because of the small differences in temperature, the surface pressures over the pasture and suburbs are similar, 1017.4 hPa over the pasture and 1017.3 hPa over the suburbs, respectively (Figure 3.10f). As a result, the solenoidal circulations which develop on the boundary between the suburbs and pasture in the SP simulation are weaker than those on the forest boundary in the PF and SF simulations. In fact, these boundaries are not readily distinguishable from the HCRs which appear throughout the domain when viewing plan views of zonal wind, near-surface air temperature, or 200 m water vapor mixing ratio (Figures 3.11f, 3.3f, 3.2f). However, looking at the vertical cross-section of water vapor, three plumes of vapor are visible around x = -50 km and x = +50 km, corresponding to the pasture-forest boundaries (Figure 3.13c). These plumes are similar in width and height to columns of larger and smaller water vapor mixing ratios seen elsewhere in the domain associated with HCRs. This suggests that, while there may not be strong solenoidal circulations at the pasture-suburban boundary, the small differences in temperature and pressure between these two surfaces do act to enhance HCRs near the boundary.

This local enhancement of HCRs does not affect the initial development of convection in the SP simulation. Unlike the PF and SF simulation, where deep convection initially developed just inside the forest boundary, deep convection in the SP simulation initially develops similarly to how

it does in the US and UP simulations (Supplemental Animation 3f). Initiation occurs along the sea breeze front at approximately y = +100 km at 1410 LT. After the initial round of deep convection, new storms develop at approximately 1630 LT over the enhanced HCRs on the suburban side of the vegetation boundary. These storms produce the heaviest precipitation of the simulation (Supplemental Animation 4f) and themselves account for the enhancement of rainfall over the suburbs in the SP simulation relative to the US simulation.

3.4 Discussion and Conclusion

To examine the role of vegetation heterogeneity and the sea breeze in convection initiation and development, I ran six idealized simulations of convection in a coastal environment. Three of these simulations (UP, UF, and US) employed a uniform vegetation type, while three simulations (PF, SF, and SP) contained two stripes of different vegetation type.

The results of this research indicate that the presence of sharp heterogeneities in vegetation type enhances the development of convective storms and precipitation. This enhancement occurs due to the presence of solenoidal circulations which arise from differences in PBL structure induced by differing adjacent vegetation types. In our PF and SF simulations, the near-surface air temperature over the forest, as a result of its higher vegetation fraction and roughness length, becomes greater than that over the surrounding pasture and suburbs. This greater near-surface temperature lowers surface pressure and produces higher PBL height over the forest than over its surroundings. This difference in pressure and PBL height induce near-surface convergence and rising motion over the forest, divergence aloft above the forest, and convergence aloft, sinking and near-surface divergence over the surrounding pasture/suburbs (Figure 3.12). The rising branches of these land surface-induced solenoidal circulations initiate convective storms along the boundary of the forest (Figure 3.4d,e). At the same time, the sinking branches of these circulations suppresse convection over the pasture and suburbs by warming the upper levels of the boundary layer over these vegetation types. Figure 3.16 presents a schematic which illustrates how the hotter forest receives more

rain as a result of converging and rising solenoidal circulations, while the downward branches of these circulations suppress precipitation over the surrounding pasture.

The rising branches over the forest appear to be more important in determining the location and timing of convection initiation in the PF and SF simulations than the sea breeze. Unlike in the uniform land surface simulations, in which strong convection is initially limited to being along the sea breeze front, in simulations PF and SF strong convection initiates along the forest boundary, not just along the sea breeze front. I did find that the intersection of the sea breeze front with the land surface-induced solenoidal circulations initiates the first convective storms in the PF and SF simulations, but within 20 minutes strong convection develops elsewhere along the forest boundary.

The first storms initiated along the forest boundary, driven by the rising branches of the land surface-induced solenoidal circulations, produce precipitation which evaporates near the surface to produce cold pools. These cold pools spread inward toward the center of the forest, propagating the pattern of near-surface inflow over the forest inward toward the center of the forest stripe (Figure 3.14). As the two sides of the inflow collide along the center of the forest, they initiate intense convective storms as a result of strong mechanical lifting. These convective storms then produce heavy precipitation along the center of the forest stripe (Figure 3.6d,e). The propagation speed of the inflow branches prior to the development of cold pools suggests that they may not have collided in the center of the forest stripe without reinforcement from cold pools. The intensity of the collision-initiated storms in the center of the forest stripe, and the role of cold pools in that collision, suggests that the interaction of cold pools with vegetation-induced solenoidal circulations enhances convection initiation. At the same time, it appears that cold pools are primarily responsible for the destruction of these circulations later in the day. The forest becomes colder than the surrounding pasture and suburbs after 1600 LT, leading to higher pressure over the forest and near-surface divergence from the forest to the pasture and suburbs (Figures 3.15, 3.14).

Although similar types of solenoidal circulations induced by vegetation heterogeneity have been described in literature including Anthes (1984); Wang et al. (2011); Lee and Kimura (2001);

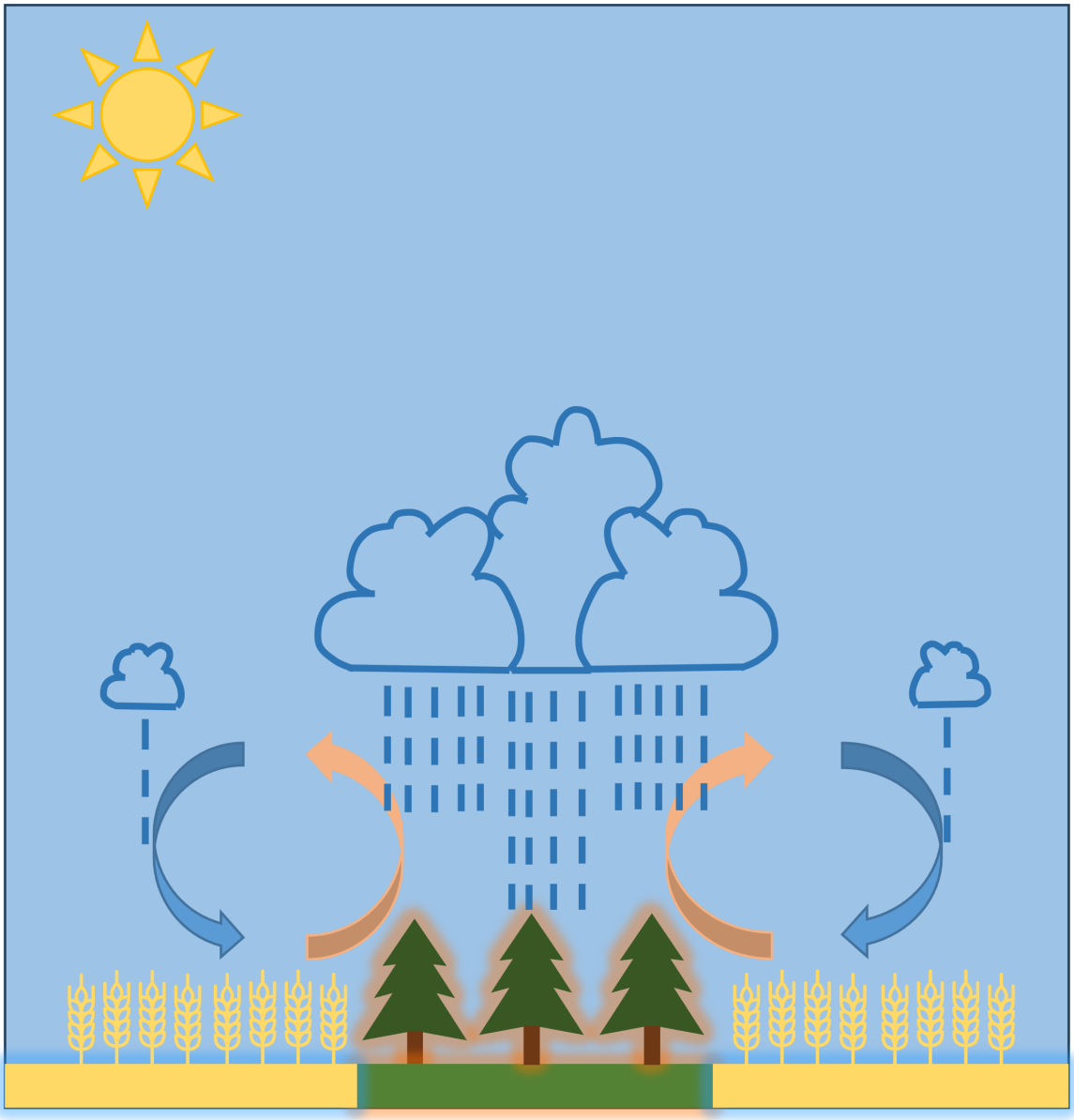

Figure 3.16: Cartoon schematic of the formation of the forest breeze at the boundary of pasture and coniferous forest. Orange highlights on the trees indicate greater temperatures, while blue highlights over the pasture indicate lower temperatures. Clouds and rainfall are shown in dark blue outlines, while the forest breeze circulations themselves are shown in orange and red arrows.

Brown and Arnold (1998); Esau and Lyons (2002); Rieck et al. (2014), there has not been a consistent name for these land surface-induced solenoidal circulations. Names which have been used in literature have included "vegetation breezes", "Non-Canonical Mesoscale Circulations (NCMCs)", "circulation[s] caused by contrasts in land use", and generic "mesoscale circulations," and "forest breezes." Given that the most dramatic land surface-induced mesoscale circulations in our simulations were those on the boundaries of the forested stripes, I will refer to these circulations as "forest breezes" within this discussion.

These findings, in corroboration with those from previous modeling and observational efforts, have implications for agricultural management. Along these sharp vegetation contrasts, the pattern of latent and sensible heating will determine which vegetation type receives more precipitation. As the studies cited above have shown, the area with greater sensible heat flux will be favored. On a forest-agricultural boundary, the vegetation type with the greater sensible heat flux will likely be quite variable, depending on soil moisture, time of year, and types of crops planted. If the agricultural area is hotter (with a greater sensible heat flux) than the forest, it will likely receive more rain at the expense of the forest, and vice-versa.

I should also add that these forest breezes and the storms they initiate are sensitive to the size of the vegetation stripes. Previous work has suggested an "ideal stripe size" which allows the two forest breezes to intersect in the middle of the hotter patch and lead to intense mechanical lifting there (Chen and Avissar, 1994; Hong et al., 1995; Lynn et al., 1998). This would have, in effect, accelerated the evolution of convection in our simulations by 3 hours by allowing the strong storms in the center of the forest which formed late in the simulation to initiate earlier. In our simulations, the rising branches of the two forest breeze circulations were approximately 15 km from the center of the circulation as seen in Figure 3.12, implying an ideal forest stripe size of approximately 30 km. However, even if this promoted the development of stronger storms earlier in the day (which seems likely given the intensity of the convection which developed as the inflow branches of the two forest breezes collided over the center of the forest at 1500 LT in the PF and SF simulations), this wouldn't necessarily increase total precipitation. The area of the forest, and

hence the area suitable for convection would be smaller. The storms initiating in the middle of the forest stripe would quickly precipitate and produce intense cold pools as occurs in the PF and SF simulations after 1600 LT (Supplemental Animation 2d,e). Once this happened, instability over the forest would decrease and storms would quickly weaken and die out. Over our 100 km-wide forest stripe, by contrast, storms can start on the edge and progress inward following cold pools. This allows convection to continue for many hours over the forest as storms continually have access to fresh CAPE. Whichever stripe size is "ideal" will depend on many factors, including atmospheric stability, humidity, and surface properties which will affect cold pool propagation speeds and dissipation rates. What constitutes an "ideal stripe size" will therefore change day-to-day. This has real-world implications for areas such as the Mississippi Delta, where forested stripes of various widths lie within agricultural areas.

The interactions of forest breezes, cold pools, and sea breezes, and their impacts on coastal convection are complex and not completely understood. Future study of these phenomena, and their interaction with other factors such as topography and urban effects, may improve forecasts of the location, timing, and hazards of convective storms in the coastal environment.

Chapter 4

Conclusion

For this thesis I conducted two studies which examined the role of land surface properties in affecting lake-effect snow and coastal deep convection, respectively. Our first study analyzed the 1-7 January 2010 lake-effect snow event over Lake Erie using two simulations, one CONTROL simulation with realistic land and lake cover and an NLH simulation in which I replaced Lake Huron with a forest. Our second study investigated the combined effects of the sea breeze, land surface-induced circulations, and cold pools on the development and impacts of coastal deep convection. I used six simulations in this second study, three of which (UP, UF, US) had a uniform land surface type and three of which (PF, SF, SP) had a striped pattern of land surface properties. In our first study, I found that the presence of Lake Huron increases snowfall over and downwind of Lake Erie. This occurs as lake-effect snow bands first develop over Lake Huron in the CONTROL simulation. These bands weaken, but their secondary circulations do not disappear, as they pass over the Ontario Peninsula separating Lake Huron from Lake Erie. As the circulations emerge over Lake Erie, they reintensify into deep and strong L2L snow bands which produce heavy snowfall totals over and downwind of the lake. When Lake Huron is absent in the NLH simulation, by contrast, there is no pre-existing L2L circulation to reintensify over Lake Erie. As a result, convective lake-effect snow bands over Lake Erie must develop "from scratch." This process of development takes time, however, and the narrow width of Lake Erie means that these lake-effect bands cannot grow as strong or produce as heavy snowfall totals as those which are connected to Lake Huron. Another factor inhibiting the growth of the lake-effect snow bands in the NLH simulation is the shallower PBL height over Lake Erie compared to the CONTROL simulation. Lake Huron, through surface sensible heat flux and the latent heat release of lake-effect convection, raises the height of the PBL. This allows subsequent lake-effect bands over Lake Erie in the CONTROL simulation to grow deeper than that in the NLH simulation in which the PBL, unmodified by Lake Huron, is shallower. I also found that areas of snow-free land surrounded by snow-covered land

can act as “brown lakes,” as the large sensible heat flux over the snow-free land destabilizes the overlying atmosphere much as the warm Great Lakes do. In the presence of northwesterly winds over the snow-free land, this destabilization promotes the growth of weak snow bands very similar to lake-effect bands. As with the lake-effect bands which form over Lake Huron and persist over land before reintensifying over Lake Erie, these “brown lake-effect” bands can persist over snow-covered land before reintensifying as they move over a lake. In both our CONTROL and NLH simulations, an area of snow-free land west of Lake Ontario initiated these “brown lake-effect” bands which subsequently reintensified over northeast Lake Erie, producing heavy snowfall totals on the downwind lake shore. In our second study, which focused on the interactions between the sea breeze, land-surface induced circulations and cold pools, I found that the coniferous forest land surface became hotter than the pasture or suburban land surfaces. In our three uniform land surface simulations, this led to a greater coverage of convection and precipitation over the uniform forest as opposed to over the uniform pasture or suburb. In our striped land surface experiments, PF and SF, the higher temperatures over the forest lowered surface pressures compared to the surrounding pasture or suburban land, leading to the formation of solenoidal mesoscale circulations with rising branches over the forest and sinking branches over the pasture and suburb. I refer to these land surface-induced circulations as "forest breezes." The lifting associated with rising branches of the forest breezes enhanced convection and precipitation over the forest while inhibiting it over the pasture and suburbs. I determined that within these idealized simulations that the forest breezes were more important than the sea breeze in determining the timing and location of convective storms. Unlike in the uniform land surface simulations, in which the first strong convective storms were concentrated along the sea breeze front, strong convection in the PF and SF simulations developed nearly simultaneously all along the edges of the forest. I also found that the cold pools produced by the storms forming along the forest edges reinforced the forest breeze circulations. This allowed the inflow branches of the forest breezes on each side of the forest to collide in the center of the forest stripe, which initiated strong convection and subsequently led to heavy precipitation. However, cold pools which resulted from the evaporation of this precipitation lowered the

average temperature over the forest compared to the surrounding pasture and suburbs, altogether destroying the forest breeze circulations in the late afternoon. Together, the results of these studies illustrate the complex effects and interactions between the land surface and convective storms. I also propose that the results of these studies may have direct implications for forecasters and agriculturalists. Forecasters may be able to predict the location of heavy lake-effect snow on the shores of a downwind lake by observing the motion of connected L2L bands over the upwind lake. Farmers whose fields are adjacent to different vegetation or land cover types may also be able to assess the likely impact of this gradient in land cover on rainfall over their fields, and plant certain crops accordingly. Finally, our findings in these two studies highlight opportunities for future research. For lake-effect snow events, I did not examine in detail how these L2L connections affect orographic-enhanced snowfall, both on the lake shore and inland of the lakes. Downwind of Lake Erie in Western New York, the Allegheny Plateau rises from 180 m to 510 m, while further south in Pennsylvania, Maryland, and West Virginia, the Allegheny Mountains rise to heights of over 1400 m. While the effects of orography on lake-effect snow have been studied previously, the role of L2L connections on this orographic precipitation has not (Campbell and Steenburgh, 2017; Niziol et al., 1995). Future modeling work analyzing the role of both air mass modification by upstream lakes and the presence of strong L2L circulations in this orographically-enhanced precipitation should be undertaken . For coastal convection enhanced by tree breezes, topographic effects are again an obvious next step in research. Previous work has demonstrated the relative strength of and interactions between diurnally-driven slope winds and tree breezes (Lee and Kimura, 2001; Kawase et al., 2008; Phillips et al., 2022). How topography, sea breezes, tree breezes, and cold pools interact has however received little attention. Future idealized modeling work would help illustrate how the combined effects of these processes influence the development of convection in mountainous coastal regions. Finally, while the model simulations performed for this research have highlighted potential processes around the manner in which sea breezes, tree breezes and cold pools interact to initiate and strengthen coastal convection, such hypotheses need to be assessed using real world data. For examining the role of tree breezes and sea breezes in a real-world

environment, the observations and case study simulations undertaken as part of the NSF-funded ESCAPE campaign provide a wealth of data in which the interaction of these two circulations, and their effects on convection, can be examined (Kollias et al., 2023). Future research focusing on analyzing these observational data may lead to additional insights into how tree breeze and sea breeze circulations, as well as cold pools, interact to affect convection in the real world.

References

Anthes, R. A., 1984: Enhancement of Convective Precipitation by Mesoscale Variations in Vegetative Covering in Semiarid Regions. *Journal of Applied Meteorology and Climatology*, **23 (4)**, 541–554, 10.1175/1520-0450(1984)023<0541:EOCPBM>2.0.CO;2.

Arakawa, AKIO., and V. R. Lamb, 1977: Computational Design of the Basic Dynamical Processes of the UCLA General Circulation Model. *Methods in Computational Physics: Advances in Research and Applications*, JULIUS. Chang, Ed., General Circulation Models of the Atmosphere, Vol. 17, Elsevier, 173–265, 10.1016/B978-0-12-460817-7.50009-4.

Avissar, R., and Y. Liu, 1996: Three-dimensional numerical study of shallow convective clouds and precipitation induced by land surface forcing. *Journal of Geophysical Research: Atmospheres*, **101 (D3)**, 7499–7518, 10.1029/95JD03031.

Bergmaier, P. T., and B. Geerts, 2020: LLAP Band Structure and Intense Lake-Effect Snowfall Downwind of Lake Ontario: Insights from the OWLeS 7-9 January 2014 Event. *J. Appl. Meteor. Climatol.*, **59**, 1691–1715, 10.1175/JAMC-D-19-0288.1.

Bergmaier, P. T., B. Geerts, L. S. Campbell, and W. J. Steenburgh, 2017: The OWLeS IOP2B Lake-Effect Snowstorm: Dynamics of the Secondary Circulation. *Mon. Wea. Rev.*, **145**, 2437–2459, 10.1175/MWR-D-16-0462.1.

Branch, O., and V. Wulfmeyer, 2019: Deliberate enhancement of rainfall using desert plantations. *Proceedings of the National Academy of Sciences*, **116 (38)**, 18 841–18 847, 10.1073/pnas.1904754116.

Brown, M. E., and D. L. Arnold, 1998: Land-surface–atmosphere interactions associated with deep convection in Illinois. *International Journal of Climatology*, **18 (15)**, 1637–1653, 10.1002/(SICI)1097-0088(199812)18:15<1637::AID-JOC336>3.0.CO;2-U.

Campbell, L. S., and W. J. Steenburgh, 2017: The OWLeS IOP2b Lake-Effect Snowstorm: Mechanisms Contributing to the Tug Hill Precipitation Maximum. *Monthly Weather Review*, **145 (7)**, 2461–2478, 10.1175/MWR-D-16-0461.1.

Chagnon, F. J. F., R. L. Bras, and J. Wang, 2004: Climatic shift in patterns of shallow clouds over the Amazon. *Geophysical Research Letters*, **31 (24)**, 10.1029/2004GL021188.

Chen, F., and R. Avissar, 1994: Impact of Land-Surface Moisture Variability on Local Shallow Convective Cumulus and Precipitation in Large-Scale Models. *Journal of Applied Meteorology and Climatology*, **33 (12)**, 1382–1401, 10.1175/1520-0450(1994)033<1382:IOLSMV>2.0.CO;2.

Chen, J., S. Hagos, H. Xiao, J. D. Fast, and Z. Feng, 2020: Characterization of Surface Heterogeneity-Induced Convection Using Cluster Analysis. *Journal of Geophysical Research: Atmospheres*, **125 (20)**, e2020JD032 550, 10.1029/2020JD032550.

Cioni, G., and C. Hohenegger, 2018: A simplified model of precipitation enhancement over a heterogeneous surface. *Hydrology and Earth System Sciences*, **22 (6)**, 3197–3212, 10.5194/hess-22-3197-2018.

Cooperative Institute for Research in the Atmosphere, 2022: A Stunning, Snow Scene in the Great Lakes. https://rammb.cira.colostate.edu/ramsdis/online/loop.asp?data_folder=loop_of_the_day/goes-16/20220126000000&number_of_images_to_display=100&loop_speed_ms=150.

Cotton, W. R., and Coauthors, 2003: RAMS 2001: Current Status and Future Directions. *Met. Atmos. Phys.*, **82**, 5–29, 10.1007/s00703-001-0584-9.

Dashtian, H., and M. H. Young, 2023: Soil Water Content and Meteorological Data to Support Tracking Aerosol Convection Interactions ExpeRiment (TRACER) over Harris County, Texas. Texas Data Repository, 10.18738/T8/FN3RWZ.

Derbyshire, S. H., I. Beau, P. Bechtold, J.-Y. Grandpeix, J.-M. Piriou, J.-L. Redelsperger, and P. M. M. Soares, 2004: Sensitivity of moist convection to environmental humidity. *Quarterly Journal of the Royal Meteorological Society*, **130 (604)**, 3055–3079, 10.1256/qj.03.130.

Drager, A. J., L. D. Grant, and S. C. van den Heever, 2022: A Nonmonotonic Precipitation Response to Changes in Soil Moisture in the Presence of Vegetation. *Journal of Hydrometeorology*, **23 (7)**, 1095–1111, 10.1175/JHM-D-21-0109.1.

Emori, S., 1998: The interaction of cumulus convection with soil moisture distribution: An idealized simulation. *Journal of Geophysical Research: Atmospheres*, **103 (D8)**, 8873–8884, 10.1029/98JD00426.

Esau, I. N., and T. J. Lyons, 2002: Effect of sharp vegetation boundary on the convective atmospheric boundary layer. *Agricultural and Forest Meteorology*, **114 (1)**, 3–13, 10.1016/S0168-1923(02)00154-5.

Fast, J. D., L. K. Berg, Z. Feng, F. Mei, R. Newsom, K. Sakaguchi, and H. Xiao, 2019: The Impact of Variable Land-Atmosphere Coupling on Convective Cloud Populations Observed During the 2016 HI-SCALE Field Campaign. *Journal of Advances in Modeling Earth Systems*, **11 (8)**, 2629–2654, 10.1029/2019MS001727.

Fisher, E. L., 1960: AN OBSERVATIONAL STUDY OF THE SEA BREEZE. *Journal of the Atmospheric Sciences*, **17 (6)**, 645–660, 10.1175/1520-0469(1960)017<0645:AOSOTS>2.0.CO;2.

Fujisaki-Manome, A., and Coauthors, 2020: Improvements in Lake-Effect Snow Forecasts Using a One-Way Air-Lake Model Coupling Approach. *J. Hydrometeor.*, **21**, 2813–2828, 10.1175/JHM-D-20-0079.s1.

Garcia-Carreras, L., D. J. Parker, and J. H. Marsham, 2011: What is the Mechanism for the Modification of Convective Cloud Distributions by Land Surface–Induced Flows? *Journal of the Atmospheric Sciences*, **68 (3)**, 619–634, 10.1175/2010JAS3604.1.

Giorgi, F., and R. Avissar, 1997: Representation of heterogeneity effects in Earth system modeling: Experience from land surface modeling. *Reviews of Geophysics*, **35 (4)**, 413–437, 10.1029/97RG01754.

Gowan, T. M., W. J. Steenburgh, and J. R. Minder, 2021: Downstream Evolution and Coastal-to-Inland Transition of Landfalling Lake-Effect Systems. *Mon. Wea. Rev.*, **149**, 1023–1040, 10.1175/MWR-D-20-0253.1.

Harrington, J. Y., 1997: The effects of radiative and microphysical processes on simulated warm and transition season arctic stratus. Ph.D. thesis, Colorado State University, Fort Collins, CO.

Harvey, N. J., C. L. Daleu, R. A. Stratton, R. S. Plant, S. J. Woolnough, and A. J. Stirling, 2022: The impact of surface heterogeneity on the diurnal cycle of deep convection. *Quarterly Journal of the Royal Meteorological Society*, **148 (749)**, 3509–3527, 10.1002/qj.4371.

Hersbach, H., and Coauthors, 2020: The ERA5 global reanalysis. *Q.J.R. Meteorol. Soc.*, **146 (730)**, 1999–2049, 10.1002/qj.3803.

Hill, G. E., 1974: Factors Controlling the Size and Spacing of Cumulus Clouds as Revealed by Numerical Experiments. *Journal of the Atmospheric Sciences*, **31 (3)**, 646–673, 10.1175/1520-0469(1974)031<0646:FCTSAS>2.0.CO;2.

Hjelmfelt, M. R., 1990: Numerical Study of the Influence of Environmental Conditions on Lake-Effect Snowstorms over Lake Michigan. *Mon. Wea. Rev.*, **118**, 138–150, 10.1175/1520-0493(1990)118%3C0138:NSOTIO%3E2.0.CO;2.

Hjelmfelt, M. R., W. Capehart, Y. Rodriguez, D. A. Kristovich, and R. Hoevet, 2004: Influence of Upwind Lakes on the Wintertime Lake-Effect Boundary Layer. *16th Symposium on Boundary Layers and Turbulence*, Portland, ME, 649–655.

Hong, X., M. J. Leach, and S. Raman, 1995: A Sensitivity Study of Convective Cloud Formation by Vegetation Forcing with Different Atmospheric Conditions. *Journal of Applied Meteorology*

and Climatology, **34 (9)**, 2008–2028, 10.1175/1520-0450(1995)034<2008:ASSOCC>2.0.CO;2.

Jensen, A. A., P. T. Bergmaier, B. Geerts, H. Morrison, and L. S. Campbell, 2020: Sensitivity of Convective Cell Dynamics and Microphysics to Model Resolution for the OWLeS IOP2b Lake-Effect Snowband. *Mon. Wea. Rev.*, **148**, 3305–3328, 10.1175/MWR-D-19-0320.1.

Jensen, M., and Coauthors, 2023: Tracking Aerosol Convection Interactions Experiment (TRACER) Field Campaign Report. Field Campaign Summary 23-038, Department of Energy, 1–132 pp.

Kang, S.-L., and G. H. Bryan, 2011: A Large-Eddy Simulation Study of Moist Convection Initiation over Heterogeneous Surface Fluxes. *Monthly Weather Review*, **139 (9)**, 2901–2917, 10.1175/MWR-D-10-05037.1.

Kawase, H., T. Yoshikane, M. Hara, F. Kimura, T. Sato, and S. Ohsawa, 2008: Impact of extensive irrigation on the formation of cumulus clouds. *Geophysical Research Letters*, **35 (1)**, 10.1029/2007GL032435.

Keeler, E., K. Burk, and J. Kyrouac, 2022: Balloon-borne sounding system (sondewnpn). 10.5439/1595321.

Kilgannon, C., L. Fadulu, H. Meko, and S. M. Nir, 2022: How the Buffalo Blizzard Became So Deadly. *The New York Times*.

Kilinc, M., and J. Beringer, 2007: The Spatial and Temporal Distribution of Lightning Strikes and Their Relationship with Vegetation Type, Elevation, and Fire Scars in the Northern Territory. *Journal of Climate*, **20 (7)**, 1161–1173, 10.1175/JCLI4039.1.

Klemp, J. B., and R. B. Wilhelmson, 1978: The Simulation of Three-Dimensional Convective Storm Dynamics. *Journal of the Atmospheric Sciences*, **35 (6)**, 1070–1096, 10.1175/1520-0469(1978)035<1070:TSOTDC>2.0.CO;2.

Kollias, P., and Coauthors, 2023: Experiment of Sea Breeze Convection, Aerosols, Precipitation, and Environment (ESCAPE). *Bull. Amer. Meteor. Soc.*

Kristovich, D. A., L. Bard, L. Stoecker, and B. Geerts, 2018: Influence of Lake Erie on a Lake Ontario Lake-Effect Snowstorm. *J. Appl. Meteor. Climatol.*, **57**, 2019–2033, 10.1175/JAMC-D -17-0349.1.

Kristovich, D. A., and N. F. Laird, 1998: Observations of Widespread Lake-Effect Cloudiness: Influences of Lake Surface Temperature and Upwind Conditions. *Wea. Forecasting*, **13**, 811–821, 10.1175/1520-0434(1998)013%3C0811:OOWLEC%3E2.0.CO;2.

Kristovich, D. A., and R. A. I. Steve, 1995: A Satellite Study of Cloud-Band Frequencies over the Great Lakes. *J. Appl. Meteor. Climatol.*, **34**, 2083–2089, 10.1175/1520-0450(1995)034% 3C2083:ASSOCB%3E2.0.CO;2.

Kunkel, K. E., N. E. Westcott, and D. A. R. Kristovich, 2002: Assessment of Potential Effects of Climate Change on Heavy Lake-Effect Snowstorms Near Lake Erie. *Journal of Great Lakes Research*, **28 (4)**, 521–536, 10.1016/S0380-1330(02)70603-5.

Laird, N. F., D. A. Kristovich, and J. E. Walsh, 2003: Idealized Model Simulations Examining the Mesoscale Structure of Winter Lake-Effect Circulations. *Mon. Wea. Rev.*, **131**, 206–221, 10.1175/1520-0493(2003)131%3C0206:IMSETM%3E2.0.CO;2.

Laird, N. F., N. D. Metz, L. Gaudet, C. Grasmick, L. Higgins, C. Loeser, and D. A. Zelinsky, 2017: Climatology of Cold Season Lake-Effect Cloud Bands for the North American Great Lakes. *Int. J. Climatol.*, **37**, 2111–2121, 10.1002/joc.4838.

Lang, C. E., J. M. McDonald, L. Gaudet, D. Doeblin, E. A. Jones, and N. F. Laird, 2018: The Influence of a Lake-to-Lake Connection from Lake Huron on the Lake-Effect Snowfall in the Vicinity of Lake Ontario. *J. Appl. Meteor. Climatol.*, **57**, 1423–1439, 10.1175/JAMC-D-17-0225 .1.

Lee, J. M., Y. Zhang, and S. A. Klein, 2019: The Effect of Land Surface Heterogeneity and Background Wind on Shallow Cumulus Clouds and the Transition to Deeper Convection. *Journal of the Atmospheric Sciences*, **76 (2)**, 401–419, 10.1175/JAS-D-18-0196.1.

Lee, S.-H., and F. Kimura, 2001: Comparative Studies In The Local Circulations Induced By Land-Use And By Topography. *Boundary-Layer Meteorology*, **101 (2)**, 157–182, 10.1023/A:1019219412907.

Lilly, D. K., 1962: On the numerical simulation of buoyant convection. *Tellus*, **14 (2)**, 148–172, 10.1111/j.2153-3490.1962.tb00128.x.

Lynn, B. H., W.-K. Tao, and P. J. Wetzel, 1998: A Study of Landscape-Generated Deep Moist Convection. *Monthly Weather Review*, **126 (4)**, 928–942, 10.1175/1520-0493(1998)126<0928:ASOLGD>2.0.CO;2.

Maeda, E. E., T. A. Abera, M. Siljander, L. E. O. C. Aragão, Y. M. de Moura, and J. Heiskanen, 2021: Large-scale commodity agriculture exacerbates the climatic impacts of Amazonian deforestation. *Proceedings of the National Academy of Sciences*, **118 (7)**, e2023787 118, 10.1073/pnas.2023787118.

Mann, G. E., R. B. Wagenmaker, and P. J. Sousounis, 2002: The Influence of Multiple Lake Interactions upon Lake-Effect Storms. *Mon. Wea. Rev.*, **130**, 1510–1530, 10.1175/1520-0493(2002)130%3C1510:TIOMLI%3E2.0.CO;2.

Marinescu, P. J., and Coauthors, 2021: Impacts of Varying Concentrations of Cloud Condensation Nuclei on Deep Convective Cloud Updrafts - A Multimodel Assessment. *J. Atmos. Sci.*, **78**, 1147–1172, 10.1175/JAS-D-20-0200.1.

Nair, U. S., R. O. Lawton, R. M. Welch, and R. A. Pielke Sr., 2003: Impact of land use on Costa Rican tropical montane cloud forests: Sensitivity of cumulus cloud field characteristics to lowland deforestation. *Journal of Geophysical Research: Atmospheres*, **108 (D7)**, 10.1029/2001JD001135.

National Operational Hydrologic Remote Sensing Center, 2004: Snow Data Assimilation System (SNODAS) Data Products at NSIDC. Data Subset: 24-Hour Snow Precipitation (Model Driving Data). NSIDC: National Snow and Ice Data Center, Boulder, Colorado USA, 10.7265/N5TB14TC.

Niziol, T. A., 1987: Operational Forecasting of Lake Effect Snowfall in Western and Central New York. *Wea. Forecasting*, **2**, 310–321, 10.1175/1520-0434(1987)002%3C0310:OFOLES%3E2.0.CO;2.

Niziol, T. A., W. R. Snyder, and J. S. Waldstreicher, 1995: Winter Weather Forecasting Throughout the Eastern United States. Part IV: Lake Effect Snow. *Wea. Forecasting*, **10**, 61–77, 10.1175/1520-0434(1995)010\%3C0061:WWFTTE\%3E2.0.CO;2.

NOAA, 2020: Great Lakes Surface Environmental Analysis (GLSEA). Great Lakes Environmental Research Laboratory.

Phillips, C. E., U. S. Nair, R. Mahmood, E. Rappin, and R. A. Pielke Sr, 2022: Influence of Irrigation on Diurnal Mesoscale Circulations: Results From GRAINEX. *Geophysical Research Letters*, **49 (7)**, e2021GL096 822, 10.1029/2021GL096822.

Rabin, R. M., S. Stadler, P. J. Wetzel, D. J. Stensrud, and M. Gregory, 1990: Observed Effects of Landscape Variability on Convective Clouds. *Bulletin of the American Meteorological Society*, **71 (3)**, 272–280, 10.1175/1520-0477(1990)071<0272:OEOLVO>2.0.CO;2.

Rapp, A. D., C. D. Kummerow, and L. Fowler, 2011: Interactions between warm rain clouds and atmospheric preconditioning for deep convection in the tropics. *Journal of Geophysical Research: Atmospheres*, **116 (D23)**, 10.1029/2011JD016143.

Reynolds, R. W., N. A. Rayner, T. M. Smith, D. C. Stokes, and W. Wang, 2002: An Improved In Situ and Satellite SST Analysis for Climate. *Journal of Climate*, **15 (13)**, 1609–1625, 10.1175/1520-0442(2002)015<1609:AIISAS>2.0.CO;2.

Rieck, M., C. Hohenegger, and P. Gentine, 2015: The effect of moist convection on thermally induced mesoscale circulations. *Quarterly Journal of the Royal Meteorological Society*, **141 (691)**, 2418–2428, 10.1002/qj.2532.

Rieck, M., C. Hohenegger, and C. C. van Heerwaarden, 2014: The Influence of Land Surface Heterogeneities on Cloud Size Development. *Monthly Weather Review*, **142 (10)**, 3830–3846, 10.1175/MWR-D-13-00354.1.

Rodriguez, Y., D. A. Kristovich, and M. R. Hjelmfelt, 2007: Lake-to-Lake Cloud Bands: Frequencies and Locations. *Mon. Wea. Rev.*, **135**, 4202–4213, 10.1175/2007MWR1960.1.

Rose, B. L., 2000: The Role of Upstream lakes in Determining Downstream Severe Lake-Effect Snowstorms. Ph.D. thesis, University of Illinois, Urbana-Champaign.

Saleeby, S. M., and W. R. Cotton, 2004: A Large-Droplet Mode and Prognostic Number Concentration of Cloud Droplets in the Colorado State University Regional Atmospheric Modeling System (RAMS). Part I: Module Descriptions and Supercell Test Simulations. *Journal of Applied Meteorology and Climatology*, **43 (1)**, 182–195, 10.1175/1520-0450(2004)043<0182:ALMAPN>2.0.CO;2.

Saleeby, S. M., and S. C. van den Heever, 2013: Developments in the CSU-RAMS Aerosol Model: Emissions, Nucleation, Regeneration, Deposition, and Radiation. *J. Appl. Meteor. Climatol.*, **52**, 2601–2622, 10.1175/JAMC-D-12-0312.1.

Sato, T., F. Kimura, and A. S. Hasegawa, 2007: Vegetation and topographic control of cloud activity over arid/semiarid Asia. *Journal of Geophysical Research: Atmospheres*, **112 (D24)**, 10.1029/2006JD008129.

Segal, M., R. W. Arritt, C. Clark, R. Rabin, and J. Brown, 1995: Scaling Evaluation of the Effect of Surface Characteristics on Potential for Deep Convection over Uniform Terrain. *Monthly Weather Review*, **123 (2)**, 383–400, 10.1175/1520-0493(1995)123<0383:SEOTEO>2.0.CO;2.

Smagorinsky, J., 1963: General Circulation Experiments with the Primitive Equations Part 1: The Basic Experiment. *Monthly Weather Review*, **91 (3)**, 99–164, 10.1175/1520-0493(1963)091<0099:GCEWTP>2.3.CO;2.

Sousounis, P. J., and G. E. Mann, 2000: Lake-Aggregate Mesoscale Disturbances. Part V: Impacts on Lake-Effect Precipitation. *Mon. Wea. Rev.*, **128**, 728–745, 10.1175/1520-0493(2000)128%3C0728:LAMDPV%3E2.0.CO;2.

Steenburgh, W. J., and L. S. Campbell, 2017: The OWLES IOP2b Lake-Effect Snowstorm: Shoreline Geometry and the Mesoscale Forcing of Precipitation. *Mon. Wea. Rev.*, **145**, 2421–2436, 10.1175/MWR-D-16-0460.1.

Sykes, R. I., W. S. Lewellen, and D. S. Henn, 1988: A Numerical Study of the Development of Claud-Street Spacing. *Journal of the Atmospheric Sciences*, **45 (18)**, 2556–2570, 10.1175/1520-0469(1988)045<2556:ANSOTD>2.0.CO;2.

Taylor, C. M., R. A. M. de Jeu, F. Guichard, P. P. Harris, and W. A. Dorigo, 2012: Afternoon rain more likely over drier soils. *Nature*, **489 (7416)**, 423–426, 10.1038/nature11377.

Villani, J. P., M. J. J. Sr., and K. Reinhold, 2017: Forecasting the Inland Extent of Lake-Effect Snow Bands Downwind of Lake Ontario. *J. Operational Meteor.*, **5 (5)**, 53–70, 10.15191/nwajom.2017.0505.

Walko, R. L., and Coauthors, 2000: Coupled Atmosphere-Biophysics-Hydrology Models for Environmental Modeling. *J. Appl. Meteor. Climatol.*, **39**, 931–944, 10.1175/1520-0450(2000)039\%3C0931:CABHMF\%3E2.0.CO;2.

Wang, C., W. Tian, D. J. Parker, J. H. Marsham, and Z. Guo, 2011: Properties of a simulated convective boundary layer over inhomogeneous vegetation. *Quarterly Journal of the Royal Meteorological Society*, **137 (654)**, 99–117, 10.1002/qj.724.

Weckwerth, T. M., J. W. Wilson, and R. M. Wakimoto, 1996: Thermodynamic Variability within the Convective Boundary Layer Due to Horizontal Convective Rolls. *Monthly Weather Review*, **124 (5)**, 769–784, 10.1175/1520-0493(1996)124<0769:TVWTCB>2.0.CO;2.

Weisman, M. L., and J. B. Klemp, 1984: The Structure and Classification of Numerically Simulated Convective Stormsin Directionally Varying Wind Shears. *Monthly Weather Review*, **112 (12)**, 2479–2498, 10.1175/1520-0493(1984)112<2479:TSACON>2.0.CO;2.

Wright, D. M., D. J. Posselt, and A. L. Steiner, 2013: Sensitivity of Lake-Effect Snowfall to Lake Ice Cover and Temperature in the Great Lakes Region. *Mon. Wea. Rev.*, **141**, 670–689, 10.1175/MWR-D-12-00038.1.

Yan, H., and R. A. Anthes, 1987: The Effect of Latitude on the Sea Breeze. *Monthly Weather Review*, **115 (5)**, 936–956, 10.1175/1520-0493(1987)115<0936:TEOLOT>2.0.CO;2.

Yang, Q., and B. Geerts, 2006: Horizontal Convective Rolls in Cold Air over Water: Buoyancy Characteristics of Coherent Plumes Detected by an Airborne Radar. *Mon. Wea. Rev.*, **134**, 2373–2396, 10.1175/MWR3203.1.